CWP-673
April 2010

Gaussian beam modeling in heterogeneous anisotropic media

Yongxia Liu

— Master of Science Thesis —
Geophysics

Defended April 30, 2010

Committee Chair & Advisor:
Dr. Ilya Tsvankin

Committee members:
Dr. Paul Sava
Dr. Charles P. Oden

Center for Wave Phenomena
Colorado School of Mines
Golden, Colorado 80401
(1) 303 384-2178

Abstract

Anisotropy-induced shear-wave cusps (triplications) have been recorded in laboratory rock-physics experiments, long-offset VSP data, and cross-well surveys. Ray tracing is insufficient for simulating shear-wave cusps because the ray amplitudes at the edge of the cusp become infinite. The Gaussian-beam (GB) method has been shown to improve the performance of modeling and imaging algorithms based on ray theory. In particular, complex-valued amplitudes of Gaussian beams help properly describe the wavefield in the neighborhood of caustics. In this thesis, I apply the GB summation method to model SV-wave cusps in transversely isotropic (TI) media. The weighting factor and beam parameters are investigated with the goal of maintaining both accuracy and efficiency of modeling. I identify the optimal range for the initial beam width as well as the beam interval and angle coverage. For example, the initial beam width strongly influences the amplitudes and the polarization for cuspoidal wavefronts. With an appropriate choice of the beam parameters, the GB method produces an adequate approximation for cuspoidal wavefronts in homogeneous and layered TI media. In particular, the amplitudes from GB summation are close to exact values obtained by the finite-difference (FD) method. The GB method also partially reproduces nonlinear polarization along the cusp and the diffraction tail away from the edges of the cusp.

Table of Contents

Acknowledgments

I am deeply grateful to my committee members: Ilya Tsvankin, Paul Sava, and Charles P. Oden. Discussions with them have opened my eyes to novel ideas and different perspectives on the same problem. My thesis adviser, Ilya Tsvankin, has given me adequate freedom to work on my ideas. Dr. Tsvankin's sharp scientific insights and his ability to clearly and elegantly explain complex ideas always amaze me. Discussions with Paul Sava and Chuck Oden always provided me with new ideas about the project.

A special thanks goes to Ivan Pšenčík, who is most responsible for helping me with the ray theory. I really appreciate his patience and encouragement.

The summer internship with N. Ross Hill encouraged me in the Gaussian-beam field. The project led me into a new area in beam migration application. His creative ideas gave me fresh insights all the time.

I appreciate Norm Bleistein for his help and advice on Gaussian beams and technical writing. He is a professional writer who clearly explains complex mathematical definitions.

Roel Snieder is always open to new ideas and is a constant source of encouragement.

Dave Hale allowed me to sit in on his C-team seminar. His enthusiasm and his ability to simplify ideas make learning fun and interesting. His swimming lessons and classes taught me how to learn independently.

The math clinic from John Stockwell aided me a lot during this project. John is open to any question in math or Seismic Unix. During the review of my thesis, John helped me check the mathematical derivations.

Barbara McLenon acts as a "mom" to many of us. She devoted her time to our thesis formatting and editing. Michelle Szobody and Pam Beckman are always there to solve student problems saving us tons of time. Diane Witters significantly helped me to improve my English skills.

The Geophysics Department, with Terry Young at the head, has created a wonderful environment that fosters learning and collaboration that has helped me expand my horizons. I am grateful to Chevron Energy Technology Company for the internship opportunities.

Many friends have helped and encouraged me along the way. I have appreciated the friendship with all colleagues and friends Jia Yan, Joyti Behara, Xiaoxiang Wang, Yong Ma, Tongning Yang, Mamoru Takanashi, Yuanzhong Fan, Ran Xuan, Farnoush Forghani, Francesco Perepone, Bharath Shekar, Jeff Godwin, Filippo Broggini, Steve Smith, Myong Jae Kwon, Chris Engelsma, Clement Fleury and Xia Qin. I will always be grateful for their friendship.

My family has given me the love and support that has carried me through rough times. They have been a constant source of encouragement.

Chapter 1

Introduction

The GB summation method is a powerful extension of the ray method (Červený & Pšenčík, 2009), which represents a high-frequency approximation of the elastodynamic wave equation. Gaussian beams employ complex amplitudes and traveltimes to remove singularities in the wavefield. The complex traveltime can be modeled by the complex eikonal function (Kravstov & Berczynski, 2007). However, it is difficult in practice to apply complex parameters including the slowness and coordinate components in seismic data processing. To solve this problem, complex beams are approximated by the paraxial Gaussian beam, which consists of the central ray built by ray tracing and a quadratic expansion in the vicinity of the central ray.

The theory of Gaussian beams has been developed in many fields including optics (Siegman, 1986), electromagnetics (Nowack & Orefice, 1993), and geophysics (Červený *et al.*, 1982; Hill, 1990, 2001). In geophysics, Gaussian beams from the scalar wave equation have been introduced by Babich & Popov (1990), Popov (1982), and Červený *et al.* (1982). The concept of Gaussian beams has been extended to elastic media by Červený & Pšenčík (1983a, 1983b), Červený*et al.* (1984), Červený (1985), Hanyga (1986), George *et al.* (1987), Popov (2002), and Červený & Pšenčík (2009). Also the GB summation method has been effectively applied in seismic migration (Hill, 1990, 2001). Further development of beam migration included true-amplitude migration of field data (Gray, 2005; Gray & Bleistein, 2009). P-wave GB migration in anisotropic media was discussed by Alkhalifah (1995) and Zhu *et al.* (2007). Here, we focus on the GB method for SV-waves in anisotropic media.

The GB summation method has several advantages to simulate seismic wave propagation. In contrast to the ray-tracing method, GB summation can handle triplications, which are common in heterogeneous media. The GB method maintains the efficiency of ray tracing while avoiding the cumbersome implementation of two-point

ray tracing. In addition, it helps model shadow-zone information using diffracted waves. All these properties make Gaussian beams appealing for seismic exploration.

In TI media, the SV-wave wavefront becomes cuspoidal if the strength of anisotropy exceeds a certain critical value. These anisotropy-induced shear-wave cusps (triplications) have been recorded in laboratory rock-physics experiments and long-offset VSP data. With the growing interest in shear and converted waves, it becomes necessary to model cuspoidal wavefronts. However, ray tracing is insufficient for simulating shear-wave cusps because the ray amplitudes at the edge of the cusp become infinite. Here, the GB summation method is applied to compute the cuspoidal wavefronts in TI media.

The procedure for GB modeling in anisotropic media is similar to that for the isotropic case (Červený, 1985). First, we apply the ray tracing method to calculate the central rays from sources to receivers and obtain their parameters including the traveltime, geometrical spreading, and reflection/transmission coefficients. Secondly, these ray parameters are used to form single beams. Then, these single beams are summed together to generate the whole wavefield. Finally, the source wavelet is applied to the beam summation results to obtain seismograms.

As discussed above, to trace the central ray and to record the dynamic ray parameters for beams, I apply ray tracing in 2D TI media. In Chapter 2, the basic features of the ray method for heterogeneous anisotropic media are reviewed following Červený & Moser (2007). Both kinematic and dynamic ray tracing are described.

In Chapter 3, I review the GB method in isotropic media and extend it to anisotropic media. To maintain the efficiency and accuracy of modeling, the weighting factor and the beam parameters have to be optimized. I choose homogeneous isotropic and anisotropic models to find appropriate beam parameters for P- and SV-waves. The results confirm that GB summation produces a good approximation for the exact amplitudes in both isotropic and anisotropic media.

Then the GB method is applied to SV-wave cusps in TI media (Chapter 4). First, I discuss the conditions necessary to generate SV-wave cusps. Then homogeneous TI models are used to test the accuracy of amplitudes and polarization produced by Gaussian beams. The amplitudes along the cuspoidal wavefronts are compared with the results from FD modeling. In addition, the polarization along different branches of the cusp is investigated.

In Chapter 5, I apply the GB method to heterogeneous media. A four-layer VTI model is used to generate reflected shear waves. The shear-wave cusps from GB summation for this more complicated model closely match the FD results.

Chapter 6 contains the conclusions and recommendations for future work.

Chapter 2

Ray Theory in Heterogeneous Anisotropic Media

2.1 Summary

The GB method is an extension of ray tracing, which is used to compute the central ray for each beam. Therefore, it is necessary to review the basic ray theory for heterogeneous anisotropic structures.

Seismic ray theory is an asymptotic high-frequency approximation for seismic waves propagating in heterogeneous isotropic or anisotropic media. For finite frequencies, the ray method is not exact, but it provides a good approximation in the far field at large distances from the source. Ray tracing in anisotropic media is extensively discussed in the literature. Here, we mainly follow the work of Červený (1972), Hanyga (1986), Alkhalifah (1995), and Červený & Moser (2007).

The ray method includes kinematic and dynamic ray tracing. Kinematic ray tracing produces the traveltime, raypath, and wavefront of a specific arrival. Dynamic ray tracing computes the geometrical spreading and displacement vector needed to generate synthetic seismograms. Kinematic ray tracing can be implemented using Snell's law and the Fermat principle. Dynamic ray tracing is based on the paraxial ray approximation.

2.2 Basics of Ray Theory

For an anisotropic medium, the source-free elastodynamic equation has the form

$$\left(c_{ijkl}u_{k,l}\right)_{,j} = \rho\frac{\partial^2 u_i}{\partial t^2}, \tag{2.1}$$

where u_i are the components of the displacement vector expressed through the Cartesian coordinates x_i and traveltime t, c_{ijkl} are the components of the stiffness tensor, ρ is the density, and $u_{k,l}$ denotes the derivative of u_k with respect to x_l. Considering the leading order approximation of the ray method, a trial solution for equation 2.1 can be expressed as

$$\boldsymbol{u}(x_i, t) = \boldsymbol{U}(x_i) \exp\left[-i\omega(t - \tau(x_i))\right], \tag{2.2}$$

where $\tau(x_i)$ is the traveltime, $\boldsymbol{U}(x_i)$ is the ray-theory amplitude vector which is real for the ray theory and complex for Gaussian beams; ω is the circular frequency and t is the time. Substituting equation 2.2 into equation 2.1, we obtain

$$-N_i(\boldsymbol{U}) + i\omega^{-1} M_i(\boldsymbol{U}) + \omega^{-2} L_i(\boldsymbol{U}) = 0, \tag{2.3}$$

where

$$\begin{aligned} N_i(\boldsymbol{U}) &= c_{ijkl} p_j p_l U_k - \rho U_i, \\ M_i(\boldsymbol{U}) &= c_{ijkl} p_j U_{k,l} + (c_{ijkl} p_l U_k)_{,j}, \\ L_i(\boldsymbol{U}) &= (c_{ijkl} U_{k,l})_{,j}. \end{aligned} \tag{2.4}$$

Here p_i are the components of the slowness vector $\boldsymbol{p}$, given by

$$p_i = \frac{\partial \tau}{\partial x_i} = \frac{n_i}{V}; \tag{2.5}$$

where n_i denote the components of the unit vector $\boldsymbol{n}$, which is perpendicular to the wavefront, and V is the phase velocity (V_P for P-waves and V_S for S-waves). Equation 2.4 is valid for heterogeneous anisotropic media.

As the traveltime τ and amplitudes $\boldsymbol{U}$ are assumed to be frequency-independent, N_i, M_i and L_i are also frequency-independent. Since equation 2.3 should be valid for

any frequency, N_i, M_i, and L_i should go to zero:

$$c_{ijkl}p_j p_l U_k - \rho U_i = 0, \tag{2.6}$$

$$c_{ijkl}p_j U_{k,l} + (c_{ijkl}p_l U_k)_{,j} = 0, \tag{2.7}$$

$$(c_{ijkl}U_{k,l})_{,j} = 0. \tag{2.8}$$

Equations 2.6 and 2.7 are sufficient to calculate the leading terms including the traveltime $\tau(x_i)$ and the amplitude vector $\boldsymbol{U}(x_i)$. Equation 2.8 is ignored because it is not satisfied for the leading term (Červený*et al.*, 2007). Equation 2.6 leads to the so-called Christoffel equation responsible for plane-wave propagation

$$(\Gamma_{ik} - \delta_{ik})U_k = 0, \quad i = 1, 3. \tag{2.9}$$

$\Gamma_{ik} = a_{ijkl}p_j p_l$ is called the generalized Christoffel matrix, a_{ijkl} are the density-normalized stiffness coefficients. The matrix Γ_{ik} has three eigenvalues $G^{(m)}(x_i, p_n)$ and three corresponding eigenvectors $\boldsymbol{g}^{(m)}(x_i, p_n)$, which correspond to three types wave propagating in heterogeneous anisotropic media with P, S_1, and S_2 waves. For each mode, the eigenvalue $G^{(m)}$ should satisfy the equation

$$G^{(m)}(x_i, p_j) = 1. \tag{2.10}$$

In the symmetry plane, the SH-wave is decoupled from P- and SV-waves. Here, we only discuss P- and SV-waves. For P-waves, $G_1(x_i, p_j) = V_P^2 p_i p_i$. For SV-waves, $G_2(x_i, p_j) = V_{SV}^2 p_j p_j$. Here V_P and V_{SV} are the phase velocity corresponding to the slowness vector $\boldsymbol{p}$.

The vectorial ray amplitude $\boldsymbol{U}$ is expressed in terms of the unit real-valued eigenvector $\boldsymbol{g}^{(m)}$ of the Christoffel matrix

$$\boldsymbol{U} = A\boldsymbol{g}^{(m)}. \tag{2.11}$$

Here $A = A(x_i)$ is a frequency-independent scalar amplitude. Equation 2.10 is a nonlinear partial differential equation of the first-order derivative for the traveltime $\tau(x_i)$, which is called the eikonal equation for heterogeneous anisotropic media. The eikonal equation is used for kinematic ray tracing in the next section.

Multiplying equation 2.7 by the eigenvector $g_i^{(m)}$, we obtain the partial differential equation of the first-order derivative for the scalar amplitude $A(x_i)$:

$$2\boldsymbol{V_G} \cdot \nabla(\sqrt{\rho}A) + (\sqrt{\rho}A)\nabla \cdot \boldsymbol{V_G} = 0, \tag{2.12}$$

where

$$V_{Gi} = a_{ijkl} p_l g_k^{(m)} g_j^{(m)}. \tag{2.13}$$

Equation 2.12 is a form of the transport equation, and $\boldsymbol{V_G}$ is the group velocity vector.

2.3 Ray Tracing in 2D Heterogeneous Anisotropic Media

2.3.1 Ray Tracing

The eikonal equation 2.10 is a nonlinear partial differential equation of the first-order derivative for the traveltime $\tau(x_i)$. It can be expressed in the Hamiltonian form,

$$H(x_i, p_j) = \frac{1}{2}\left[G^{(m)}(x_i, p_j) - 1\right] = 0, \tag{2.14}$$

where H is the Hamiltonian function. Because equation 2.14 is nonlinear for the first-order and second-order derivatives, this system can be solved by the method of characteristics. The parameter specifying the points along the characteristics depends on the selected Hamiltonian. In this paper, we choose this parameter the traveltime τ. The formulas for ray tracing in heterogeneous anisotropic media can be expressed in terms of Hamiltonian equations as

$$\frac{\mathrm{d}x_i}{\mathrm{d}\tau} = \frac{1}{2}\frac{\partial G^{(m)}}{\partial p_i}, \qquad \frac{\mathrm{d}p_i}{\mathrm{d}\tau} = -\frac{1}{2}\frac{\partial G^{(m)}}{\partial x_i}, \tag{2.15}$$

where

$$G^{(m)}(x_n, p_n) = \Gamma_{ik}(x_n, p_n) g_i^{(m)} g_k^{(m)} = 1, \tag{2.16}$$

and

$$\Gamma_{ik}(x_n, p_n) = a_{ijkl}(x_n)p_j p_l. \tag{2.17}$$

Here, $G^{(m)}$ and $\boldsymbol{g}^{(m)}$ are the eigenvalue and eigenvector of the Christoffel matrix Γ_{ik}, respectively, x_i denote the coordinates along the trajectory, p_i are the components of the slowness vectors $p_i = \dfrac{n_i}{V}$, n_i is a unit vector in the direction of the wave normal (parallel to the slowness vector $\boldsymbol{p}$), and V is the phase velocity.

Therefore, the ray tracing system for heterogeneous anisotropic media is given by

$$\frac{\mathrm{d}x_i}{\mathrm{d}\tau} = a_{ijkl}p_l g_j^{(m)} g_k^{(m)}, \qquad \frac{\mathrm{d}p_i}{\mathrm{d}\tau} = -\frac{1}{2}\frac{\partial a_{ijkl}}{\partial x_i}p_n p_l g_j^{(m)} g_k^{(m)}. \tag{2.18}$$

For isotropic media, the ray tracing system reads

$$\frac{\mathrm{d}x_i}{\mathrm{d}\tau} = V^2 p_i, \qquad \frac{\mathrm{d}p_i}{\mathrm{d}\tau} = -\frac{\partial \ln V}{\partial x_i}; \tag{2.19}$$

V denotes the P- or SV-wave velocity.

The initial conditions ($\tau = 0$) for the ray tracing system are

$$x_i(0) = x_i^0, \qquad p_i(0) = p_i^0, \tag{2.20}$$

where x_i^0 denote the source coordinates and $p_i^0 = n_i^0/V$ are the slowness components at the source which define the initial ray directions.

During ray-tracing calculations, one of the criteria to test the accuracy of the algorithm is to verify that

$$p_i V_{Gi} = 1. \tag{2.21}$$

2.3.2 Dynamic Ray Tracing

The ray-tracing system allows us to compute the ray trajectory along with the traveltime τ and slowness vector $\boldsymbol{p}$. However, these quantities are not known in the vicinity of the ray. In addition, geometrical spreading and ray amplitudes cannot be computed by kinematic ray tracing alone. Geometrical spreading is computed by

dynamic ray tracing (DRT) or paraxial dynamic ray tracing. DRT involves solving a system of linear ordinary differential equations along a central ray. It yields the derivatives of the coordinates along the ray and of the corresponding slowness vectors with respect to the ray parameters.

The DRT system can be expressed in many forms and in various coordinate systems. The most common choices are the general Cartesian coordinate system (x_i) and the wavefront orthonormal coordinate system (y_i). GB summation requires the geometrical spreading in wavefront orthonormal coordinate. In the following, all the parameters in the dynamic ray tracing system are in wavefront orthonormal coordinates.

The dynamic ray-tracing equations given by Hanyga (1986) and Alkhalifah (1995) for 2D anisotropic media are

$$\begin{aligned} \frac{\mathrm{d}Q}{\mathrm{d}\tau} &= SP + NQ, \\ \frac{\mathrm{d}P}{\mathrm{d}\tau} &= -NP - FQ, \end{aligned} \tag{2.22}$$

where P and Q are defined as $Q = \dfrac{\partial y_1}{\partial t}$ and $P = \dfrac{\partial(\partial\tau/\partial y_1)}{\partial\tau}$, S, N, F are the derivatives of the eikonal with respect to y_1 (normal to the phase direction) and to p_1 (the ray parameter in the direction of y_1). They can be expressed as

$$\begin{aligned} S &= 0.5\frac{\partial^2 G^{(m)}}{\partial y_1^2} - 0.25\left(\frac{\partial G^{(m)}}{\partial y_1}\right)^2, \\ F &= 0.5\frac{\partial^2 G^{(m)}}{\partial (p_1)^2} - 0.25\left(\frac{\partial G^{(m)}}{\partial p_1}\right)^2, \\ N &= 0.5\frac{\partial^2 G^{(m)}}{\partial p_1 \partial y_1} - 0.25\left(\frac{\partial G^{(m)}}{\partial p_1}\frac{\partial G^{(m)}}{\partial y_1}\right). \end{aligned} \tag{2.23}$$

For isotropic media, the DRT equations are simplified to

$$\frac{\mathrm{d}Q}{\mathrm{d}\tau} = V^2 P, \tag{2.24}$$

$$\frac{\mathrm{d}P}{\mathrm{d}\tau} = -\frac{V_{,y_1 y_1}}{V} Q. \tag{2.25}$$

where V is the velocity, $V_{,y_1 y_1}$ is the second partial derivative of the phase velocity

in the y_1 direction. Equation 2.22 can be solved with a matrix formula that uses the fundamental matrix of linearly independent solutions of the DRT system. We call this fundamental matrix the DRT propagator matrix. The components of the propagator matrix are the DRT coefficients

$$\begin{pmatrix} Q_1 & Q_2 \\ P_1 & P_2 \end{pmatrix}.$$

The initial conditions for the fundamental solution of system 2.22 are formed by an identity matrix (Červený, 2001). Once the fundamental solution is found, the dynamic ray-tracing results can be obtained from the following equation:

$$\begin{pmatrix} Q \\ P \end{pmatrix} = \begin{pmatrix} Q_1 & Q_2 \\ P_1 & P_2 \end{pmatrix} \begin{pmatrix} Q_0 \\ P_0 \end{pmatrix}. \tag{2.26}$$

For ray tracing, the initial value of Q_0 and P_0 are real. For GB modeling, these values become complex, in the following, we denote them by Q_{GB0} and P_{GB0}. Similarly, Q_{GB} and P_{GB} denote the complex geometrical-spreading factors for Gaussian beams. Therefore, complex dynamic ray tracing for Gaussian beams can be represented by the following equation

$$\begin{pmatrix} Q_{GB} \\ P_{GB} \end{pmatrix} = \begin{pmatrix} Q_1 & Q_2 \\ P_1 & P_2 \end{pmatrix} \begin{pmatrix} Q_{GB0} \\ P_{GB0} \end{pmatrix}. \tag{2.27}$$

In heterogeneous media, the DRT should follow the interface condition in Appendix A.

Chapter 3

GB summation method

3.1 Summary

The ray tracing method is a useful approximation for body-wave propagation in heterogeneous isotropic or anisotropic media, even though it breaks down in caustic regions, in particular at the edges of triplications (Červený, 1972, 1983; Popov, 2002). In order to overcome these limitations while retaining the advantages of efficiency and simplicity, the GB summation method is applied (Červený *et al.*, 1982; Popov, 1982).

The theory of Gaussian beams in heterogeneous isotropic media has been described in many papers. Popov (1982), Babich & Popov (1990) and Červený *et al.* (1982) studied Gaussian beams for the scalar wave equation. Červený & Pšenčík (1983a, 1983b), George *et al.* (1987) and Popov (2002) extended Gaussian beams to elastic isotropic media. The GB method was successfully applied to seismic migration by Hill (1990, 2001), Gray (2005), and Gray & Bleistein (2009). Alkhalifah (1995) and Zhu *et al.* (2007) generalized the GB method to migration in transversely isotropic media. Červený & Pšenčík (2009) investigated single beams for the GB method in anisotropic media.

Gaussian beams in anisotropic media are different in several ways from their isotropic counterparts because velocity changes with angle. First, beam wavefronts are no longer perpendicular to the central ray because beams are formed in the vicinity of the central ray controlled by the group-velocity vector, while the wavefronts are perpendicular to the phase-velocity direction (Figure 3.1). In anisotropic media, group-velocity vectors generally deviate from the corresponding phase-velocity vectors in off-axis directions. Second, beams no longer spread equally when computed with a constant increment in the phase angle. In energy-focusing areas, the beam density is high, while in defocusing areas it is low (Pšenčík& Teles, 1996). Therefore, the beam

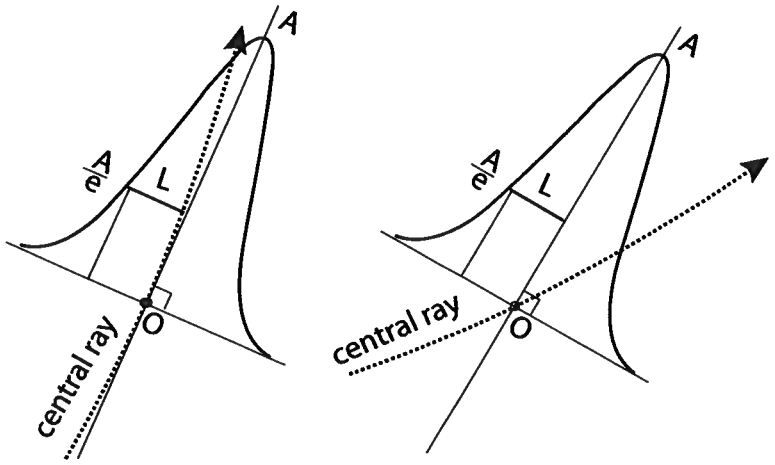

Figure 3.1: Gaussian beam wavefronts in isotropic (a) and anisotropic (b) media. In isotropic media, the beam wavefront is perpendicular to the central ray. In anisotropic media, the wavefront is perpendicular to the wave vector, which deviates from the central ray. L is the half-beam width corresponding to the amplitude A/e, where A is the peak amplitude.

parameters should be designed to obtain a good approximation for both focusing and defocusing areas. Third, the beam width changes with direction even in homogeneous anisotropic media because it is influenced by the angle variations of velocity and geometrical spreading.

The seismic wavefield is evaluated by integrating over all beams in the vicinity of a given receiver. This procedure has several advantages. First, time-consuming two-point ray tracing can be avoided. Second, the GB method yields stable results for a wide range of beam parameters. Third, Gaussian beams keep the amplitudes at caustics finite while ray tracing produces infinite amplitudes. In addition, the GB method maintains the efficiency of the ray tracing method; Gaussian beam modeling is two orders of magnitude faster than the finite-difference method.

Here, we discuss the single Gaussian beam and beam summation. To ensure accuracy of beam summation, the weighting factor and the beam parameters including the beam angle range, interval, and width should be carefully chosen.

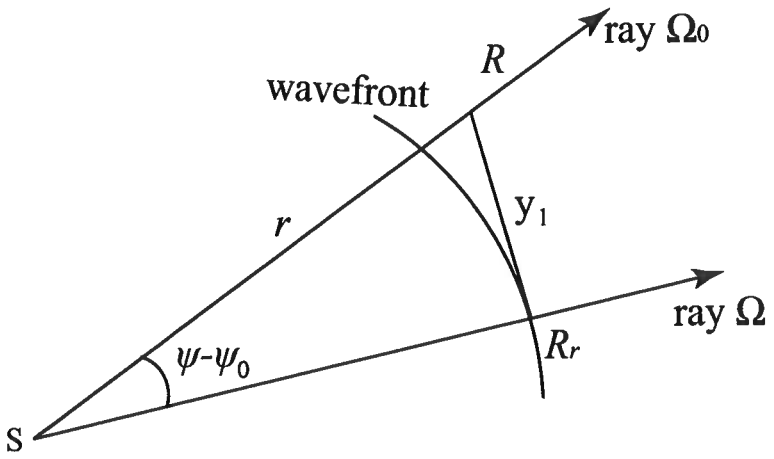

Figure 3.2: Geometry of a Gaussian beam. ψ is the group angle for the central ray Ω, ψ_0 is the group angle for ray Ω_0. R_r is the reference point on the central ray and R is the receiver. For ψ and ψ_0, the corresponding phase angles are θ and θ_0.

3.2 Gaussian Beams

A Gaussian beam is a high-frequency asymptotic time-harmonic solution of the wave equation, with a Gaussian amplitude profile around the central ray. It represents a bundle of complex-valued rays concentrated in the vicinity of the real-valued central ray. The complex traveltime at each point in the beam satisfies the complex eikonal equation 3.2 (Nowack & Orefice, 1993, 1994). A Gaussian beam is described by

$$\boldsymbol{u}_{GB}(R,\theta) = \boldsymbol{U}_{GB}(R_r,\theta)\exp\left[i\omega\tau(R,R_r)\right], \tag{3.1}$$

where $\boldsymbol{u}_{GB}(R,\theta)$ denotes the displacement for the beam with the phase angle θ, $\boldsymbol{U}_{GB}(R_r,\theta)$ is the complex-valued amplitude, $\tau(R,R_r)$ is the complex-valued traveltime, and R and R_r are the receiver point and reference point on the central ray, respectively (Figure 3.2). Both $\boldsymbol{U}_{GB}$ and τ are smooth functions of the spatial coordinates.

The traveltime $\tau(R,R_r)$ can be obtained from the complex eikonal equation,

$$(\nabla\tau)^2 = \left(\frac{1}{V}\right)^2, \tag{3.2}$$

$$\tau = \tau_R + i\tau_I. \tag{3.3}$$

Applying both the real and imaginary parts of the complex eikonal equation 3.3 to the ray-tracing system, we obtain the complex GB system (Nowack & Orefice, 1993, 1994).

3.2.1 Paraxial Gaussian Beams

The complex parameters of Gaussian beams including the slowness vector and coordinates are difficult to apply in practice, especially for heterogeneous media (Nowack & Orefice, 1993, 1994). Therefore, a common approximation is to expand the complex traveltime into a second-order Taylor series (Červený, 1985). We refer to this second-order Taylor expansion as the "paraxial Gaussian beam". The complex traveltime in paraxial Gaussian beams can be found as

$$\tau(R, R_r) = \tau(S, R_r) + i\frac{y_1^2}{2}M_{GB}. \tag{3.4}$$

where $\tau(S, R_r)$ is the real traveltime from the source to the reference point on the central ray, and $M_{GB} = \dfrac{\partial^2\tau}{\partial y_1^2}$ is the second-order derivative of the traveltime, which is a scalar in 2D and a matrix in 3D. This quadratic expression makes the wavefront of a beam hyperbolic.

The evolution of the shape of a Gaussian beam is determined by ordinary differential equations 2.22. The traveltime is found from the ray tracing system. The complex-valued M_{GB}, which controls the shape of the Gaussian beam, is computed by dynamic ray tracing. In isotropic media, this variation is governed by the second-order derivatives of the velocity field. In anisotropic media, it depends on the pertinent anisotropy parameters.

The procedure for paraxial GB modeling in anisotropic media is similar to the isotropic algorithm (Červený, 1985). First, the ray tracing method is applied to calculate the central rays from the source to the receiver and compute the traveltime and geometrical spreading. Second, these ray parameters are used to form single beams. Third, the single beams are summed together to obtain the whole wavefield. Finally, the source wavelet is applied to the beam summation results to generate the

seismograms.

Second-order Derivatives of the Complex Traveltime. The second-order derivative of the complex-valued traveltime M_{GB} (Červený, 1985) plays a significant role in the GB summation method. It can be determined from the ray propagator matrix by solving the dynamic ray tracing system, which calculates the complex beam parameters Q_{GB} and P_{GB} in equation 2.27 (Červený *et al.*, 1982; Červený & Pšenčík, 1983):

$$\begin{aligned} M_{GB} &= \mathrm{Re}(M_{GB}) + i\mathrm{Im}(M_{GB}). \\ &= P_{GB}\, Q_{GB}^{-1}. \end{aligned} \tag{3.5}$$

Here, M_{GB}, P_{GB}, and Q_{GB} are complex quantities satisfying the following conditions (Popov, 1982; Červený, 1985):

1. Q_{GB} is regular everywhere.
2. M_{GB} is symmetric.
3. $\mathrm{Im}(M_{GB})$ is positively defined.

The complex initial values automatically ensure the above conditions (Bleistein, 2009). An alternative way to obtain M_{GB} using the physical beam quantities is

$$\mathrm{Re}(M_{GB}) = \mathrm{Re}\left(\frac{P_{GB}}{Q_{GB}}\right) = \frac{K(R_r)}{V}, \tag{3.6}$$

$$\mathrm{Im}(M_{GB}) = \mathrm{Im}\left(\frac{P_{GB}}{Q_{GB}}\right) = \frac{2L(R_r)^2}{\omega}, \tag{3.7}$$

where $K(R_r)$ is the curvature of the beam wavefront of the beam, and $L(R_r)$ is the frequency-dependent effective half-width of the beam (Figure 3.1).

3.3 Summation of Beams

The wavefield is calculated by summing over all beams around receivers (Babich & Popov, 1990; Červený, 1982). The basic equation to describe this procedure is

$$\boldsymbol{u}(R,\omega) = \int_D \phi(\theta)\, \boldsymbol{u}_{GB}(R,\theta)\mathrm{d}\theta. \tag{3.8}$$

where, $\boldsymbol{u}_{GB}$ is the single-beam contribution from equation 3.1, $\phi(\theta)$ is the weighting factor, and D is a certain region around the receiver.

To obtain a good approximation for the wave equation, a proper weighting factor should be calculated for each beam. In addition, the parameters including the region of integration and the beam interval should be optimized to ensure both efficiency and accuracy.

3.3.1 Weighting Factor for 2D GB Summation

The weighting factor $\phi(\theta)$ plays a significant role in determining the amplitude of the wavefield. The weighting factor can be obtained by comparing the Green's function with the asymptotic GB expression in homogeneous media. Červený *et al.* (1982), and George *et al.* (1987) calculated the weighting factor for acoustic and isotropic media. For anisotropic media, it is difficult to obtain an explicit expression for the Green's function. Here, we represent the Green's function in 2D homogeneous anisotropic media using ray parameters such as geometrical spreading following Červený's (2001) derivation (Appendix C). The steepest-descent method is used to derive an asymptotic expression for the GB summation method in TI media in Appendix B. By equating the Green's function and the asymptotic expression, we obtain the following weighting factor for 2D TI media,

$$\phi(\theta) = \frac{i}{4\pi}\frac{\sqrt{(M-M_{GB})Q}}{\rho V}, \tag{3.9}$$

where Q is the ray-tracing geometrical spreading from equation 2.26, M and M_{GB} represent the second-order spatial derivatives of the ray tracing system and the GB system, respectively. If we simplify this expression for acoustic media, we obtain the same formula as Červený *et al.* (1982).

3.3.2 Beam Parameters

Before we calculate the wavefield generated by a line source, it is necessary to expand a plane wave into Gaussian beams (Červený, 1982). To form a plane wave using GB summation, the only required parameter is the beam interval (Červený, 1982; Hill, 1990). If the beam interval is smaller than the half-width of the beams, we obtain a good approximation for plane waves. For point or line sources, there are more parameters to consider including the beam angle coverage, interval, and width. The beam intervals and ranges are determined by the ray-tracing procedure. The beam width can be controlled in the beam forming step.

1. Angle range

   Ideally, the angle range for the beam summation method should be from $-\pi$ to π. However, this is not realistic for computational reasons. The question is how large the angle range should be to maintain accuracy in beam summation. We investigate the relationship between the amplitudes and angle range in the numerical tests below. Note that the angle range should be symmetric at the receiver.

   First, we test the results for the acoustic case. The summation of Gaussian beams is compared to the exact solution of the wave equation for a line source (Červený *et al.*, 1982). The acoustic Green's function (Červený *et al.*, 1982) is

$$u(r,\omega) \sim -\frac{1}{4}\sqrt{\frac{2V}{\pi\omega r}}\exp\left(i\frac{\omega r}{V}+i\frac{\pi}{4}\right). \tag{3.10}$$

   Here, $u(r,\omega)$ is the displacement for the frequency ω, r is the distance from the source to the receiver, and V is the velocity. The ratio of the Green's function and the amplitude from beam summation is calculated as a function of the angle range in Figure 3.3. As shown in Figure 3.3, when the angle range is small, the GB amplitude deviates from the Green's function. But once the maximum angle exceeds 15°, the beam-summation errors are smaller than 3%. Next, we test the influence of the angle range on P-wave GB amplitudes in a homogeneous anisotropic medium (Figure 3.4). The X- and Z-component of displacement are computed using the FD method for comparison with the GB

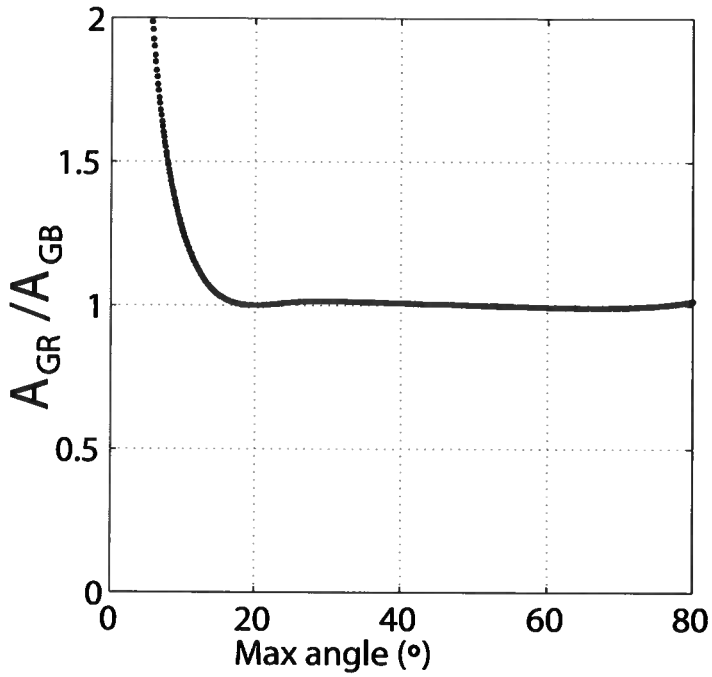

Figure 3.3: Ratio of the Green's function and the GB amplitude. The horizontal axis is the range of angles used in the beam summation.

summation method (Figure 3.5). Because it is difficult to plot the FD and GB seismograms at the same scale, the relative amplitudes are shown in Figures 3.6 and 3.7. The seismograms from the GB summation method closely match those computed by FD. Figures 3.6 and 3.7 show that the GB summation method produces a good approximation if the angle range exceeds 15°. This limitation may pose problems for more complex models. When the structure is complex, the angle coverage may not be sufficient angle coverage, which could distort GB amplitudes.

2. Beam interval

   The more beams are computed, the more accurate the results are. However, to maintain accuracy and efficiency, the optimal beam interval should be determined. Here, we test the beam interval for acoustic media. An optimized beam angle interval required to form a local plane wave was defined by Hill (1990, 2001). If the beam interval is small and the spherical wave is assumed to be

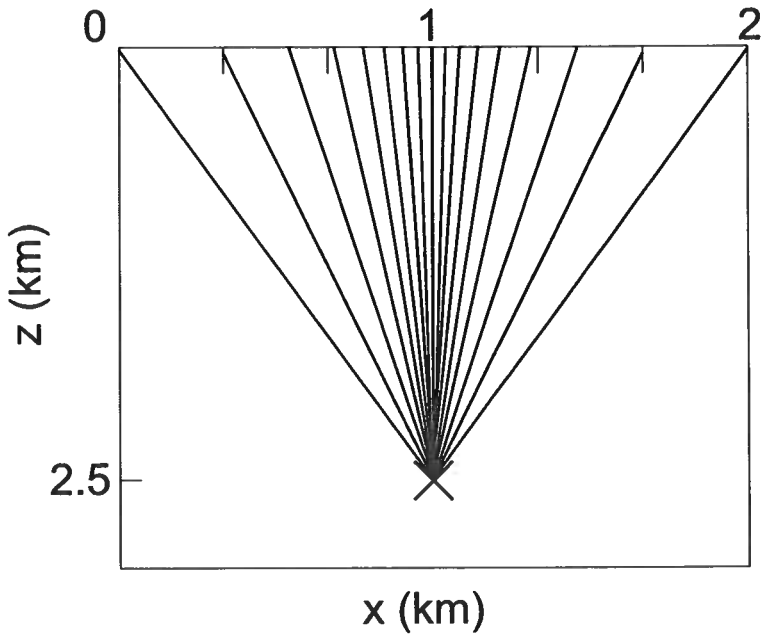

Figure 3.4: P-wave raypaths in a VTI medium with $V_{P0} = 3.0$ km/s, $V_{S0} = 1.5$ km/s, $\epsilon = 0.2$, and $\delta = -0.2$. The source is marked by the cross; the receivers are located at the surface.

locally equivalent to a plane wave, the GB summation should be close to the FD results. Here, we modify the expression from Hill (1990) by introducing a free parameter for anisotropic media.

To obtain accurate amplitudes, the beam interval (Hill, 1990) should satisfy

$$|\delta p_1| \leq \frac{\pi \cos\theta}{w_0\sqrt{\omega\omega_r}}, \tag{3.11}$$

where δp_1 is the horizontal slowness interval, w_0 is the initial beam width, ω is the angular frequency, ω_r is the reference angular frequency, and θ is the takeoff phase angle for the slowness vector $\boldsymbol{p}$.

Expressing $p_1 = \sin\theta/V$ and assuming $\omega < \omega_{peak}$, an alternative expression for the angle interval can be written as

$$|\delta\theta| \leq \frac{\lambda}{2nw_0}. \tag{3.12}$$

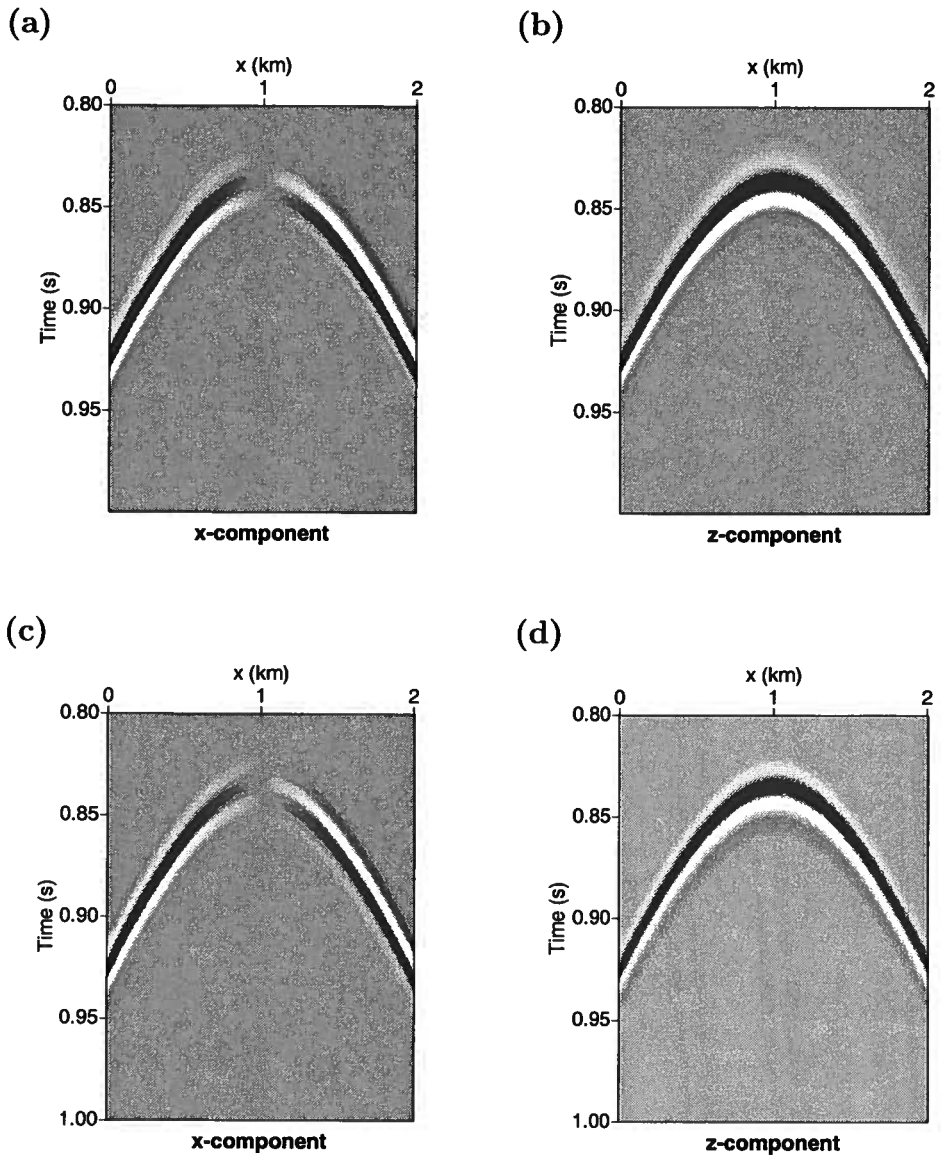

Figure 3.5: P-wave seismograms for the VTI model from Figure 3.4. (*a*) and (*b*) are the X- and Z-component seismograms computed with the FD method. (*c*) and (*d*) are computed with the GB summation method.

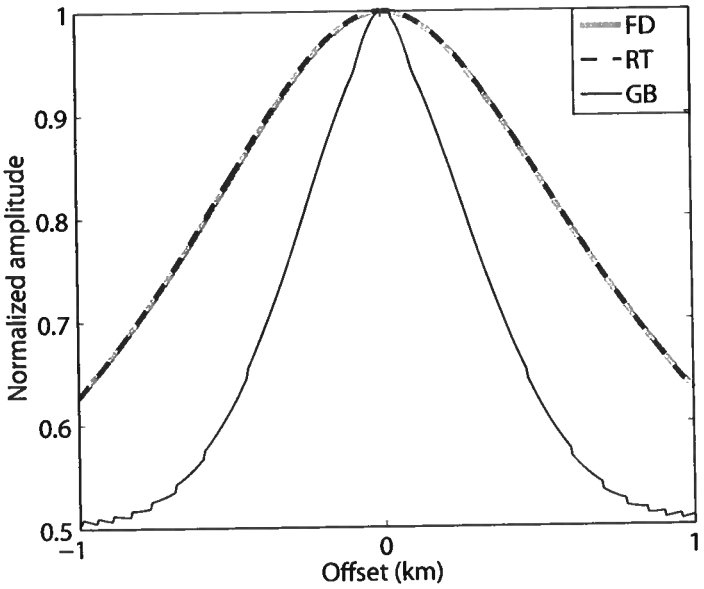

Figure 3.6: Z-component amplitudes computed by the finite-difference method (FD), the ray tracing method (RT), and the GB summation method (GB). The GB amplitudes are computed for a maximum angle of 10°.

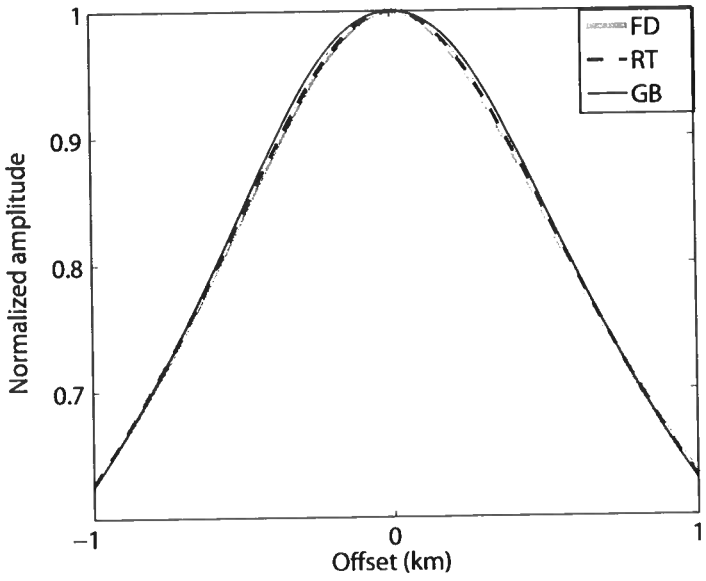

Figure 3.7: Same as Figure 3.6, but for a maximum angle of 15° for GB.

If we choose the initial beam width $w_0 = \lambda$ as suggested by Hill (1990), the above equation becomes

$$|\delta\theta| \leq \frac{1}{2n}. \tag{3.13}$$

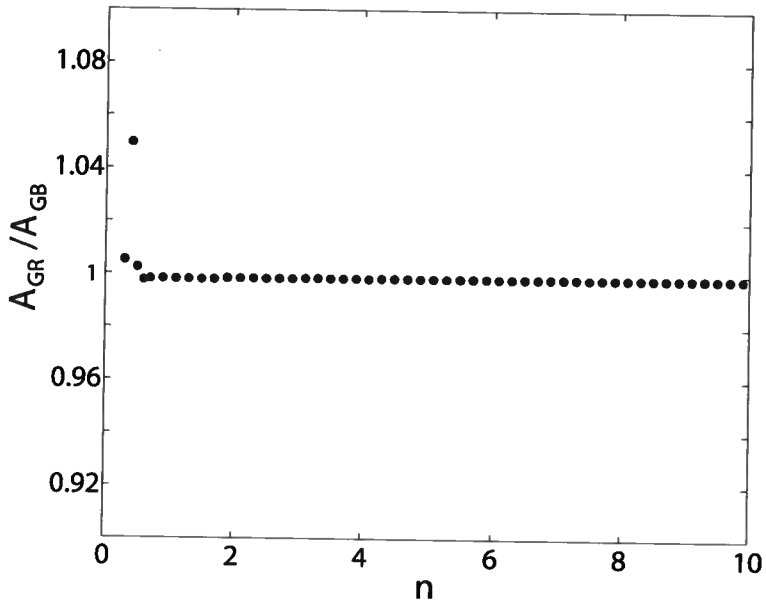

Figure 3.8: Ratio of the Green's function and the Green's function amplitude. The parameter n is responsible for the beam angle interval (see equation 3.12).

Figure 3.8 shows that the GB amplitude converges toward the Green's function for acoustic media when the parameter $n > 2$. For anisotropic media, the value of n should be generally larger. In the following tests, we set $n = 10 - 50$ to ensure the high accuracy of GB summation.

3. Beam width

A Gaussian beam in a homogenous isotropic media is shown in Figure 3.9. The beam width $w(r)$ is described by a hyperbolic function (Meschede, 2007):

$$w(r) = w_0\sqrt{1 + \left(\frac{r}{r_R}\right)^2}, \tag{3.14}$$

where the parameter r_R is the Rayleigh range expressed as $r_R = \frac{\pi w_0^2}{\lambda}$, and λ is

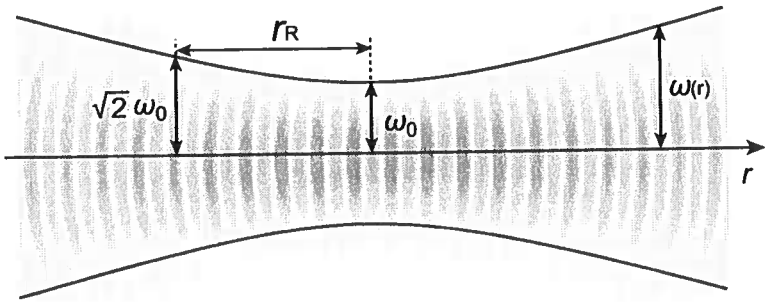

Figure 3.9: Gaussian beam propagating in a homogeneous medium. The GB width $w(r)$ changes with the axial distance r. w_0 is the beam "waist", and r_R is the Rayleigh range.

the wavelength.

The accuracy of GB approximation depends not only on the model, but also on the spatially varying beam shape (Červený *et al.*, 1982; Červený, 1985; Hill, 1990; Kravstov & Berczynski, 2007). Because of the paraxial nature of a Gaussian beam, the summation method is accurate if the beam is narrow. However, equation 3.14 shows that if the initial beam width is small at the source, it increases quickly with distance. Conversely, if the initial beam width is large, it increases slowly. Therefore, it is necessary to determine an optimal initial beam width.

The beam width can be evaluated by two different methods, using either the initial width at the source (Hill, 1990) or the final width at the receiver (Babich & Popov, 1990; Červený *et al.*, 1982). Both methods are generally suitable for beam modeling.

To determine the initial beam width at the source, it is convenient to use the initial values of the ray parameters P_{GB0} and Q_{GB0} for isotropic media (Hill, 1990):

$$\begin{aligned} P_{GB0} &= \frac{i}{V_0}, \\ Q_{GB0} &= \frac{\omega_r w_0^2}{V_0}. \end{aligned} \tag{3.15}$$

Here V_0 is the initial velocity, ω_r is the reference angular frequency, and w_0 is

the initial beam width which has the following optimized value (Hill, 1990):

$$w_0 = 2\pi V_a/\omega_r, \tag{3.16}$$

where V_a is the average velocity along the raypath. Equation 3.16 is derived for isotropic heterogeneous media (Hill, 1990). For anisotropic media, we set $V_a = V_0$ (V_0 is the P- or SV-wave velocity in the symmetry direction), $\omega_r = 2\pi f_{peak}$, and use a free parameter m:

$$w_0 = 2m\pi V_0/\omega_r. \tag{3.17}$$

The influence of the parameter m on the accuracy of GB modeling for isotropic

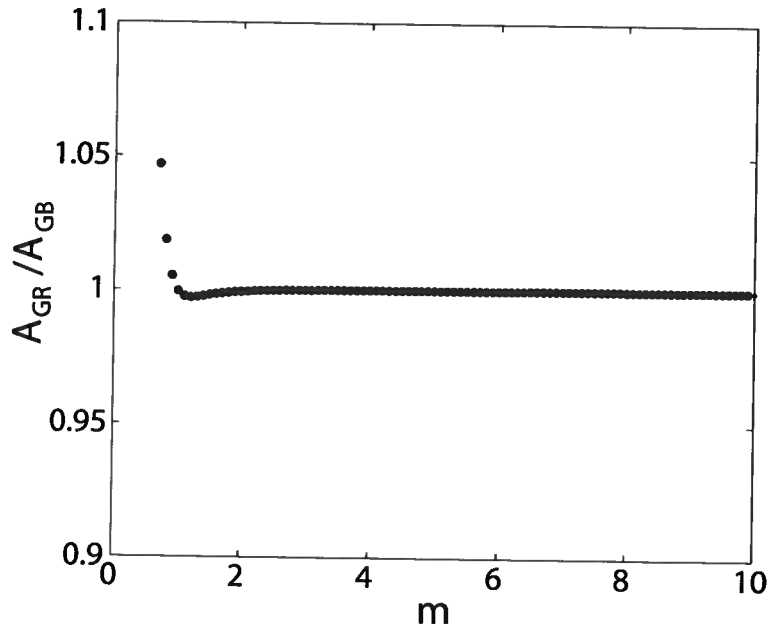

Figure 3.10: Amplitude ratio between beam summation and the Green's function for an acoustic model for different initial beam-widths. The initial beam width is indicated by equation $w_0 = 2m\pi V_0/\omega_r$.

media is illustrated in Figure 3.10. Values of $m > 2$ provide a good approximation for the exact amplitudes. The complex initial values in equation 3.15 ensure the absence of singularities on the central ray.

Another method for controlling the beam width is to introduce a certain com-

plex parameter at the receiver (Popov, 1982; Červený *et al.*, 1982). The corresponding initial beam width is obtained by minimizing the beam width at the receiver:

$$w_0^{opt} = \sqrt{\frac{2V_0}{\omega}}\sqrt{\left|\frac{Q_2}{Q_1}\right|}. \tag{3.18}$$

Here Q_1 and Q_2 are the components of the propagator matrix for dynamic ray tracing in equation 2.26, and V_0 is the symmetry-direction velocity at the source. This method yields the parameter using m_{opt} which corresponds to the following initial complex ray parameters:

$$\begin{aligned} P_{GB0} &= \frac{1}{V_0}, \\ Q_{GB0} &= i\frac{\omega_r w_0^2}{2V_0}. \end{aligned} \tag{3.19}$$

Figure 3.11 shows the beam width at the receivers for a VTI model in Figure

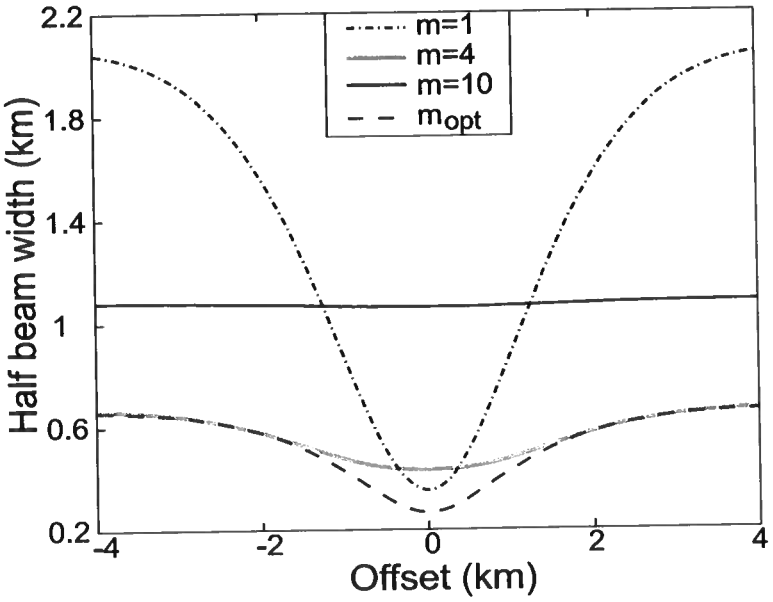

Figure 3.11: Beam width at the receiver locations for different initial beam widths for P-wave from model in Figure 3.4. The parameter m is defined in equation 3.17.

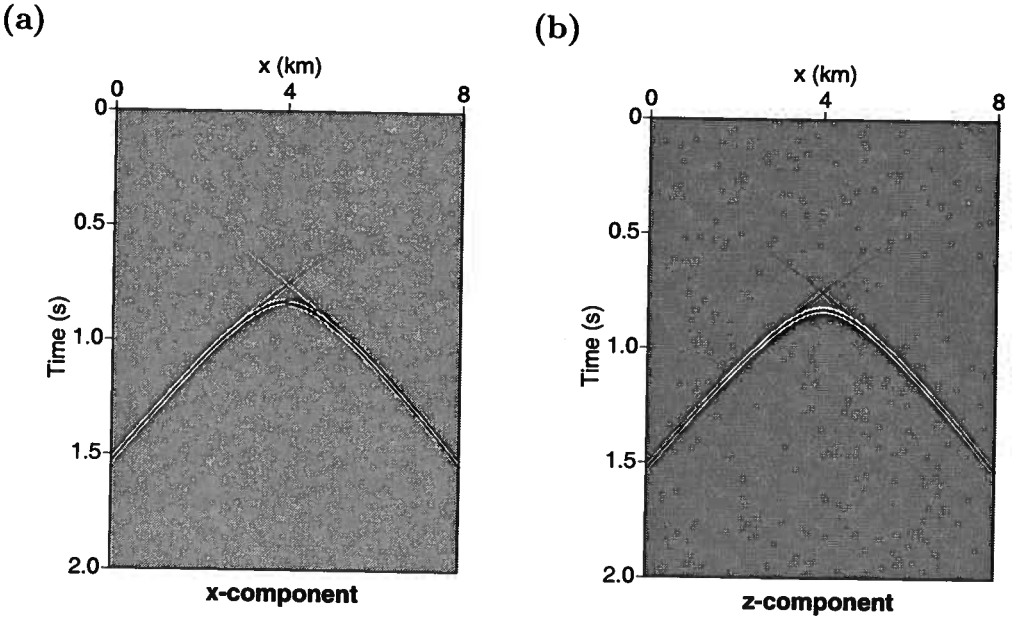

Figure 3.12: P-wave seismograms for a VTI medium from the model from Figure 3.4; $m = 1.0$. The beam widths at receivers are shown in Figure 3.11.

3.4. If the initial beam width is small, it increases quickly along the ray path ($m = 1$ in Figure 3.11). If the initial beam width is large ($m = 10$), it increases slowly. The corresponding P-wave seismograms are shown in Figures 3.12 - 3.15. The seismograms with the optimized m in Figure 3.15 are clean without noise because the beams at the receivers are sufficiently narrow. There are noise due to the too wide beam width from narrow initial beams in Figure 3.12. The beam widths corresponding to $m = 4.0$ and $m = 10.0$ ensure clean and accurate seismograms.

3.4 Amplitude for GB Modeling

At any point along the ray, the GB amplitude is controlled by the complex-valued parameter M_{GB} (Červený & Pšenčík, 2009). In anisotropic media, the complex amplitude of a single Gaussian beam for P- or SV-waves is expressed as (Červený &

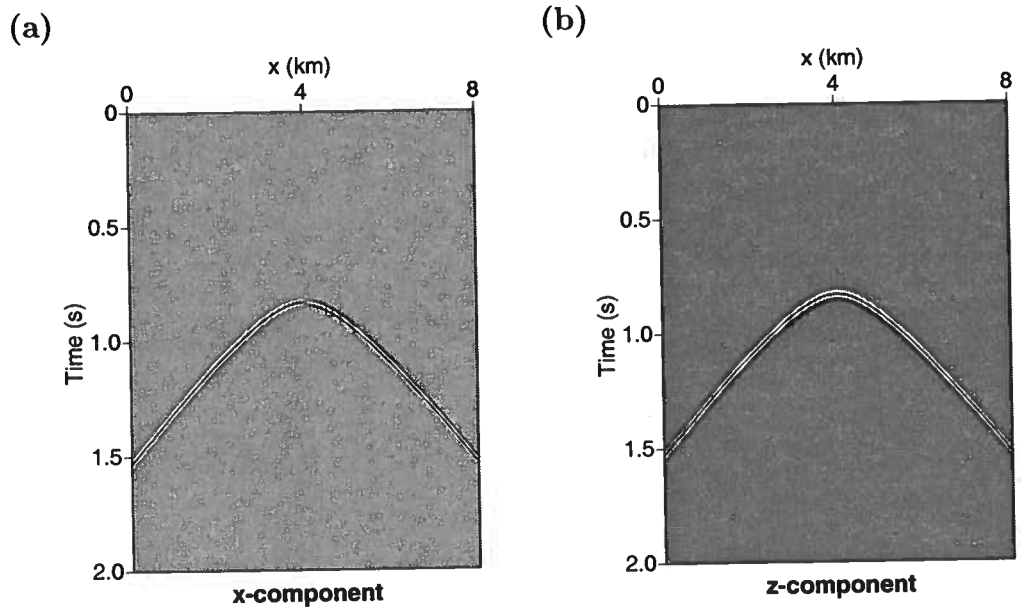

Figure 3.13: Same as Figure 3.12 for $m = 4.0$.

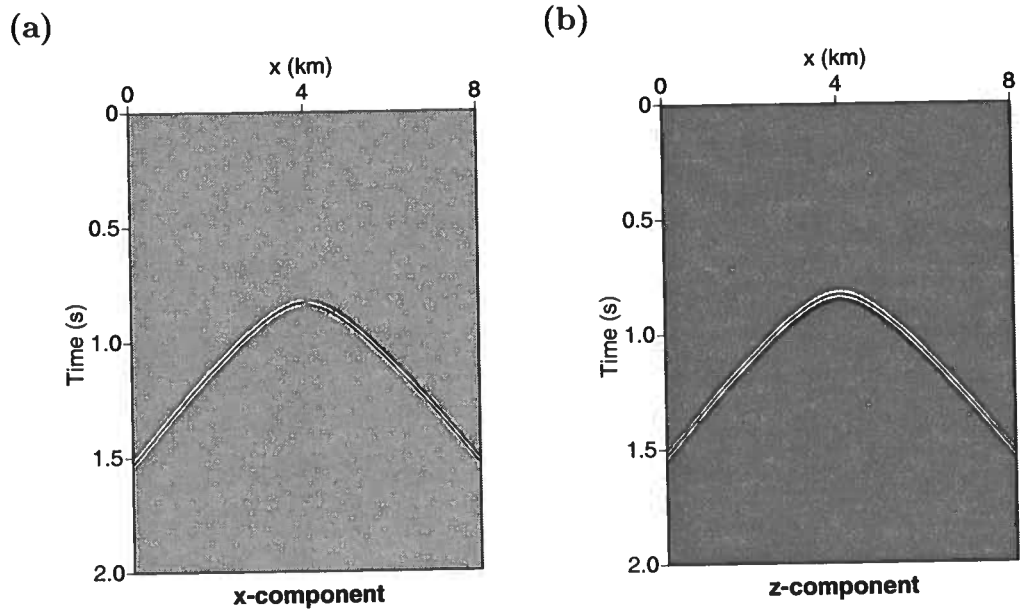

Figure 3.14: Same as Figure 3.12 for $m = 10.0$.

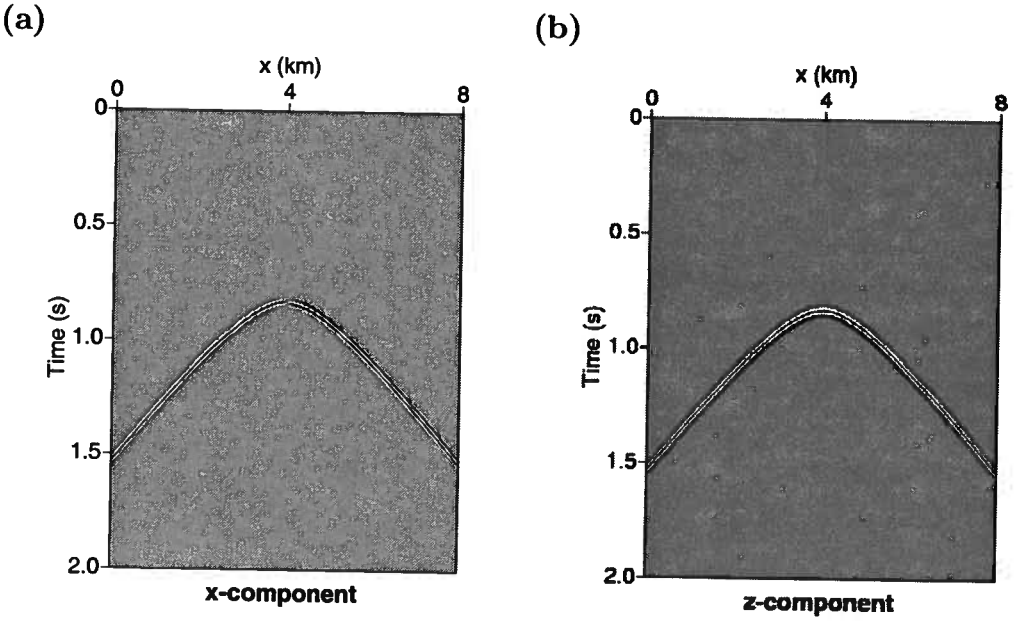

Figure 3.15: Same as Figure 3.12 for m_{opt}.

Pšenčík, 2009)

$$\boldsymbol{U}_{GB} = A\boldsymbol{g} \exp\left[-\frac{1}{2}\,\omega\, y^2 \mathrm{Im}(M_{GB})\right]. \tag{3.20}$$

Here A is the amplitude determined by dynamic ray tracing:

$$A = A_0 T \sqrt{\frac{V_0\,\rho_0\,Q_0}{V\,\rho\,Q_{GB}}}, \tag{3.21}$$

where ρ_0 , V_0, and Q_0 are the density, phase velocity, and complex geometrical spreading at the source. ρ , V, and Q are the same quantities at the receiver. A_0 is the initial amplitude, and T is the product of the reflection and transmission coefficients.

3.5 Synthetic Seismograms

There are three ways to obtain synthetic seismograms using the GB method:

1. Direct beam summation in the time domain.

2. Frequency-domain multiplication with the source wavelet.

3. Convolutional approach.

The beam expression in the time domain used in the first method is not as simple as in the frequency domain because the beam shape is not Gaussian. Application of the convolutional approach is hindered by the fact that the beam parameters are complex numbers. Therefore, we use the second method based on frequency-domain multiplication because it is more direct and efficient for GB summation.

We multiply the GB expression in equation 3.8 with the source function and apply the inverse Fourier transform. The frequency-domain solution can be transformed into the time domain using the inverse Fourier transform

$$\boldsymbol{u}(R,t) = \int_{-\infty}^{\infty} X(\omega)\, \boldsymbol{u}(R,\omega) \exp[-i\omega t] \mathrm{d}\omega. \tag{3.22}$$

Here, $X(\omega)$ is the spectrum of the Ricker wavelet used as the source signal.

Chapter 4

GB summation for shear-wave cusps

4.1 Summary

Shear-wave cusps have already been observed in laboratory rock physics experiments and long-offset and VSP data (Slater *et al.*, 1993; Sondergeld & Rai, 1992). With growing interest in shear and converted waves, it becomes necessary to model cuspoidal wavefronts. However, difficulties in detection of cusps are caused not only by the multivalued traveltimes but also by uneven energy distribution along the wavefront. The ray tracing method breaks down at the edges of cusps because the amplitudes go to infinity. GB summation has been known to improve the performance of modeling and imaging algorithms in caustic regions. Here, we discuss the application of the GB summation method for simulating the SV-wave cuspoidal wavefronts in transversely isotropic (TI) media. The modeling results illustrate the improvements achieved by GB in describing the amplitudes and polarization along cuspoidal wavefronts.

4.2 Conditions for SV-wave Cusps in TI Media

In TI media, kinematic signatures of SV-waves are mainly determined by the parameter σ (equation 4.6). SV-wave cusps occur in homogeneous TI media when σ exceeds a certain critical value discussed below (Musgrave, 1970; Martynov & Mikhailenko, 1984; Thomsen & Dellinger, 2003; Vavrycuk, 2003, 2004). In homogeneous TI media, SV-waves have off-axis and on-axis triplications. Generally, off-axis triplications are approximately centered at an angle of 45° from the symmetry axis (Thomsen & Dellinger, 2003). On-axis triplications, which correspond to untypical negative values of σ, occur in the directions parallel and perpendicular to the

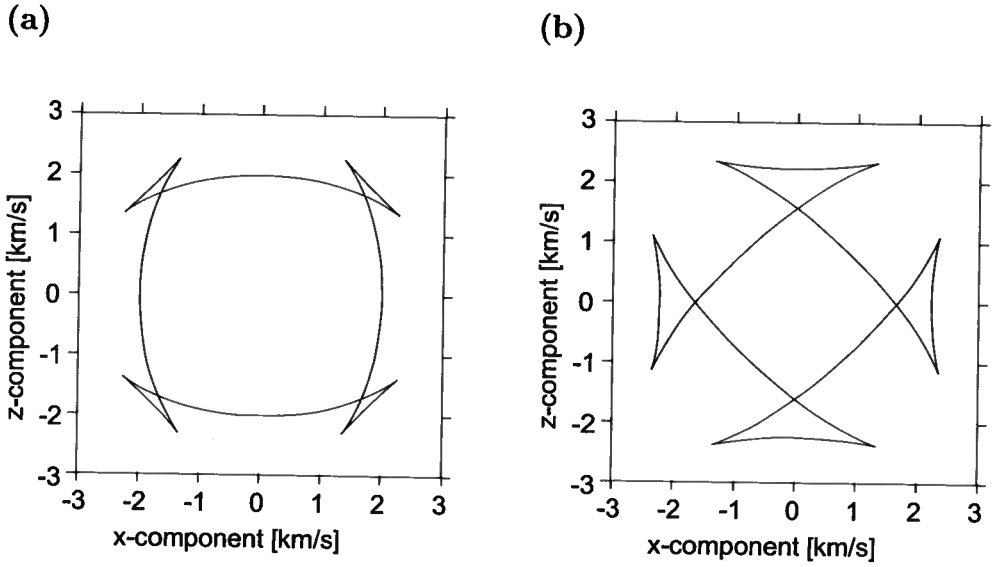

Figure 4.1: Triplication types in TI media (Vavrycuk, 2003). (a) off-axis triplications and (b) on-axis triplications.

symmetry axis.

The triplication conditions in TI media have been known for decades (Musgrave, 1970; Thomsen & Dellinger, 2003; Vavrycuk, 2004). The exact expressions for the triplication conditions in terms of the elastic moduli are quite involved. Several approximations are suggested by Thomsen & Dellinger (2003) and Vavrycuk (2003). Here, we review the expressions of Thomsen & Dellinger (2003) because their formulas are simple and give insight into the influence of the anisotropy parameters.

The ray angle ψ with respect to the symmetry axis can be expressed as the following function of the corresponding phase angle θ (Dellinger, 1991):

$$\psi = \theta + \tan^{-1}\left(\frac{\mathrm{d}V(\theta)/\mathrm{d}\theta}{V(\theta)}\right). \tag{4.1}$$

Here, $V(\theta)$ is the phase velocity at the takeoff angle θ.

Triplications occur when a certain ray direction is associated with more than one phase direction, which can be expressed as

$$\frac{\mathrm{d}\psi}{\mathrm{d}\theta} < 0. \tag{4.2}$$

Differentiating equation 4.1 to eliminate the ray propagation direction ψ and substituting the result into equation 4.2 yields

$$\frac{\mathrm{d}^2V(\theta)}{\mathrm{d}\theta^2} + V(\theta) < 0. \tag{4.3}$$

Explicit expressions for the triplication condition can be obtained using the anisotropy parameters ϵ, δ, and σ (Thomsen, 1986; Tsvankin, 2005):

$$\epsilon = \frac{C_{11} - C_{33}}{2C_{33}}, \tag{4.4}$$

$$\delta = \frac{(C_{13} + C_{55})^2 - (C_{33} - C_{55})^2}{2C_{33}(C_{33} - C_{55})}, \tag{4.5}$$

$$\sigma = \frac{C_{33}}{C_{55}}(\epsilon - \delta). \tag{4.6}$$

Substituting equation 4.6 and the exact shear-wave phase velocity (Tsvankin, 2005) into the inequality in equation 4.2 and setting $\theta = 0°$ leads to

$$\sigma < -0.5. \tag{4.7}$$

Similarly, the condition for triplications at $\theta = 90°$ becomes

$$\sigma < -0.5 - \delta + \frac{V_{S0}^2}{2V_{P0}^2}, \tag{4.8}$$

where V_{S0} and V_{P0} are the SV- and P-wave velocity in the symmetry direction, respectively. These two conditions for the on-axis triplications are exact.

The inequality for off-axis triplications is so involved that it cannot be solved exactly. If we assume that δ and $\frac{V_{S0}}{V_{P0}}$ are much smaller than unity, inequality 4.2 reduces to (Thomsen & Dellinger, 2003)

$$\sigma > \frac{2}{3}\left(1 + \delta - \frac{V_{S0}^2}{9V_{P0}^2}\right). \tag{4.9}$$

Generally, on-axis triplications occur for $\sigma < -0.5$ and off-axis cusps occur for relatively large values of σ in the range $0.8 - 1.0$. Several numerical examples for different values of σ are discussed in the next section.

4.3 Cusp Modeling Using GB Summation

Most rays concentrate near the edges of cusps, with relatively scarce illumination in the central triplication area. Cuspoidal edges on the wavefront can significantly complicate wavefields by producing energy focusing and phase shifting of signals. Using the ray-tracing method, it is difficult to obtain a good approximation for cuspoidal wavefields because amplitudes at the edges of cusps become infinite. Here, the GB summation method described in Chapter 3 is applied to SV-wave cusp modeling. The tests are conducted for three homogeneous TI models.

4.3.1 VTI Model with $\sigma = -0.8$

On-axis triplications are observed in SV-wave seismograms obtained by GB summation and finite differences in Figures 4.2, 4.3, and 4.4. The GB summation method produces seismograms similar to those generated by FD. When the initial beam width is too small ($m = 0.5$), the beam width at receivers becomes very large (Figure 4.9) and such wide beams introduce artifacts (Figure 4.2). With increasing initial beam width, the artifacts disappear, and the seismograms look similar to the ones obtained by finite differences. The excellent agreement between the GB and FD results shows that the GB method can provide a close approximation for the exact solution of the wave equation. The amplitudes at the edges of the cusp computed by the GB method are finite but not exact. The X- and Z-component amplitudes for two branches of SV-wave cusps are compared in Figure 4.7. The amplitude errors at the edges of the cusp for different values of m are shown in Figure 4.8. The maximum GB amplitude along the cusp is shifted slightly from the edges of cusps. The amplitude errors at the edge of the cusps converge toward 5% for the X-component and 30% for the Z-component as m increases. Although the error for the Z component is large, the total wavefield error is still less than 10% because the wave is polarized predominantly in the horizontal direction. The "optimal" value m_{opt} produces amplitudes with larger errors than the method based on changing the initial beam widths. Therefore, al-

though seismograms produced using m_{opt} do not have artifacts, the amplitude errors for the cusps are large.

The beam width at the receivers is shown in Figure 4.9. The optimized beam width produces a narrower beam than that for other values of m. The beam width of a narrow beam at the source ($m = 0.5$) increases quickly, while that of a wide beam at the source ($m = 4.5$) increases slowly. Although wide beams produce almost the same amplitudes as those shown in Figures 4.7 and 4.8, they may cause artifacts in the seismograms (Figures 4.2). Therefore, the initial beam width should not be too small or too large to maintain the accuracy of the GB method.

4.3.2 VTI Model with a Large Positive σ

A model with a large positive value of σ is tested next. GB summation reproduces the whole cuspoidal wavefront with finite amplitudes at the edges of the cusp. Figures 4.10 - 4.12 show the X- and Z-component seismograms computed by the FD method and GB summation with different initial beam widths. As was the case for $\sigma < 0$, the GB method provides a good approximation for the exact wavefield. The X- and Z-component amplitudes for one of the branches (Figure 5.4) of the cusp are plotted in Figure 4.15. Despite some deviations, the amplitudes computed by the GB method are close to those from the FD method. To obtain a good amplitude approximation, m should be larger than 2. Notice that the amplitudes at the edge of the cusps are not necessarily large because they are influenced by several factors including polarization, source spectrum, and the reflection/transmission coefficients for heterogeneous media.

As shown in Figure 4.11 and 4.12, beams that are too narrow or too wide at the source cause artifacts on the GB seismograms. As discussed above, when m is small ($m = 0.5$), the beam width increases quickly and becomes too large at the receivers, causing artifacts at the edges of the cusps (Figure 4.11). When the initial beam width is too large ($m = 10$), it increases slowly but is still too large at the receivers to produce a clean seismogram (Figure 4.12). Therefore, the initial beam width should be neither too small nor too large to maintain the accuracy of the GB summation method. For modeling of SV-wave cusps, the optimal range for the initial beam width should be $m = 2.0 - 8.0$.

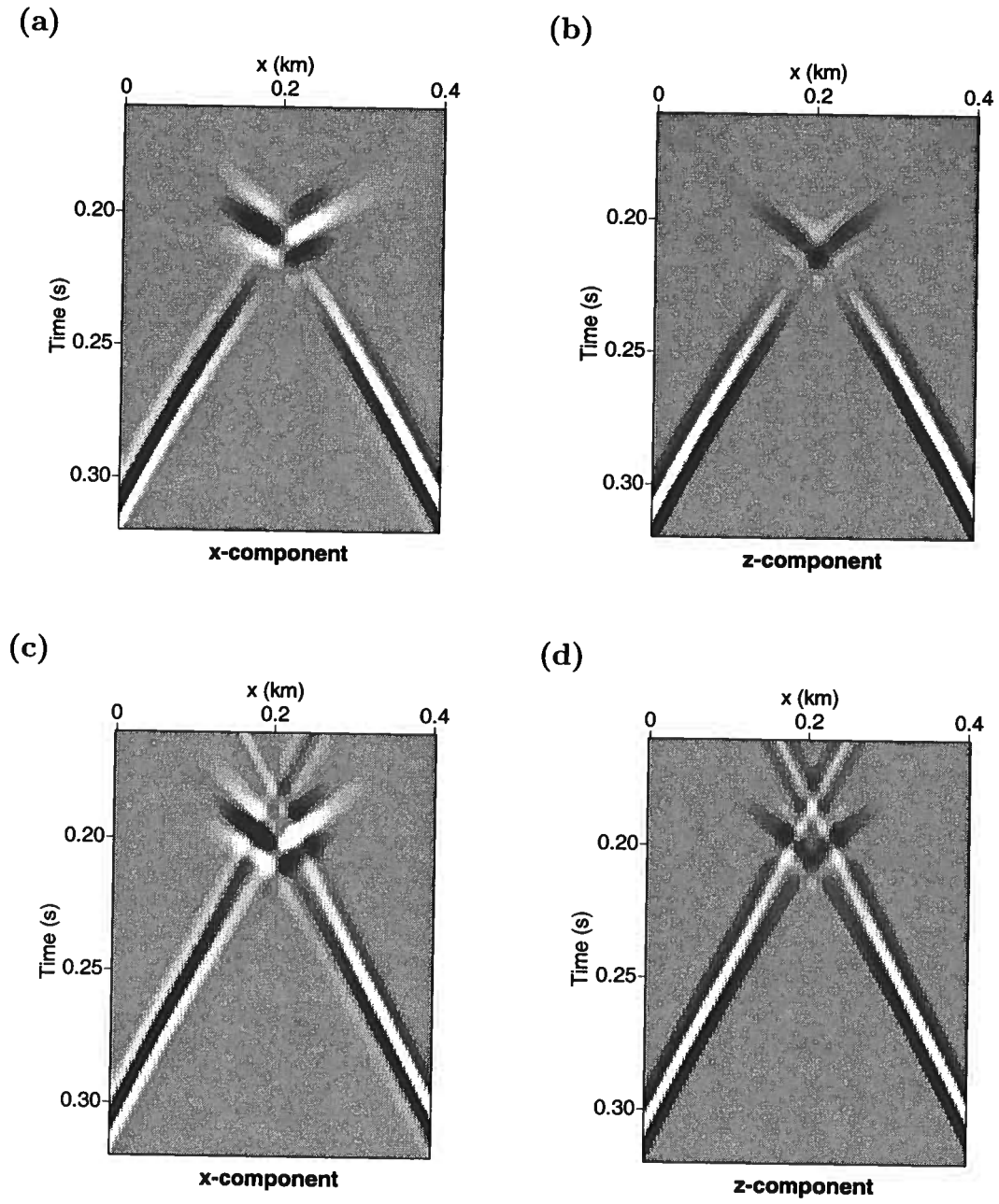

Figure 4.2: SV-wave seismograms for VTI media with the parameters $V_{P0} = 3.0$ km/s, $V_{S0} = 1.5$ km/s, $\epsilon = -0.1$, $\delta = 0.1$, and $\sigma = -0.8$. A line source is located at a depth of 0.3 km and direct SV-waves are recorded at the surface. Figures (a) and (b) are the X- and Z-component seismograms calculated by FD modeling. Figures (c) and (d) are obtained by GB modeling with the initial beam width parameter $m = 0.5$ (equation 3.17).

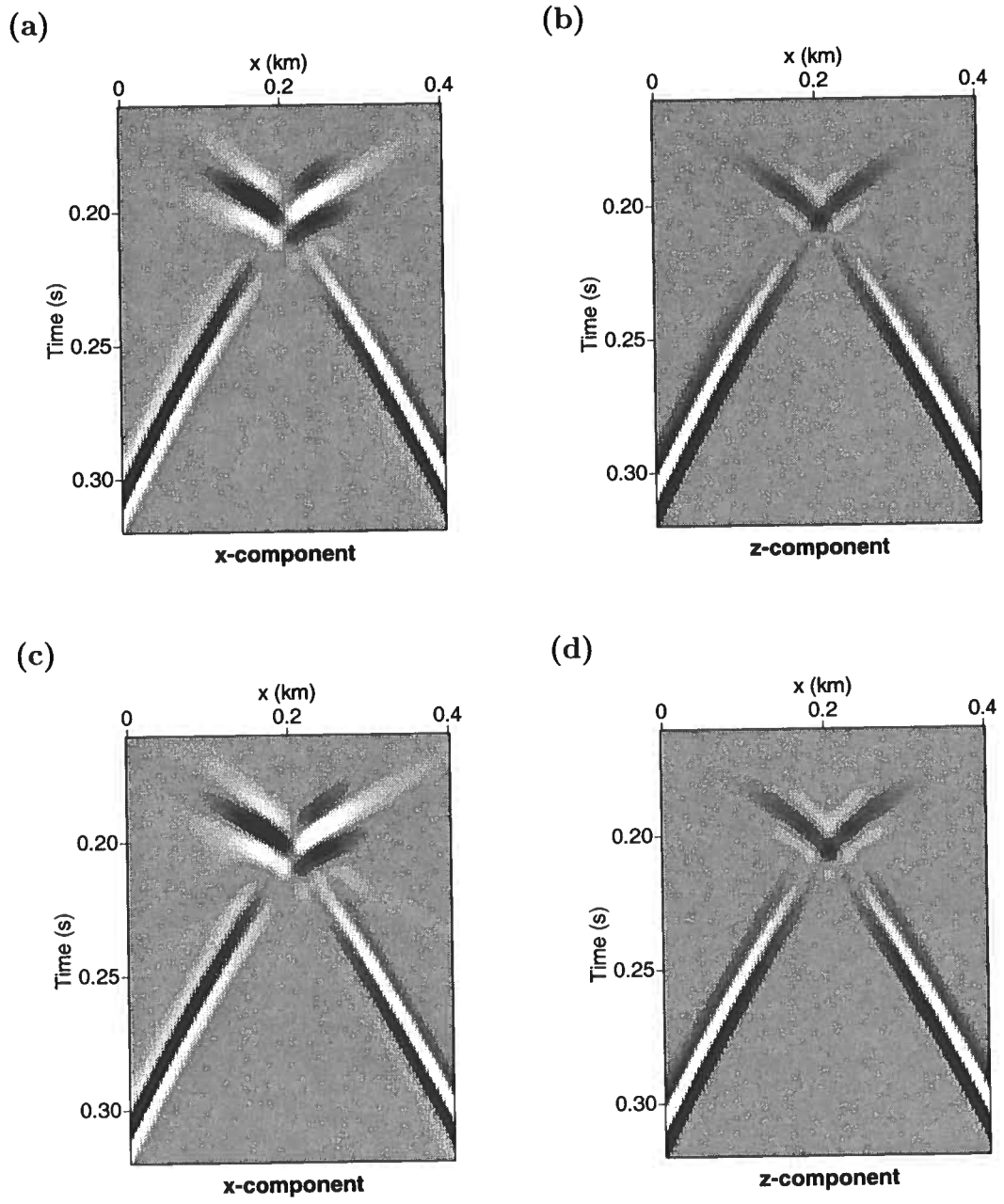

Figure 4.3: Wavefields generated by GB modeling for the model from Same as Figure 4.2. Figures (a) and (b) are the X- and Z-component seismograms for $m = 2.5$. Figures (c) and (d) are for $m = 4.5$.

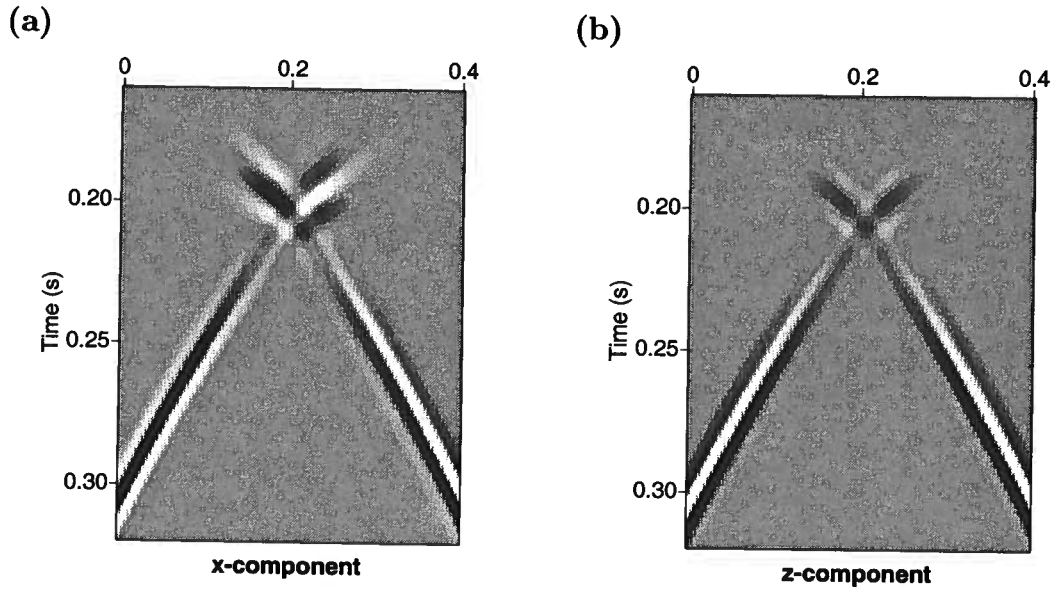

Figure 4.4: Seismograms for the model in Figure 4.2 obtained by the GB method for the optimized initial beam width m_{opt}.

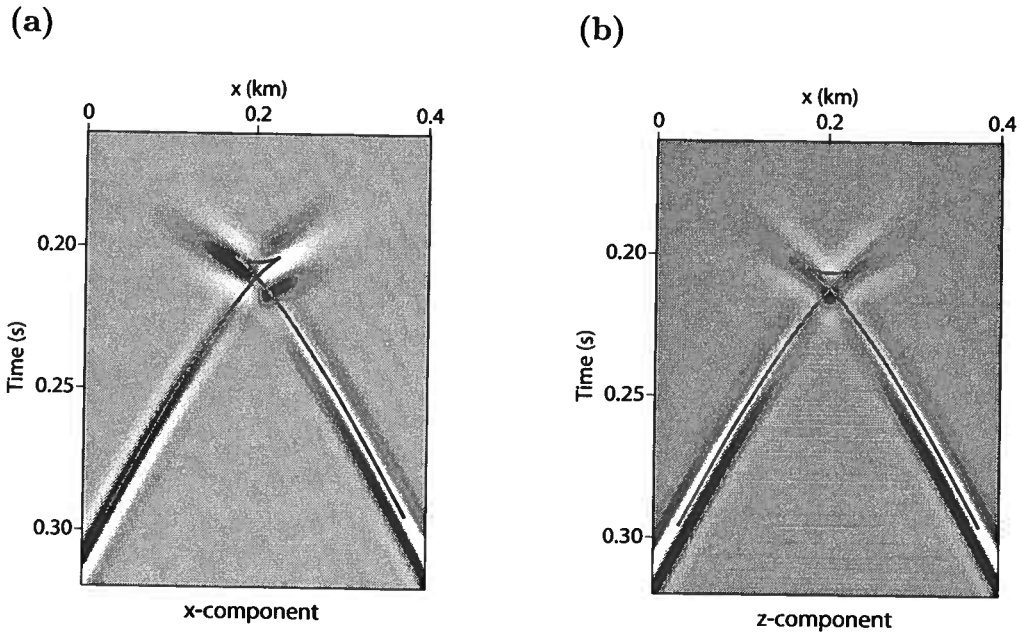

Figure 4.5: Seismograms and group-velocity surface for the model in Figure 4.2.

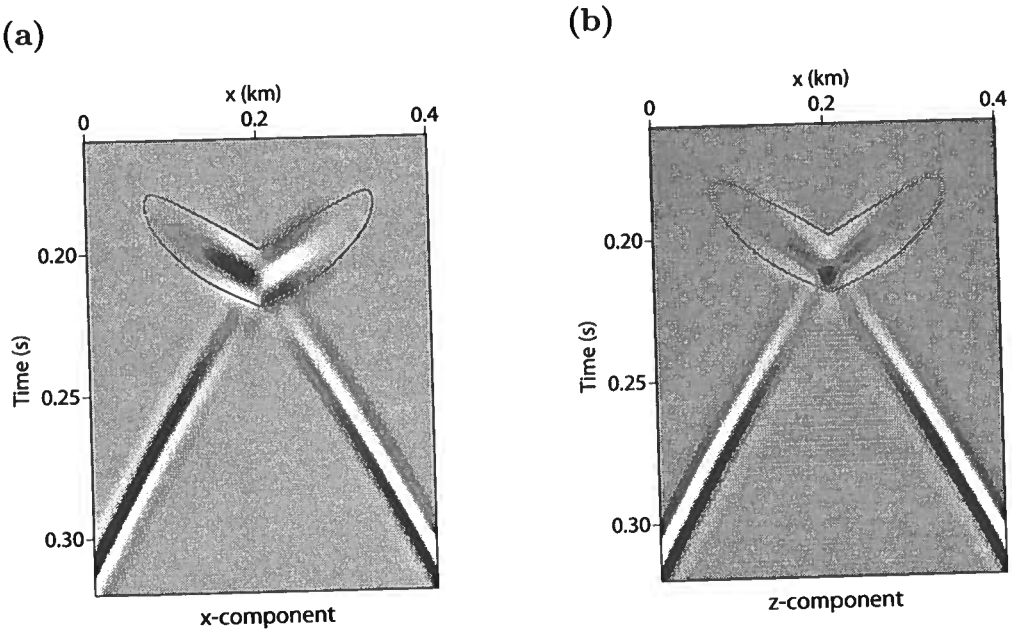

Figure 4.6: Branches of the cusp used in the amplitude comparison in Figure 4.7.

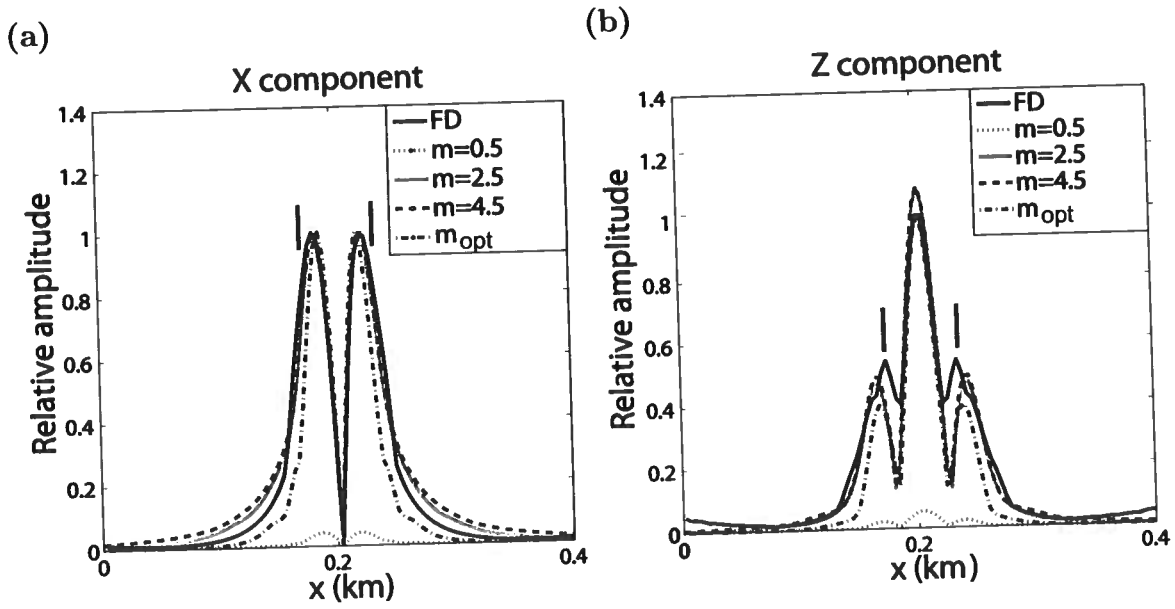

Figure 4.7: Amplitude comparison for the two branches of the cusp in Figure 4.6 (a) the X-component and (b) the Z-component. The vertical marks indicate the locations of the edge of the cusp.

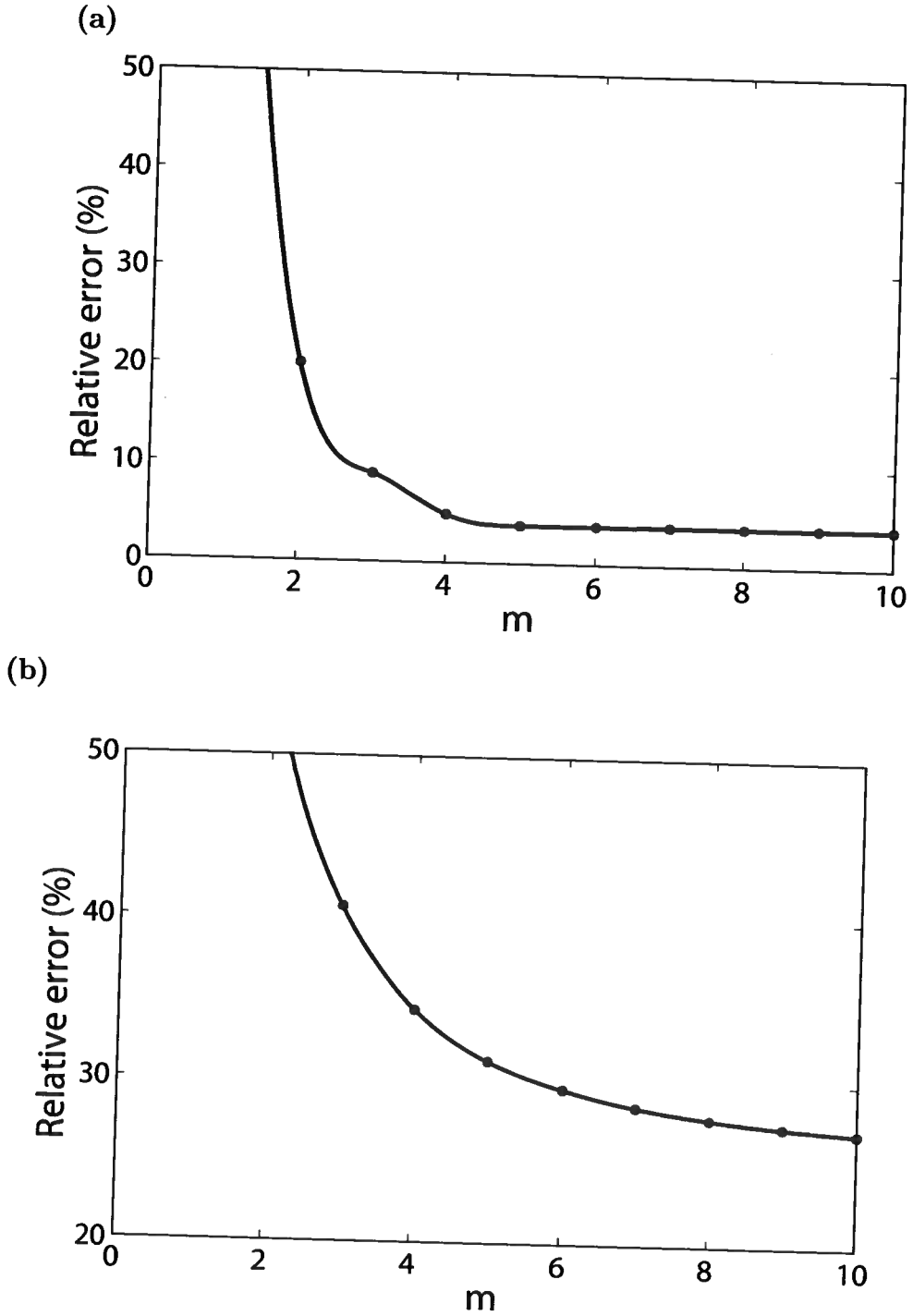

Figure 4.8: The relative errors of the X- (a) and Z- (b) component amplitudes at the edge of cusps in Figure 4.7 as functions of m.

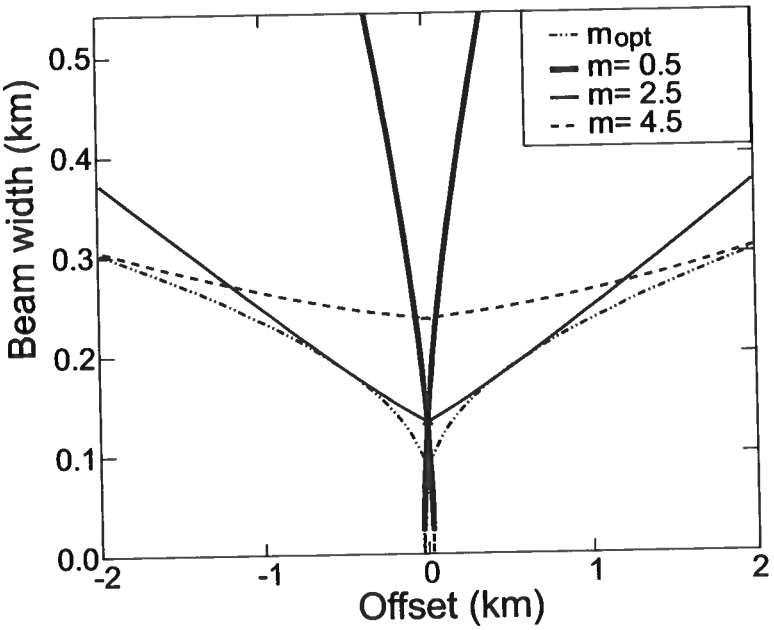

Figure 4.9: Beam width as a function of offset for the whole 4 km $\times$ 0.3 km model for $m = 0.5, 2.5, 4.5$, and the optimized beam width.

4.3.3 Physical TTI Model

Transverse isotropy with a tilted symmetry axis (TTI media) describes dipping shale layers near salt domes and fold-and-thrust belts such as the Canadian Foothills (Isaac & Lawton, 1999). The parameters V_{P0}, V_{S0}, ϵ, and δ for TTI media are defined in the rotated coordinate system with respect to the symmetry axis, in which the orientation is defined by the tilt ν and azimuth β. SV-wave cusps rotate along with the symmetry axis.

Dewangan *et al.* (2006) used physical-modeling reflection data from a phenolic sample (assumed to be TTI) to test their multicomponent moveout-inversion method. The sample was approximated by a horizontal TI layer with a tilted symmetry axis. To verify the inversion results, they conducted a transmission experiment by placing a horizontal source at the bottom of the sample (Figure 4.16). The transmitted SV-wave exhibits a prominent cusp near the 45° angle with respect to the symmetry axis ($\sigma > 0$). Here, we apply GB summation to compute the cusp for the physical model in Figure 4.16. Figure 4.17 shows the transmitted shear-wave raypaths.

GB summation reproduces the cusp and other major features of the transmitted

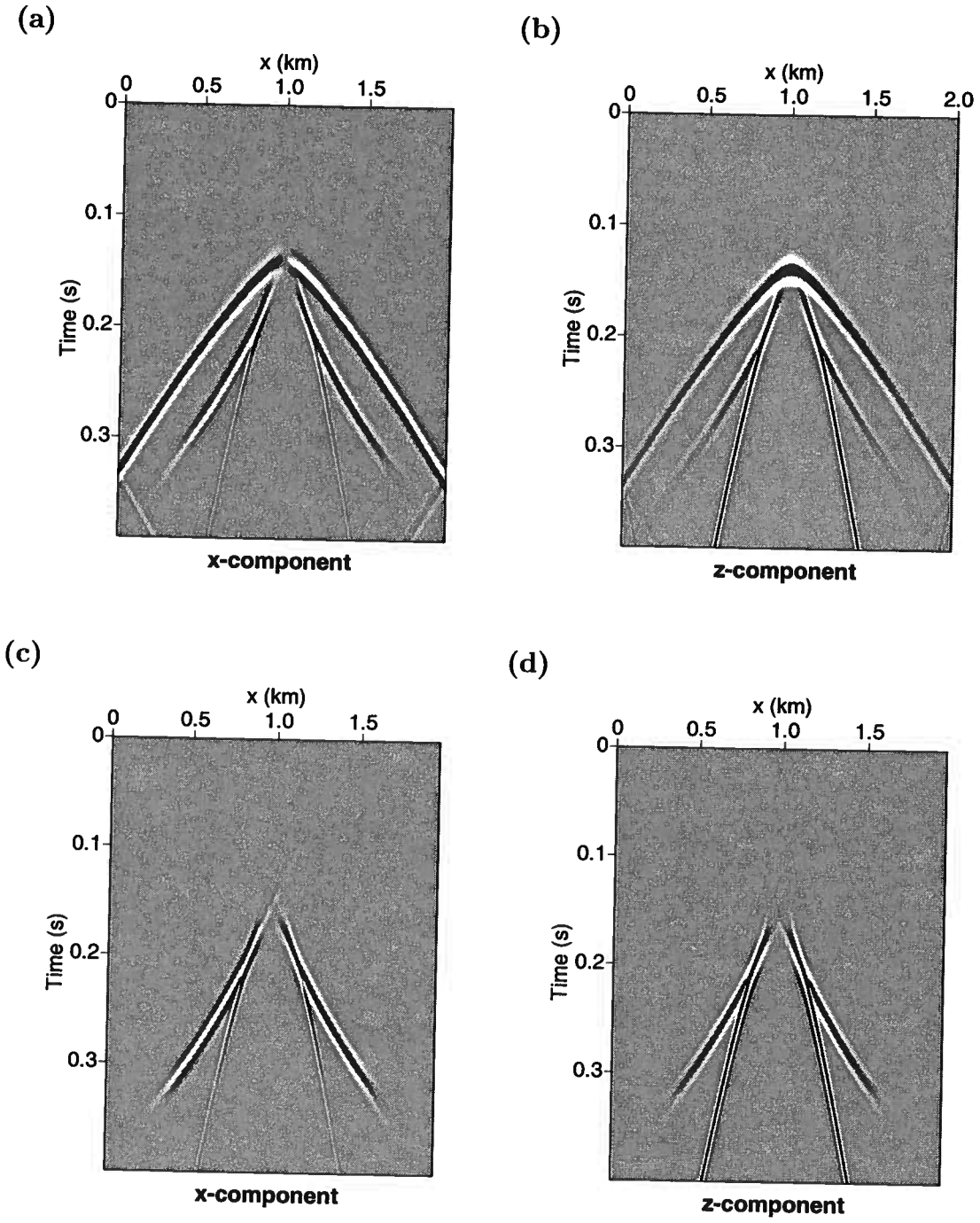

Figure 4.10: Seismograms for a 2 km $\times$ 0.3 km VTI model with $V_{P0} = 2.0$ km/s, $V_{S0} = 1.17$ km/s, $\epsilon = 1.1$, $\delta = -0.06$, and $\sigma = 3.38$. The source is located at point $(1.0, 0.3)$ km. The receivers are located at the surface. Plots (a) and (b) are the X- and Z-component seismograms obtained by FD modeling; (c) and (d) are the X- and Z-component seismograms obtained by GB summation using m_{opt}.

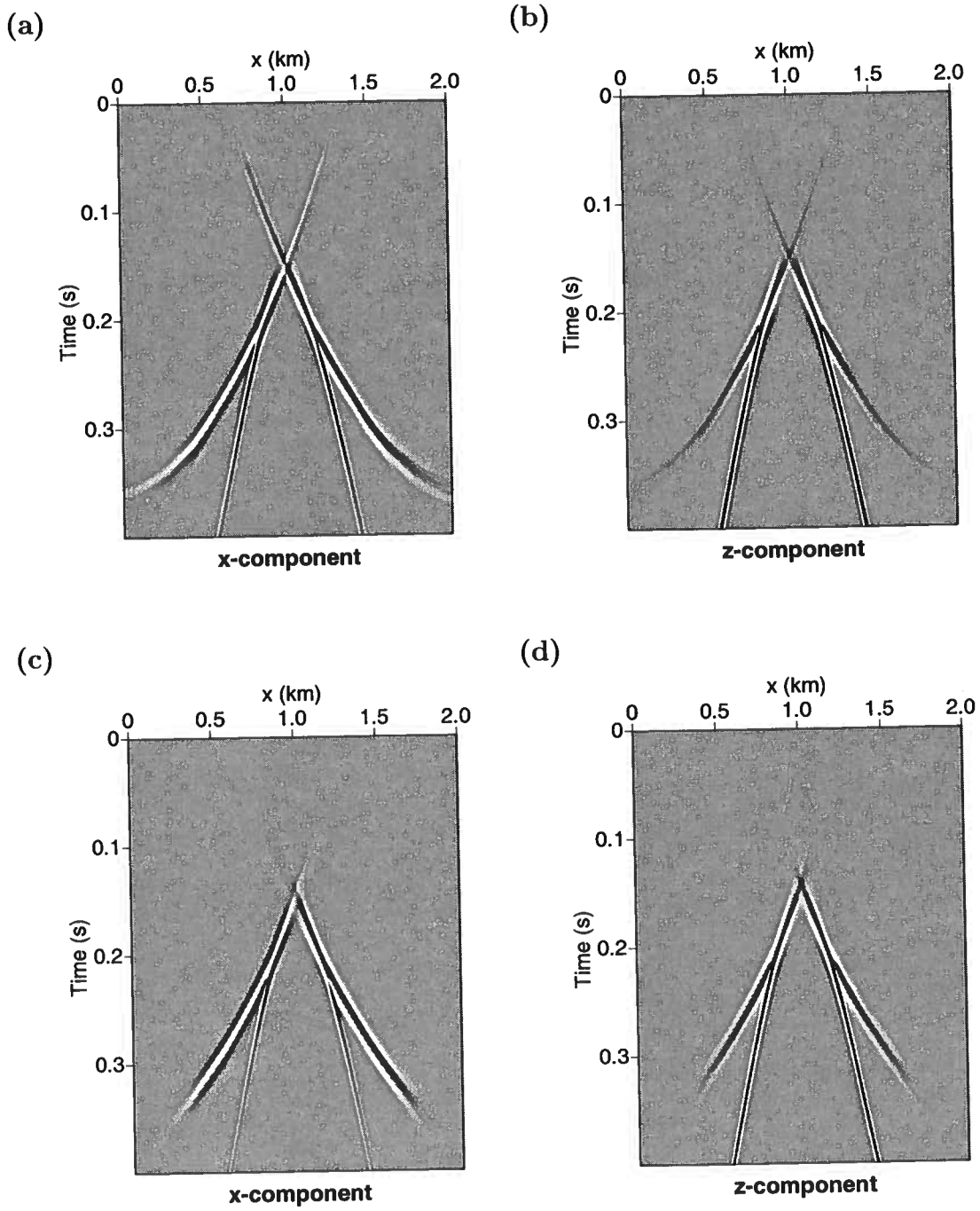

Figure 4.11: GB summation results for the model from Figure 4.10. (a) and (b) are X and Z component seismograms for $m = 0.5$; (c) and (d) are for $m = 2.5$.

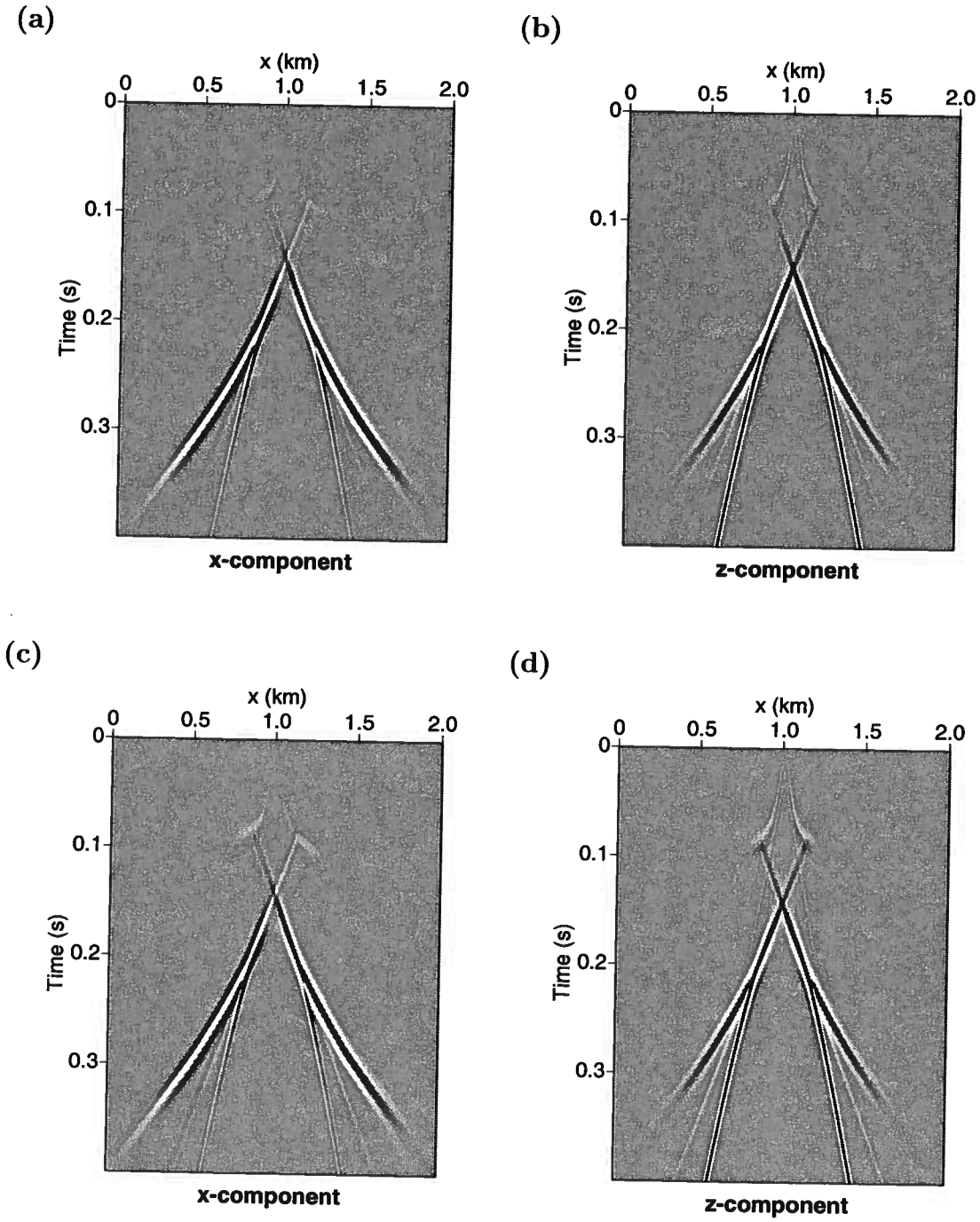

Figure 4.12: Same as Figure 4.11. (a) and (b) are X- and Z-component seismograms for $m = 4.5$; (c) and (d) are for $m = 10$.

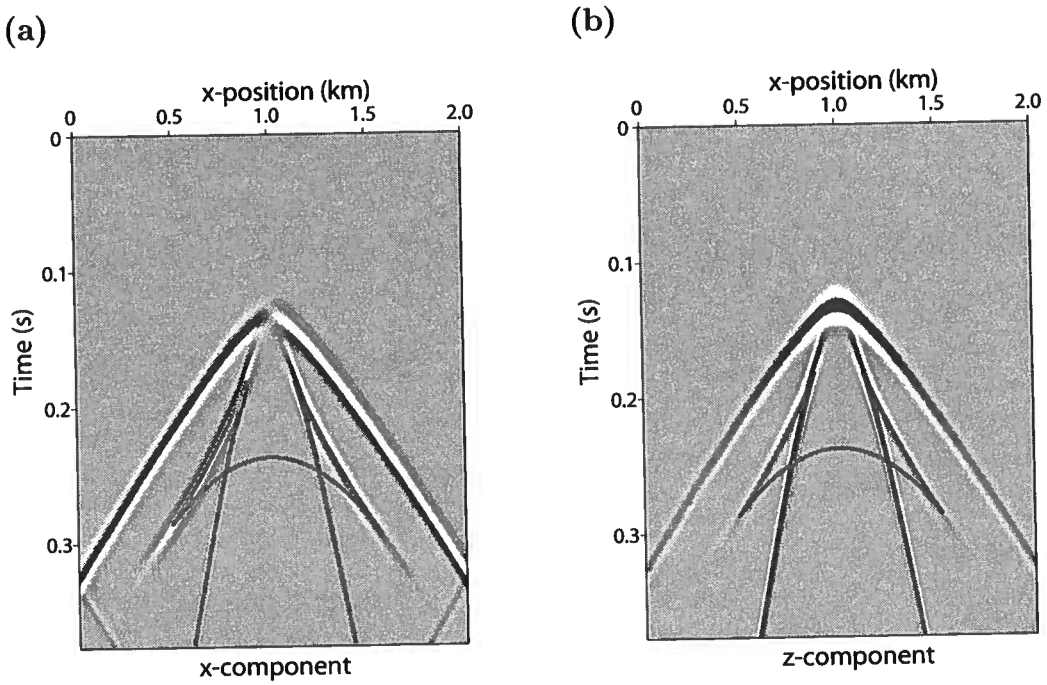

Figure 4.13: SV-wave seismograms and group-velocity surface for the model in Figure 4.10.

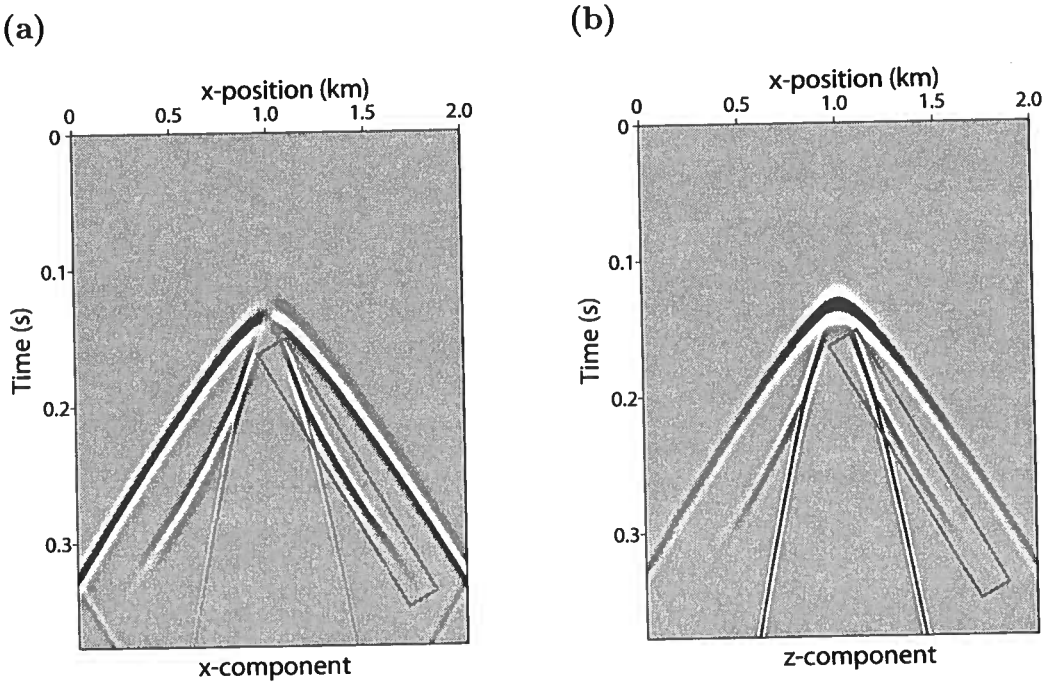

Figure 4.14: Cuspoidal branch used in the amplitude comparison in Figure 4.15.

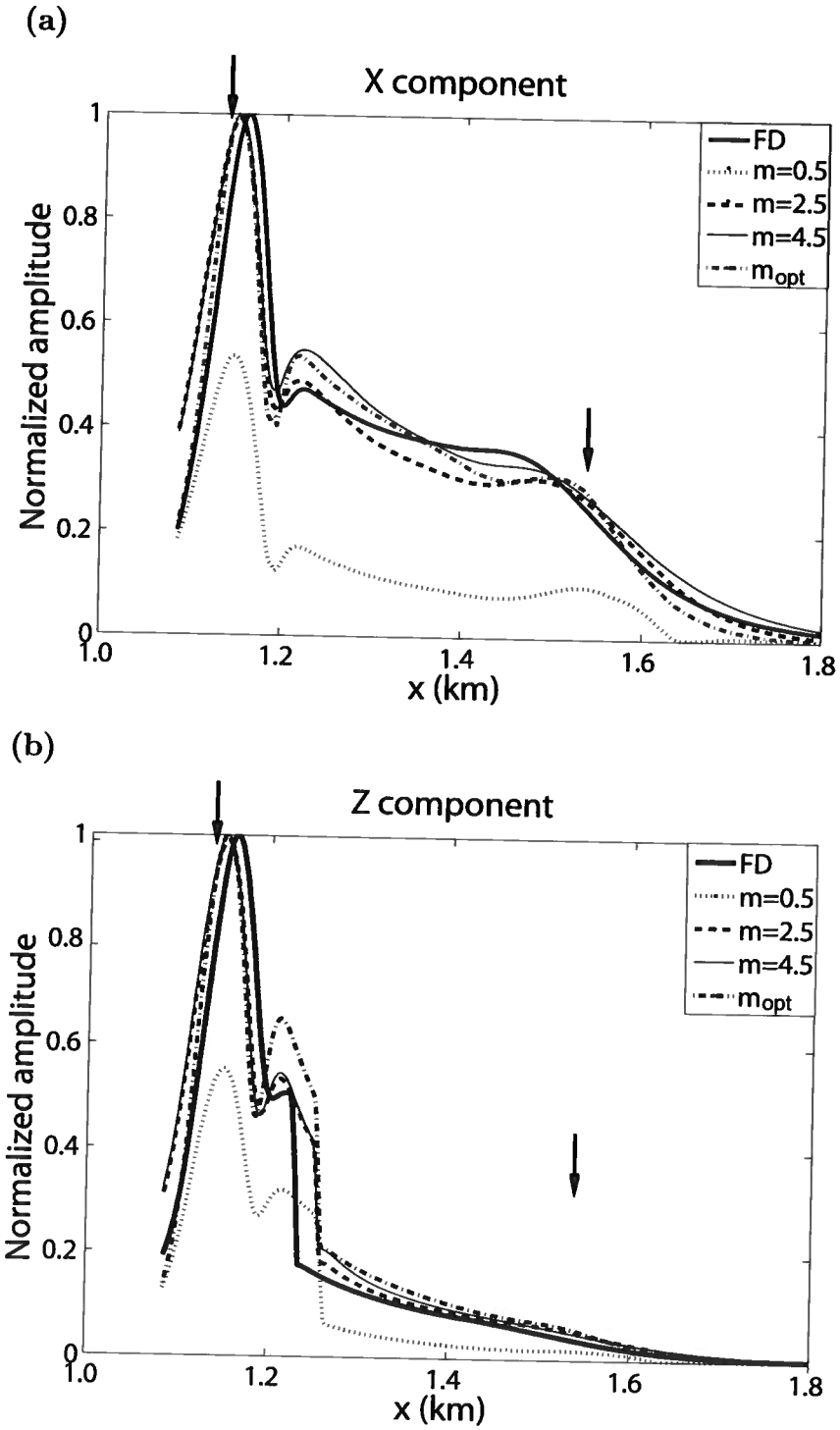

Figure 4.15: Comparison of normalized amplitudes for the (a) X- and (b) Z-components in Figure 5.4. The vertical marks indicate the locations of the edge of the cusp.

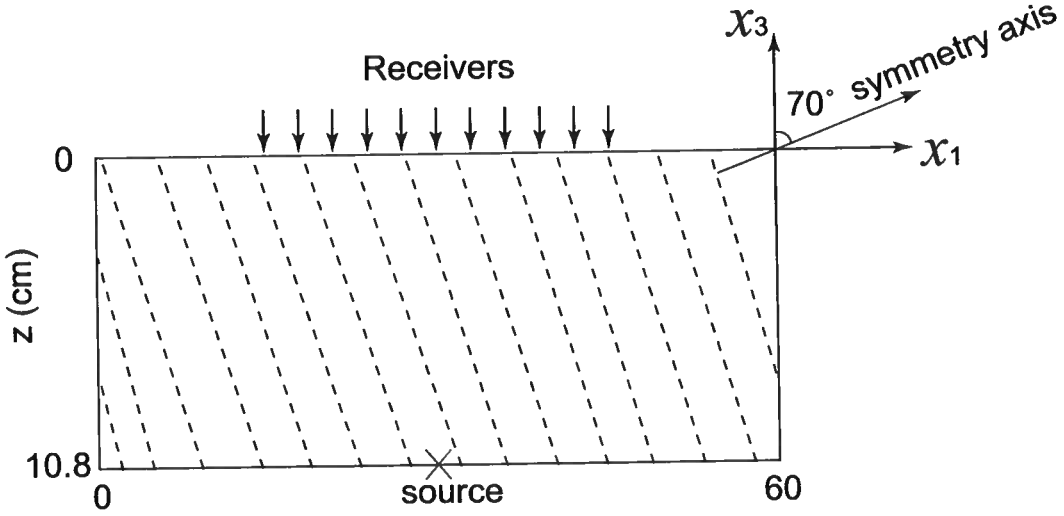

Figure 4.16: Physical model with the estimated parameters $V_{P0} = 2.6$ km/s, $V_{S0} = 1.38$ km/s, $\epsilon = 0.46$, $\delta = 0.11$, $\sigma = 1.24$, and $\nu = 70°$. The shear-wave source (a horizontal transducer) is located at the bottom of the model. The receivers are located at the surface.

wavefield excited by the shear transducer and modeled by the spectral element method (Figure 4.18). Because we do not have access to the physical modeling and spectral-element data, it is difficult to compare the amplitudes and polarization. Note that the σ value in this model is typical for shales. Although the tails of the cuspoidal wavefront calculated by GB summation are slightly longer than the ones on the the physical-modeling and spectral-element section, the shape of the cusp is well-reconstructed.

4.4 Hodograms for SV-wave Cusps

The geometrical-seismics approximation is described by the leading term of the ray series expansion, which has a linear polarization for P- and SV-waves. Hence, the ray tracing method based on geometrical seismics can only produce linear polarization for cuspoidal wavefronts. At the edges (location 1 in Figure 4.20) or the tails (location 3 in Figure 4.20) of the cusps, ray tracing cannot provide any information because the amplitude at the edge of the cusp is infinite and the ray method cannot model diffraction tails. Although GB summation is based on ray theory, diffraction expressions

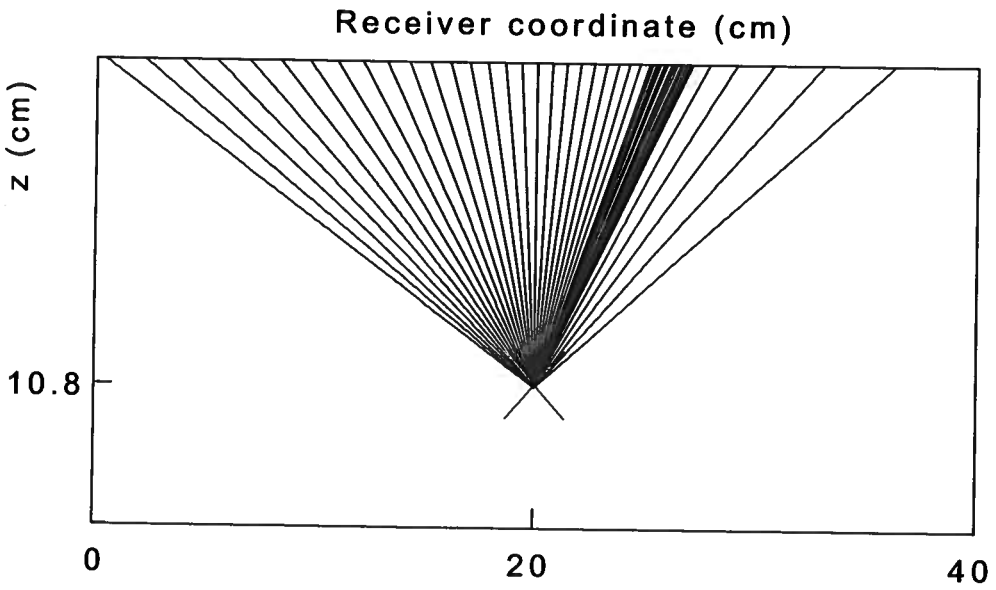

Figure 4.17: SV-wave raypaths for the model in Figure 4.16.

using complex traveltimes and summation of Gaussian beams may produce nonlinear polarization.

Generally, nonlinear polarization is caused by higher-order ray series terms, primarily by the first-order term, which is largely governed by the spatial derivatives of the leading term (Tsvankin, 2005). Therefore, the uneven amplitude distribution along the wavefront may produce nonlinear polarization in the area of the cusp (Martynov & Mikhailenko, 1984). Deviations from the geometrical seismics, which can be identified by nonlinear polarization on particle-motion diagrams, sometimes are substantial even in the far-field. Here, we only consider far-field SV-wave polarization (the source-receiver distance exceeds 10 average SV-wavelengths).

The analysis in Figures 4.21–4.26 shows that GB summation produces nonlinear polarization, but the nonlinearity is less pronounced than that generated by FD. The polarization at all three locations are close to elliptical. At the edge of the cusp (location 1), GB summation produces nonlinear polarization with less ellipticity than finite differences. At location 2 inside the cusp, the polarization diagrams generated by both methods are similar. Location 3 is at the tails of the cusp where nonlinear polarization is caused by diffraction. As is the case for location 1, the polarization computed by GB summation is more linear compared with the FD result.

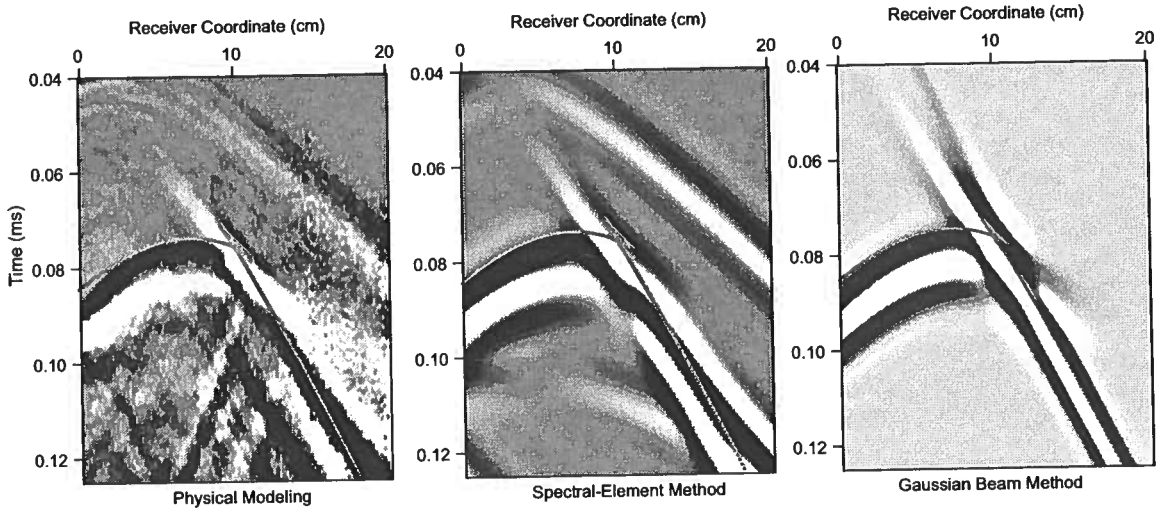

Figure 4.18: Cusps in the transmitted wavefield excited by a shear-wave source. The left section is recorded by the laser vibrometer. The middle section is simulated using the spectral-element method. The right section is calculated by GB summation for a central frequency of 0.6 Hz with the optimized beam width M_{opt}. The solid line is the direct shear-wave traveltime computed from the SV-wave group-velocity surface.

The initial beam width also influences the polarization diagrams. The degree of nonlinearity varies with the initial beam widths and flattens out for $m > 2.0 \sim 4.0$ (Figures 4.22, 4.24, and 4.26). All the hodograms are plotted in the same scale. The dependence of the polarization on m is similar to that for the amplitude and confirms that the optimal range for the beam width is $2.0 < m < 8.0$.

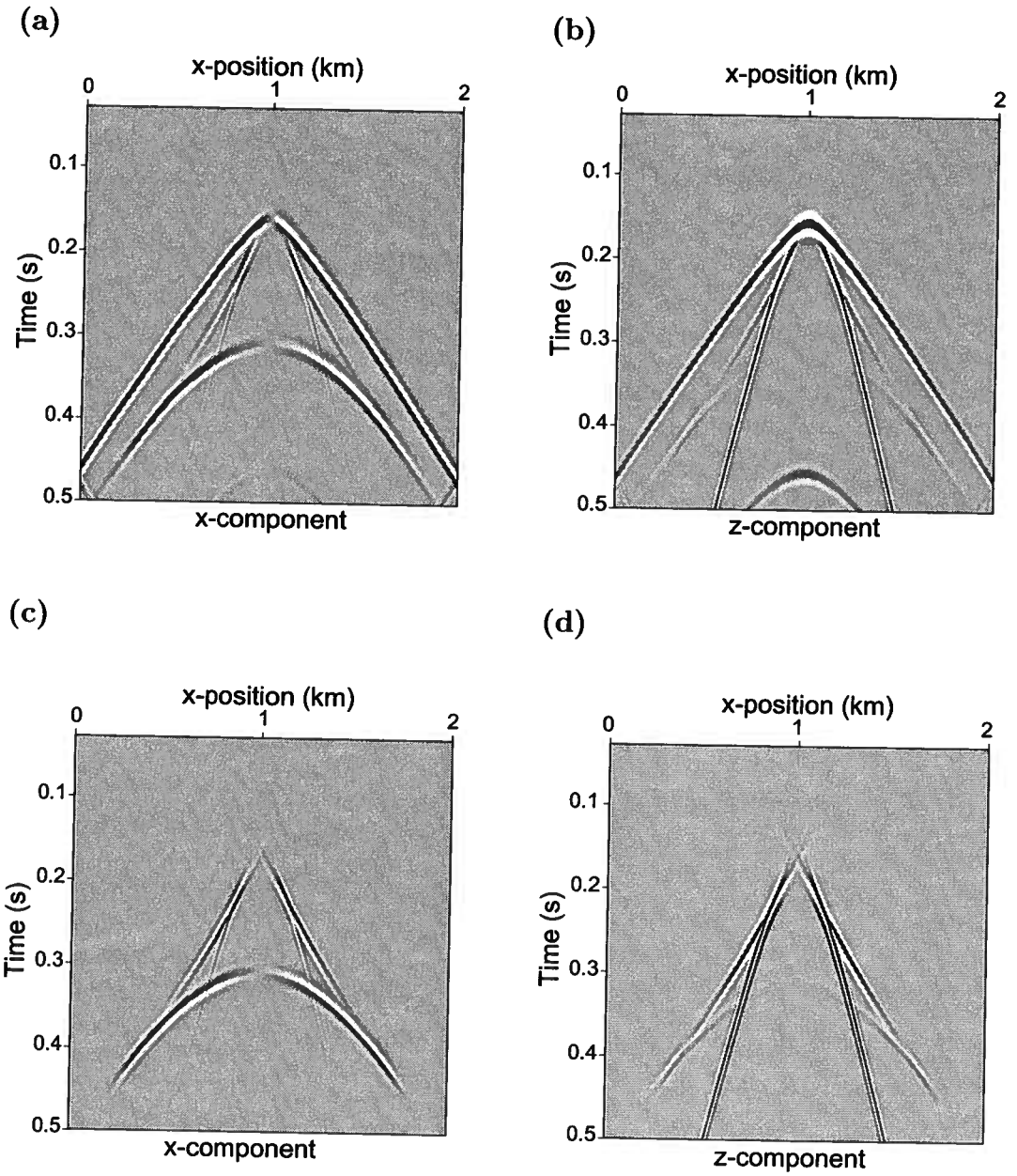

Figure 4.19: Seismograms for a homogeneous VTI model with $V_{P0} = 2.0$ km/s, $V_{S0} = 1.0$ km/s, $\epsilon = 0.3$, $\delta = -0.3$, and $\sigma = 2.4$. (a) and (b) are the X- and Z-component seismograms obtained by the finite difference method. (c) and (d) are computed by the GB method with m_{opt}.

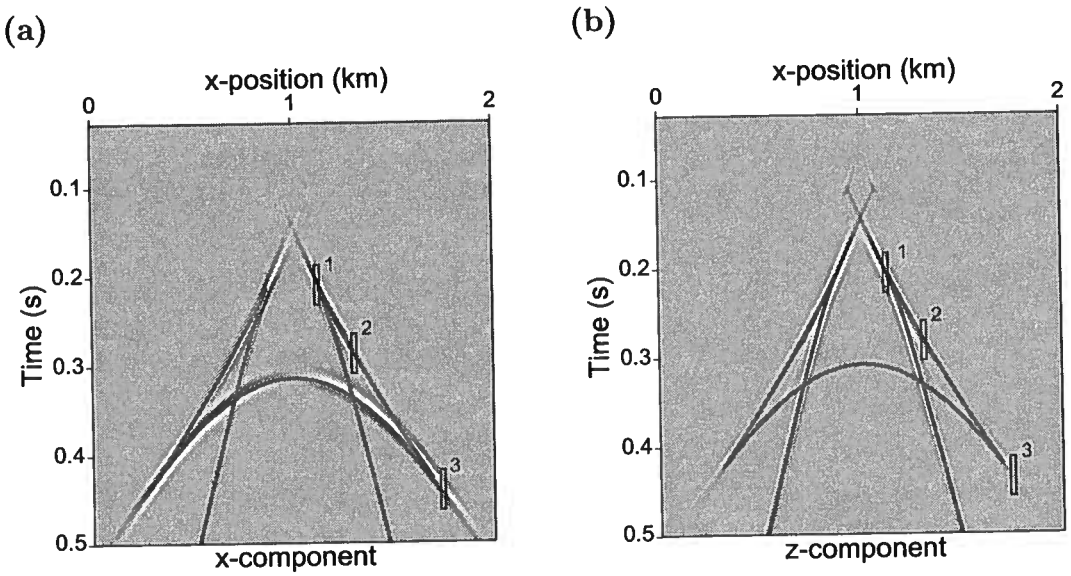

Figure 4.20: Seismograms for the model from Figure 4.19 with the overlaid direct SV-wave traveltime (solid lines) computed from the group-velocity surface. The hodograms in Figures 4.21, 4.23, and 4.25 are computed at locations 1, 2, and 3.

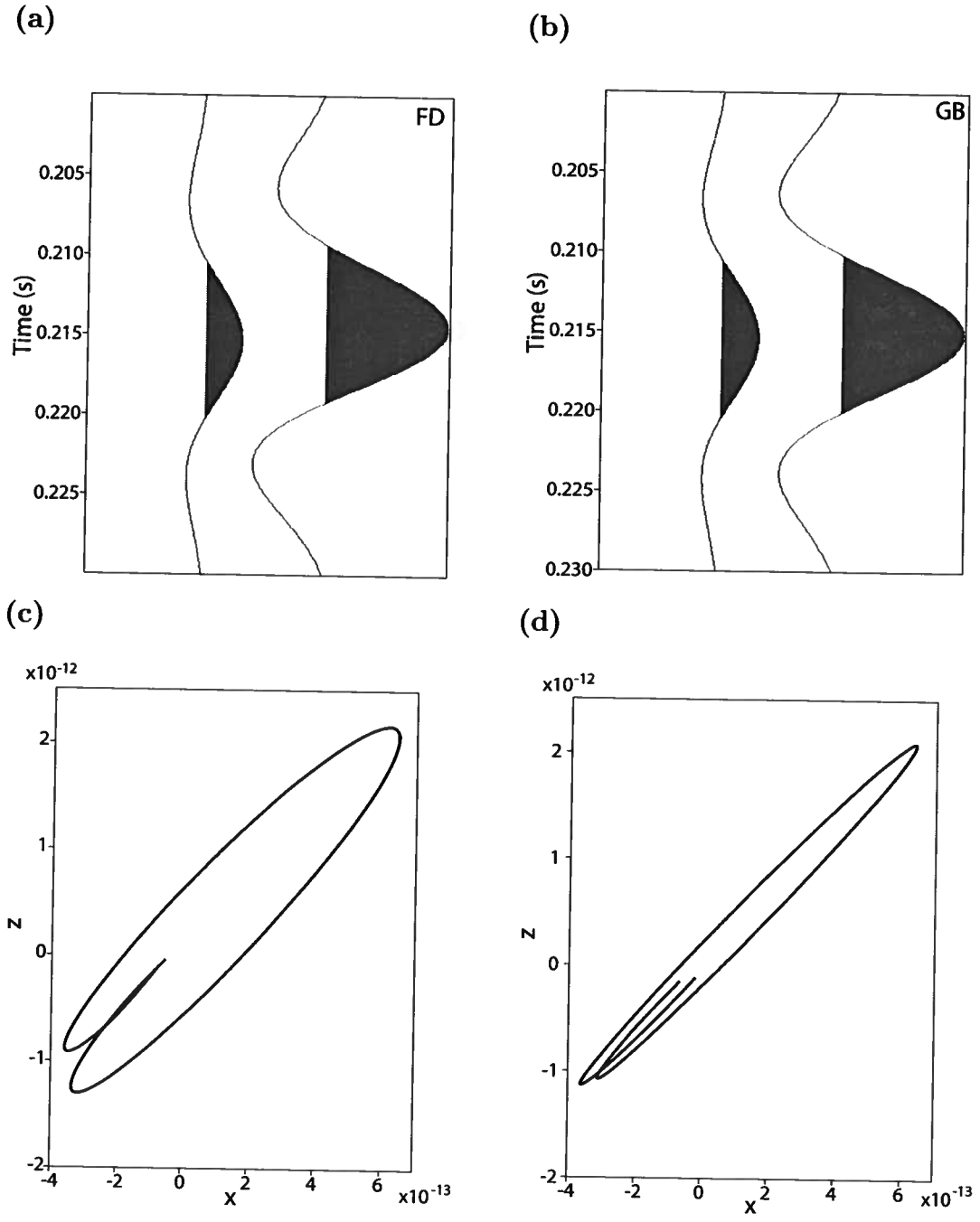

Figure 4.21: Seismic traces and hodograms at location 1 in Figure 4.20. (a) and (b) are the X- and Z-component traces obtained by the finite difference method and GB summation, respectively. (c) and (d) are the corresponding hodograms.

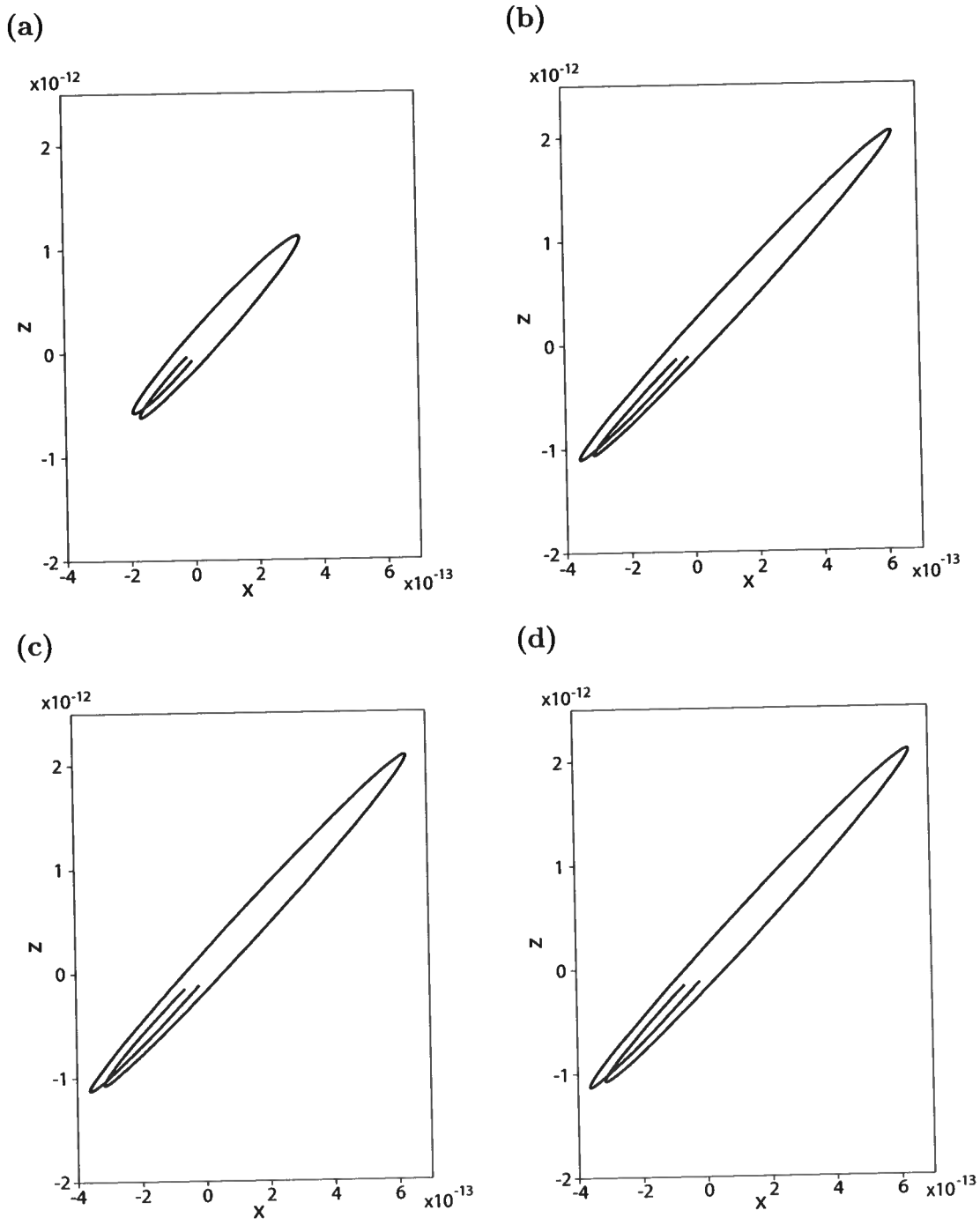

Figure 4.22: Hodograms at location 1 in Figure 4.20 for different values of m (i.e., different initial beam width). (a) $m = 0.5$; (b) $m = 2.5$; (c) $m = 4.5$; and (d) $m = 6.5$.

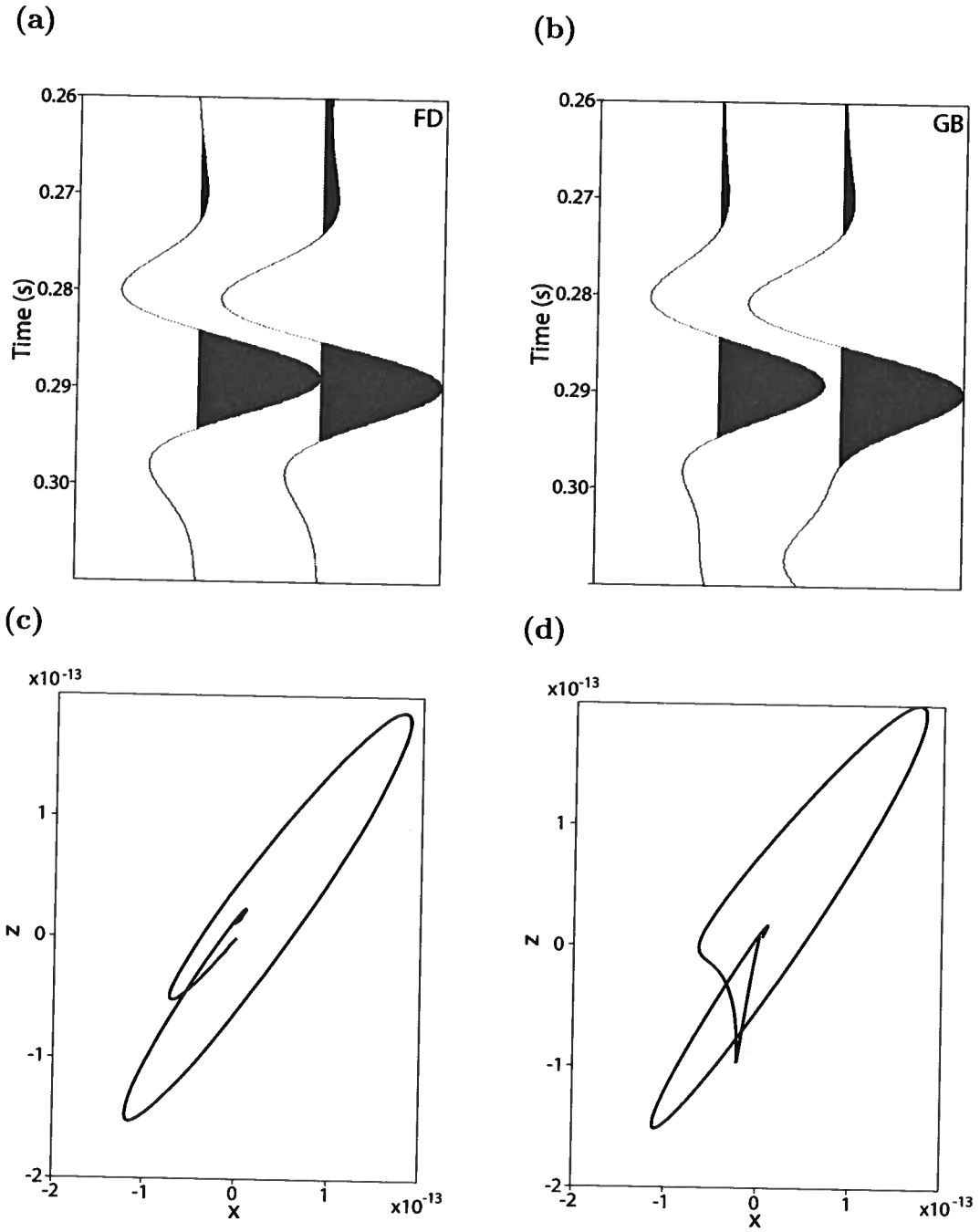

Figure 4.23: Seismic traces and hodograms at location 2 in Figure 4.20. (a) and (b) are the X- and Z-component traces obtained by the finite difference method and the GB summation, respectively. (c) and (d) are corresponding hodograms.

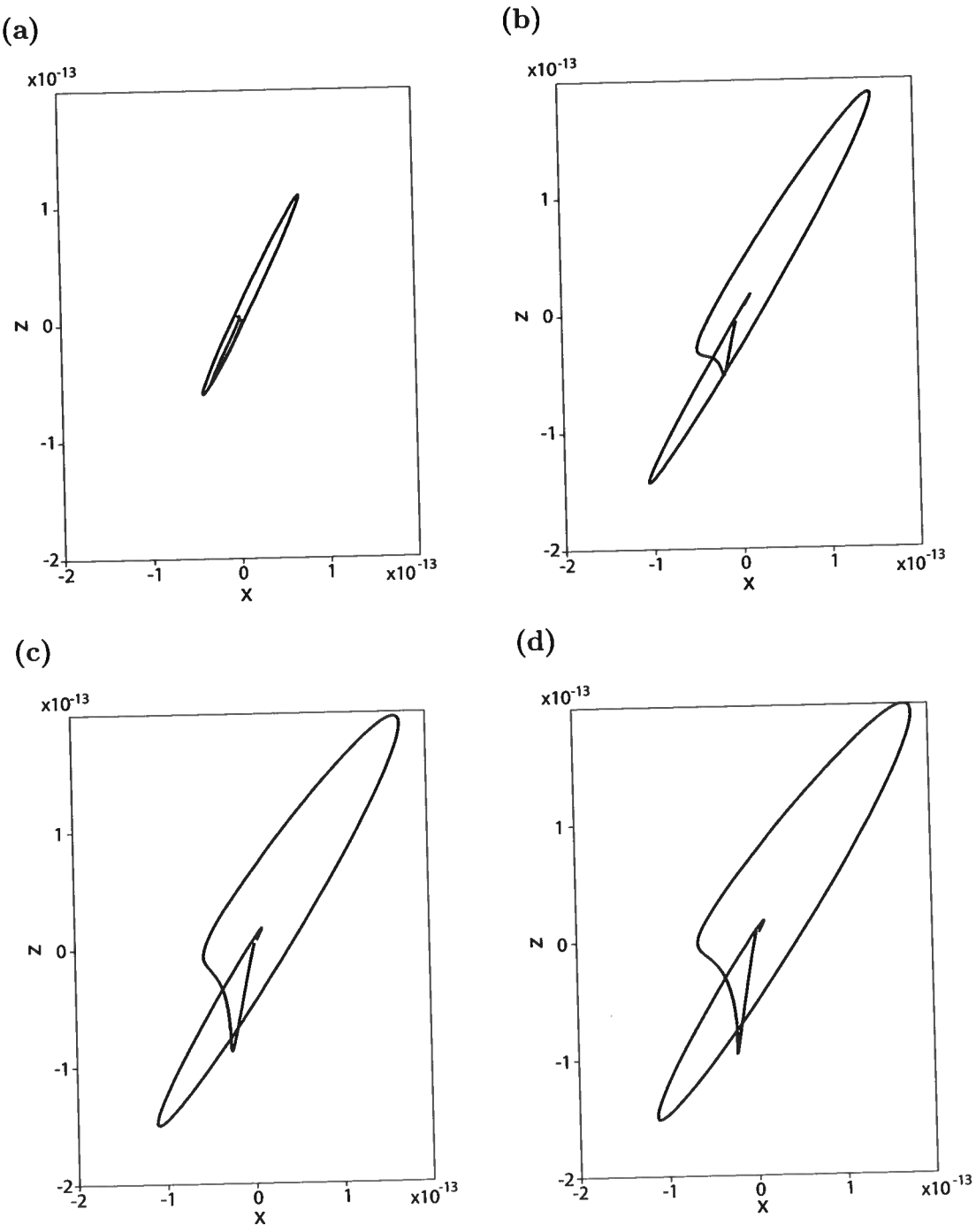

Figure 4.24: Hodograms at location 2 in Figure 4.20 for different values of m. (a) $m = 0.6$; (b) $m = 2.5$; (c) $m = 4.5$; and (d) $m = 6.5$.

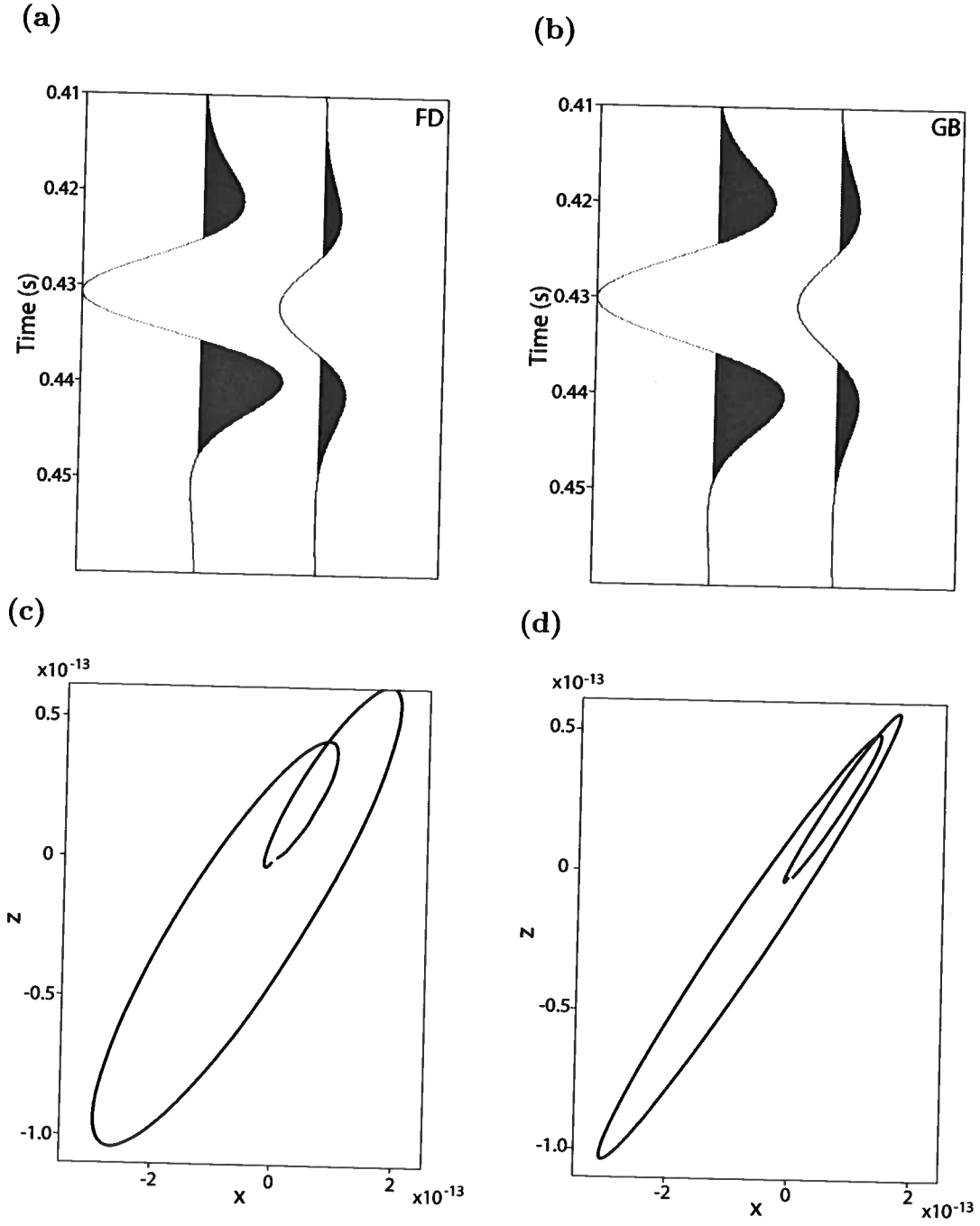

Figure 4.25: Seismic traces and hodograms at location 3 in Figure 4.20. (a) and (b) are the X- and Z-component traces obtained by the finite difference method and the GB summation, respectively. (c) and (d) are corresponding hodograms.

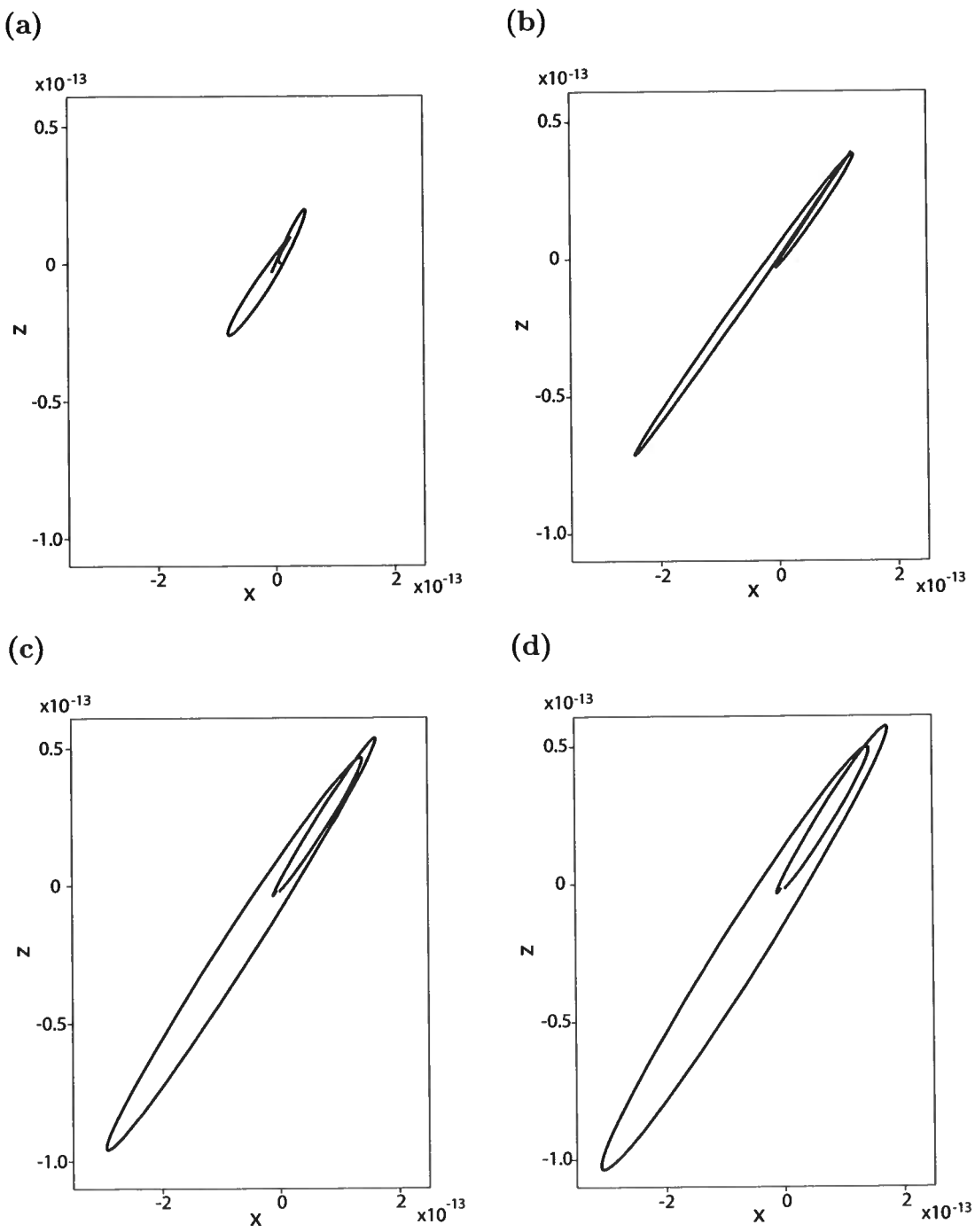

Figure 4.26: Hodograms at location 3 in Figure 4.20 for different values of m. (a) $m = 0.5$; (b) $m = 2.5$; (c) $m = 4.5$; and (d) $m = 6.5$.

Chapter 5

Tests for heterogeneous media

5.1 Summary

The previous chapter describes SV-wave cusps in homogeneous TI media. The theory outlined in Chapter 3, however, is valid for heterogeneous anisotropic media as well. Here, GB modeling is applied to a more complicated layered VTI model. The seismograms contain anisotropy-induced cusps in reflection SV-wave data.

5.2 Layered Model

A four-layer VTI model is used with the parameters given in Table 5.1. The magnitude of the anisotropy parameters ϵ and δ does not exceed 0.3. Reflected shear waves from all three interfaces are computed by the FD and GB methods in Figures 5.1-5.3. Although the seismograms are normalized, the GB summation method reproduces the cusps with amplitudes that are similar to the FD results. Because the reflected SV-wave cusps are observed at long offsets (more than twice the reflector depth), the FD computation time is extremely high(the GB method is about 500 faster). Still, the FD results in Figure 5.1 contain considerable numerical noise, which complicates picking of amplitudes and polarizations.

The results of GB summation for three reflected SV-wave cusps confirm the conclusions drawn for homogeneous media. Here, we examine the SV-wave cusps reflection from the second interface. The beam width influences the shape and amplitudes of the cuspoidal wavefront. When m is small ($m = 0.5$ in Figure 5.2), the beam widths at the receivers become large and introduce artificially long tails for SV-wave cusps. The amplitudes are much smaller than those for larger values of m (Figure 5.5). With increasing m, the seismograms become close to the FD results and

Parameters	Depth	V_{P0}	V_{S0}	ρ	ϵ	δ	σ
Layer 1	1.48	5.370	2.2	2.774	0.264	0.016	1.477
Layer 2	1.98	4.336	1.8	2.567	0.247	0.010	1.375
Layer 3	2.28	3.882	1.6	2.247	0.230	0.011	1.289
Layer 4	5.00	3.600	1.5	2.242	0.0	0.0	0.0

Table 5.1: Parameters of a four-layer VTI model. For all models, the vertical velocities (V_{P0} and V_{S0}) are in km/s, depth is in km, and density (ρ) is in gm/cm^3. A line source is located at the surface.

the amplitudes converge to a certain value. However, when the initial beam width is large ($m = 10.0$), the wide beam widths cause artifacts (Figure 5.3). If the m value is within the range ($2.0 < m < 8.0$) suggested in Chapter 4, the GB summation seismograms are close to the FD results (Figures 5.1-5.3). Due to such factors as the geometrical spreading, source spectrum, polarization and reflection/transmission coefficients, the highest amplitude is not necessarily observed at the edges of the cusps (Figure 5.5).

As discussed above, the polarization for cuspoidal wavefronts is nonlinear. Because it is difficult to record the polarization at location 2 (as in Figure 5.6), the other two locations (1, 3) are chosen (Figure 5.6). Figures 5.7 and 5.8 show the polarization at the edge of cusps which are almost linear as in the homogeneous media (Figure 4.21). The polarizations at the tails of the cusps are elliptical due to the diffraction (Figures 5.9 and 5.10).

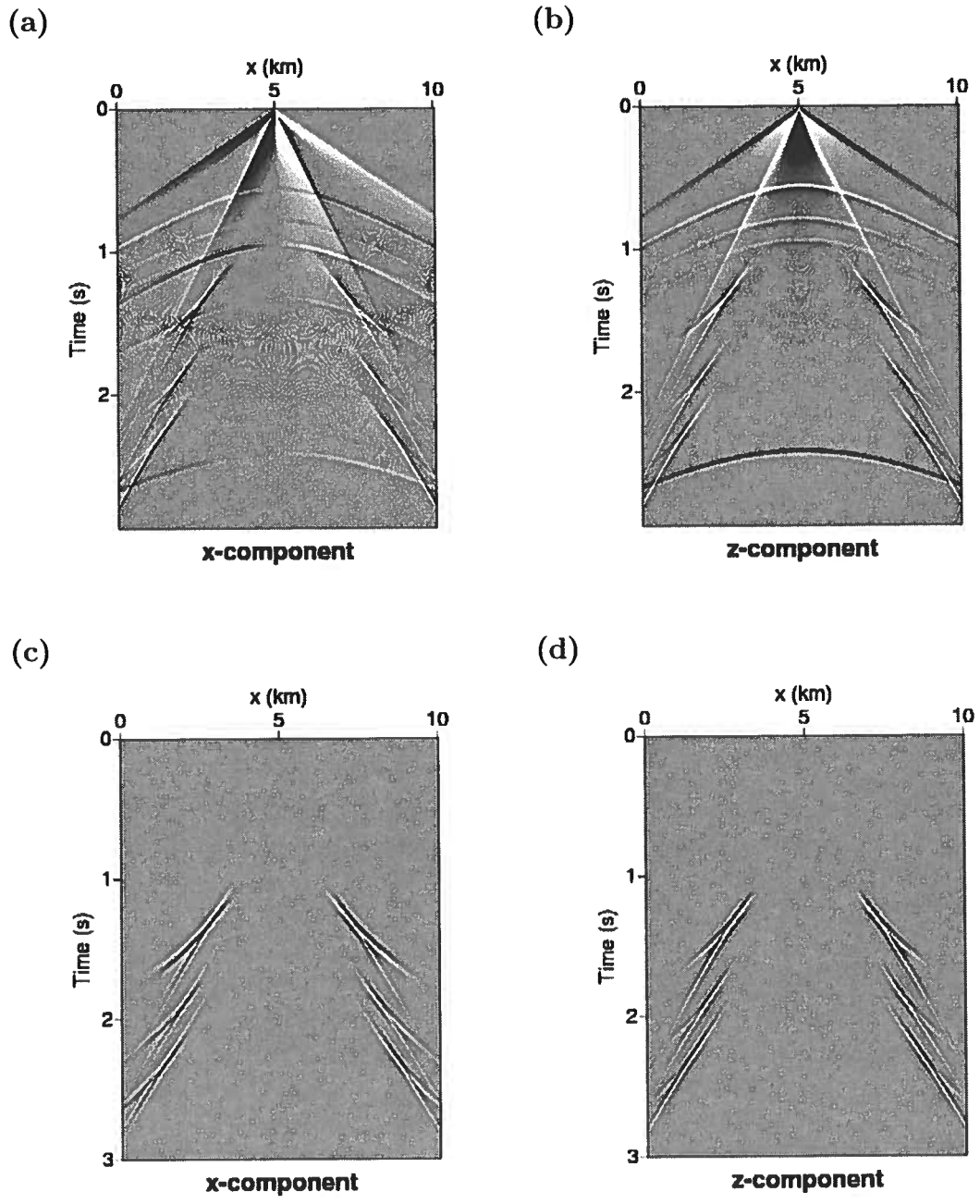

Figure 5.1: Seismograms for the four-layer VTI model from Table 5.1. Figures (a) and (b) are the seismograms from the FD method. Figures (c) and (d) are from the GB summation method with m_{opt}.

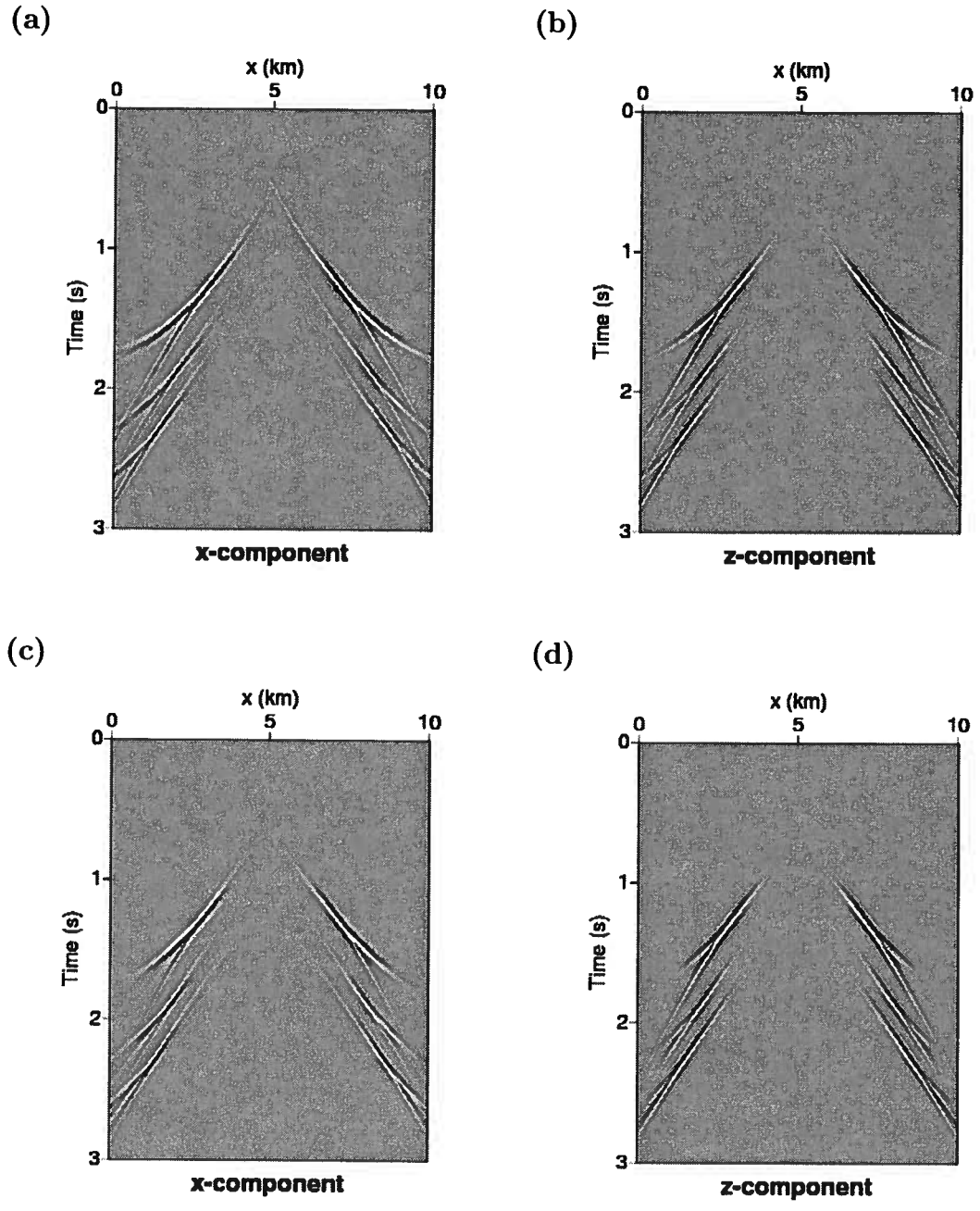

Figure 5.2: Wavefields generated by GB modeling for the same model as in Figure 5.1. Figures (a) and (b) are the X- and Z-component seismograms for $m = 0.5$. Figures (c) and (d) are for $m = 2.5$.

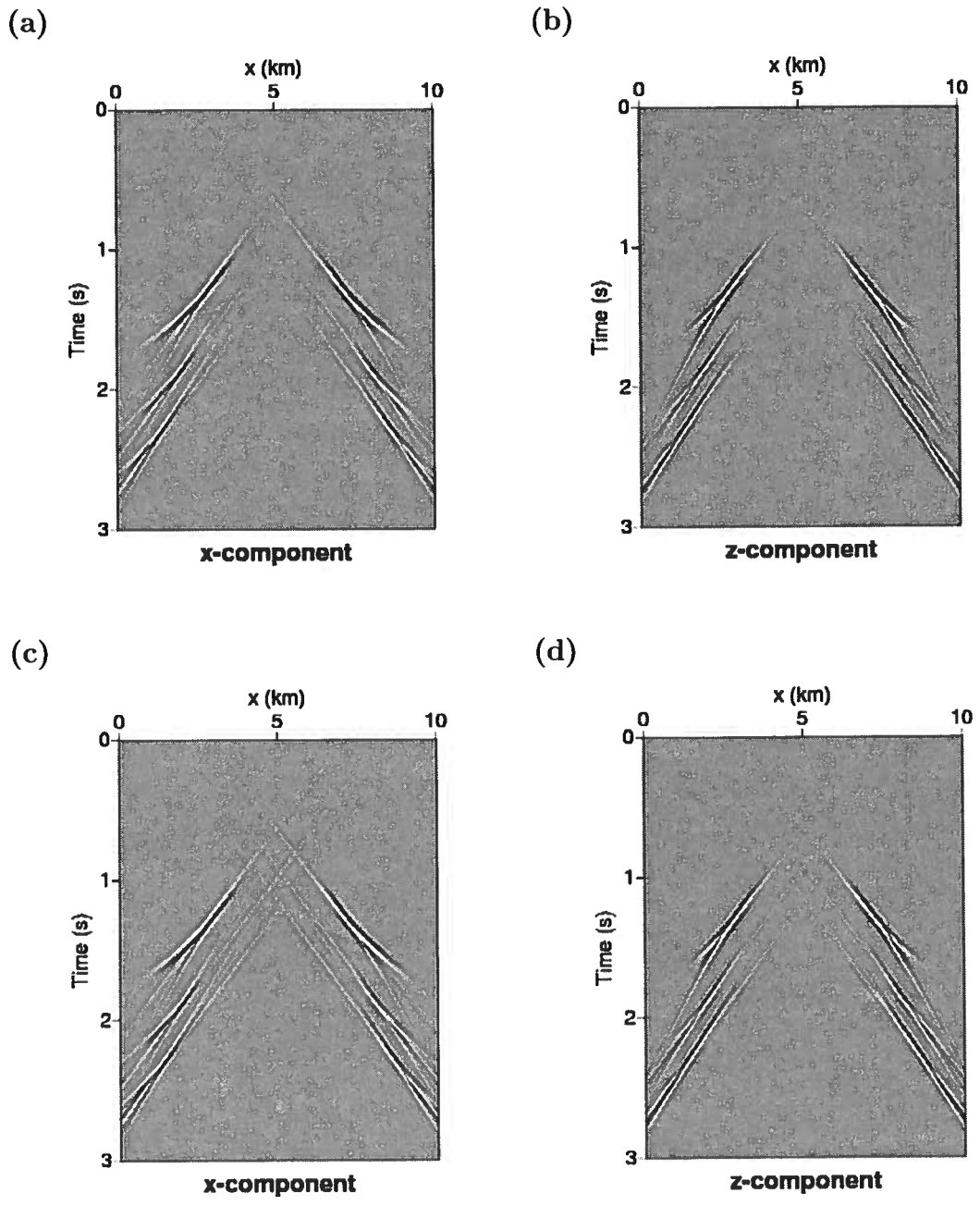

Figure 5.3: Same as Figure 5.2. Figures (a) and (b) are the X- and Z-component seismograms for $m = 4.0$. Figures (c) and (d) are for $m = 10.0$.

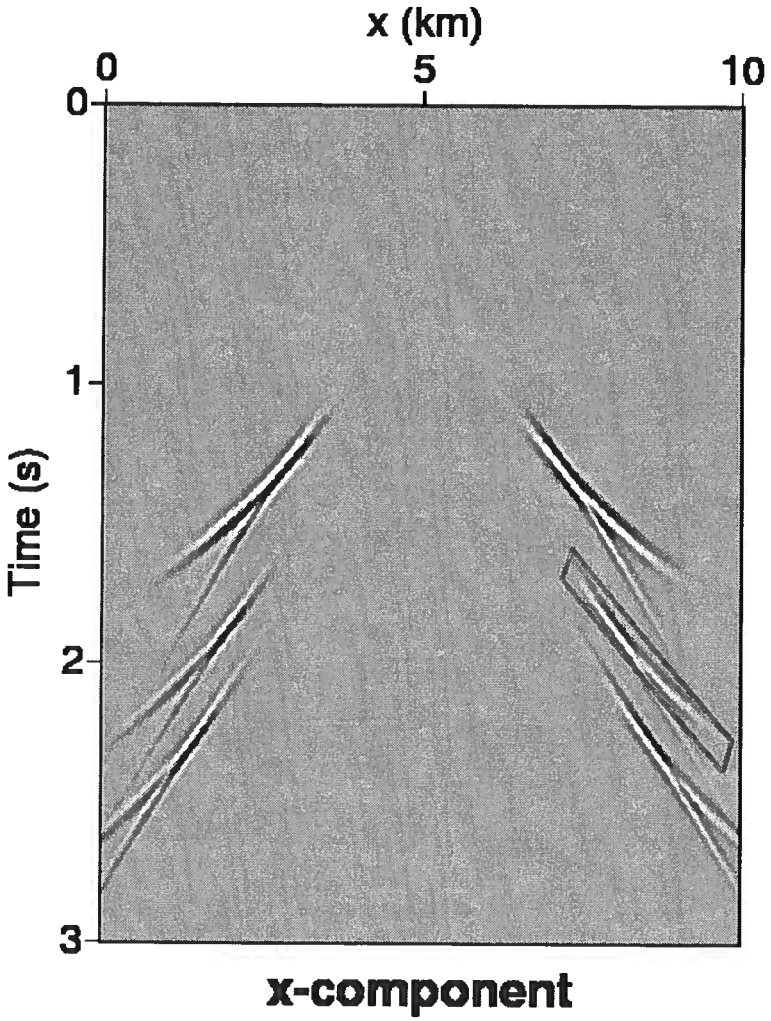

Figure 5.4: Cuspoidal branch marked area used in the amplitude comparison in Figure 5.5.

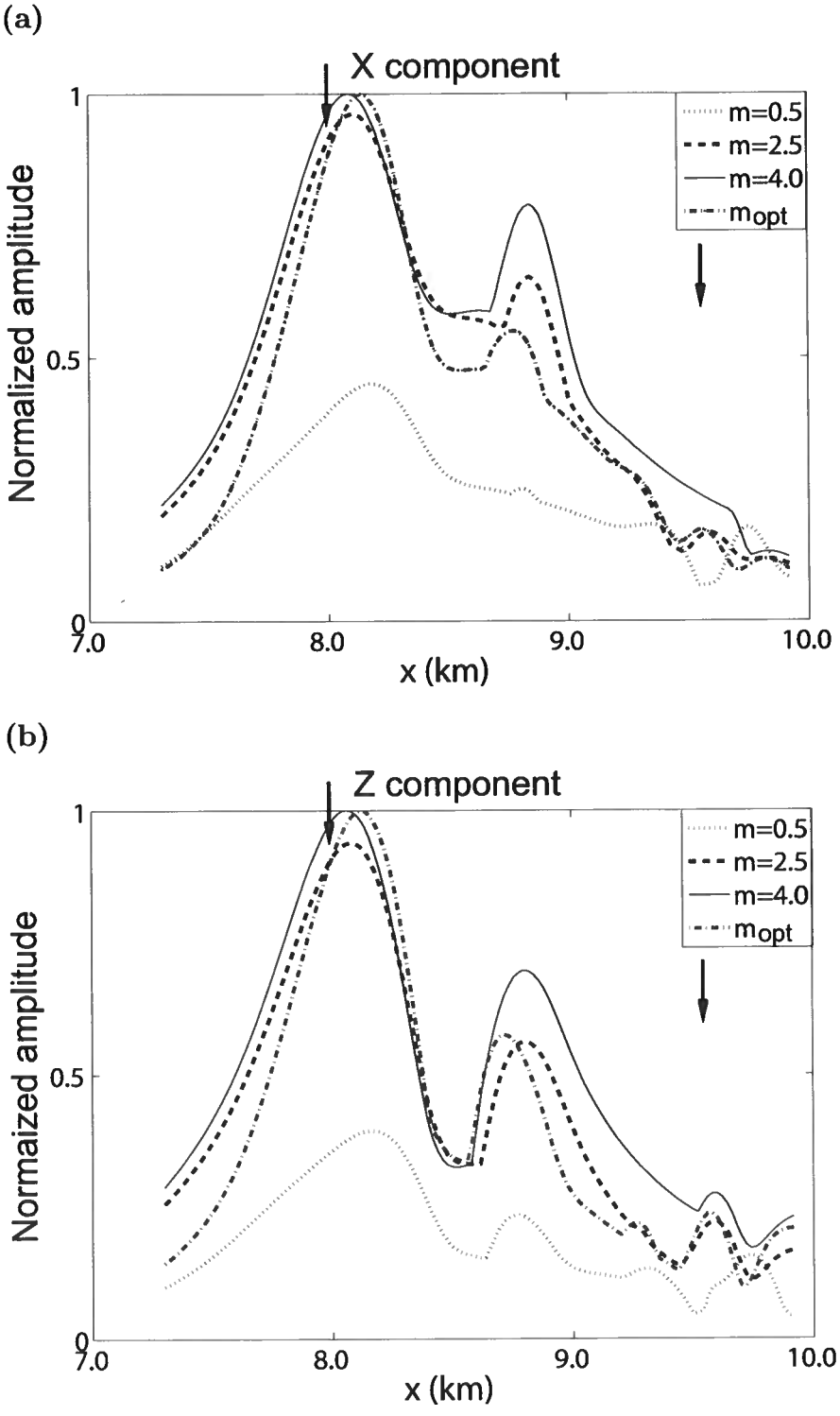

Figure 5.5: Amplitudes for the cuspoidal branch in Figure 5.4. Figures (a) and (b) are the relative amplitudes of the X- and Z-component from the GB summation method. The vertical marks indicate the locations of the edges of the cusp.

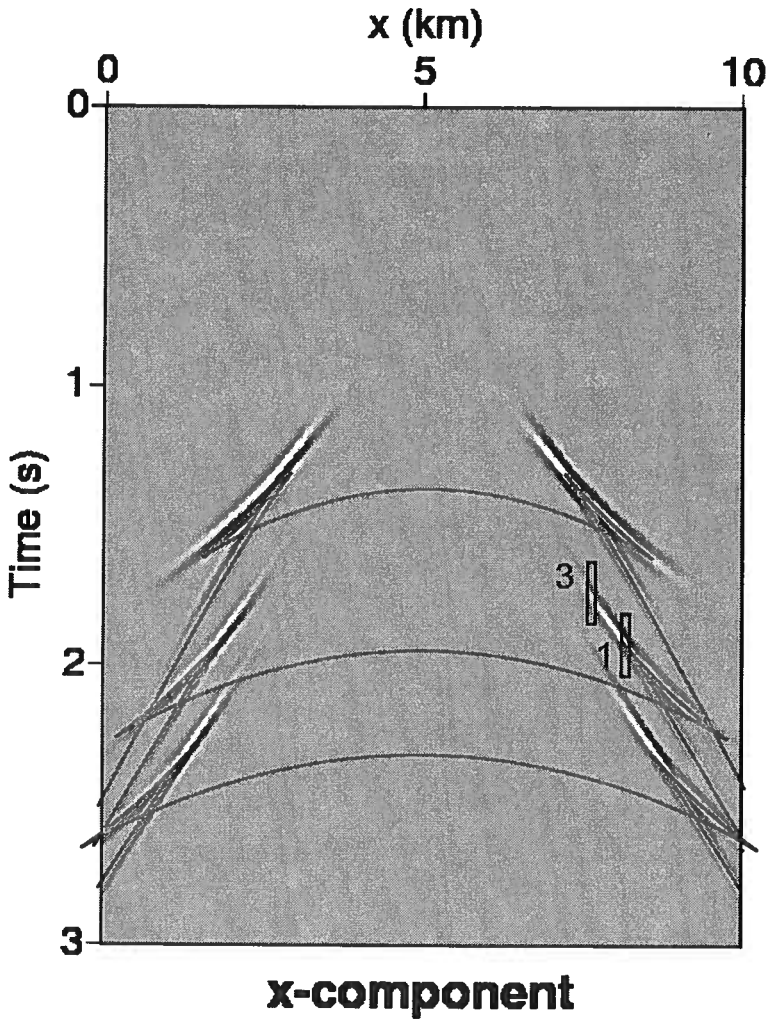

Figure 5.6: Seismograms for the model from Table 5.1 with the overlaid SV-wave traveltime (solid lines) computed from the group-velocity surface. The hodograms in Figures 5.7 - 5.10 are computed at locations 1 and 3.

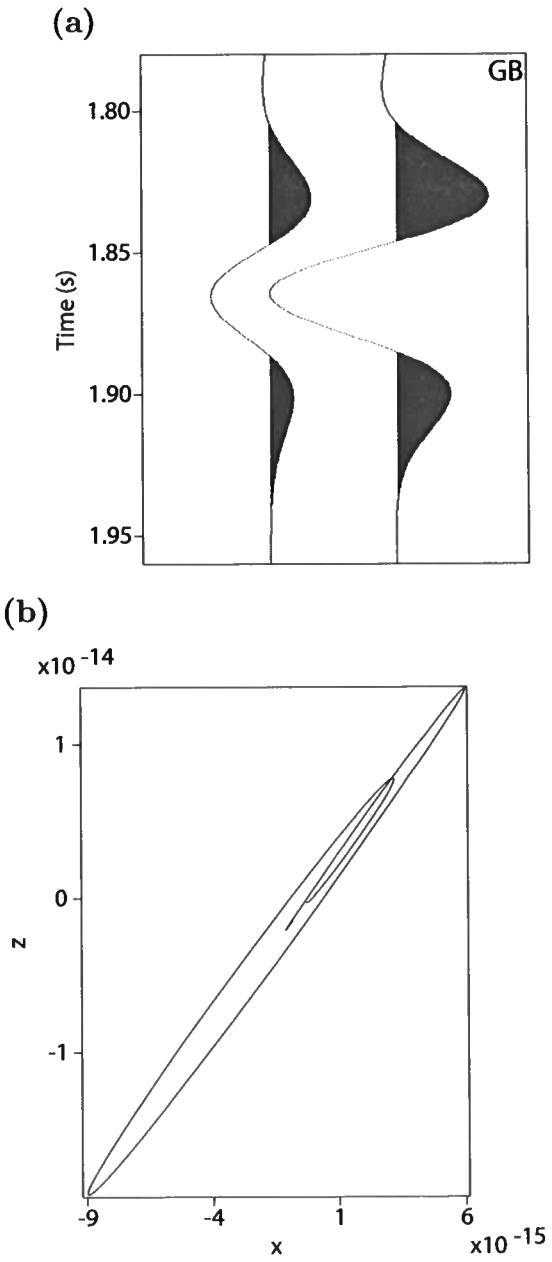

Figure 5.7: Seismic traces and hodograms at location 1 in Figure 5.6 obtained by the GB summation for $m = 4.0$. (a) is the X- and Z-component traces obtained by GB summation. (b) is the corresponding hodogram.

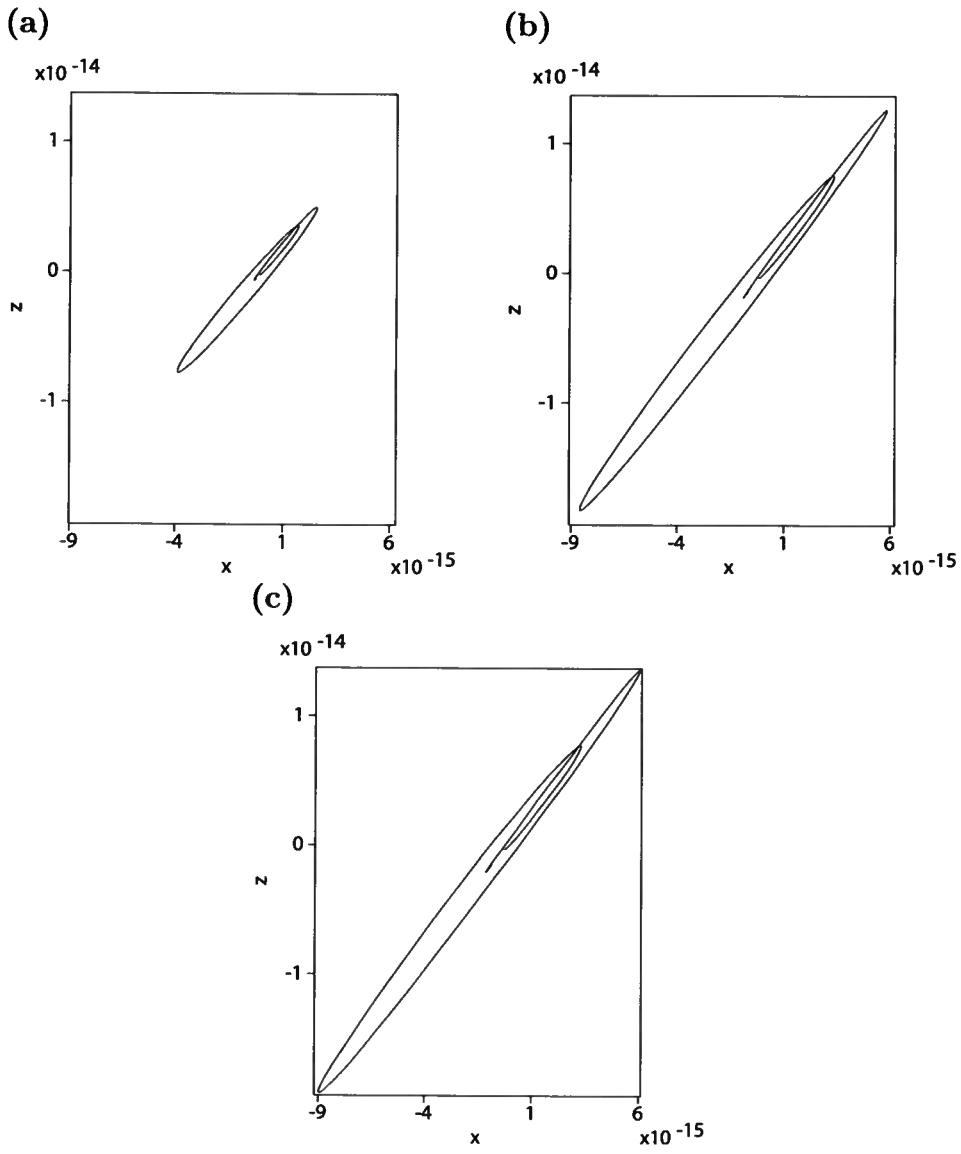

Figure 5.8: Hodograms at location 1 in Figure 5.6 for different values of m. (a) $m = 0.5$; (b) $m = 2.5$; (c) $m = 4.0$.

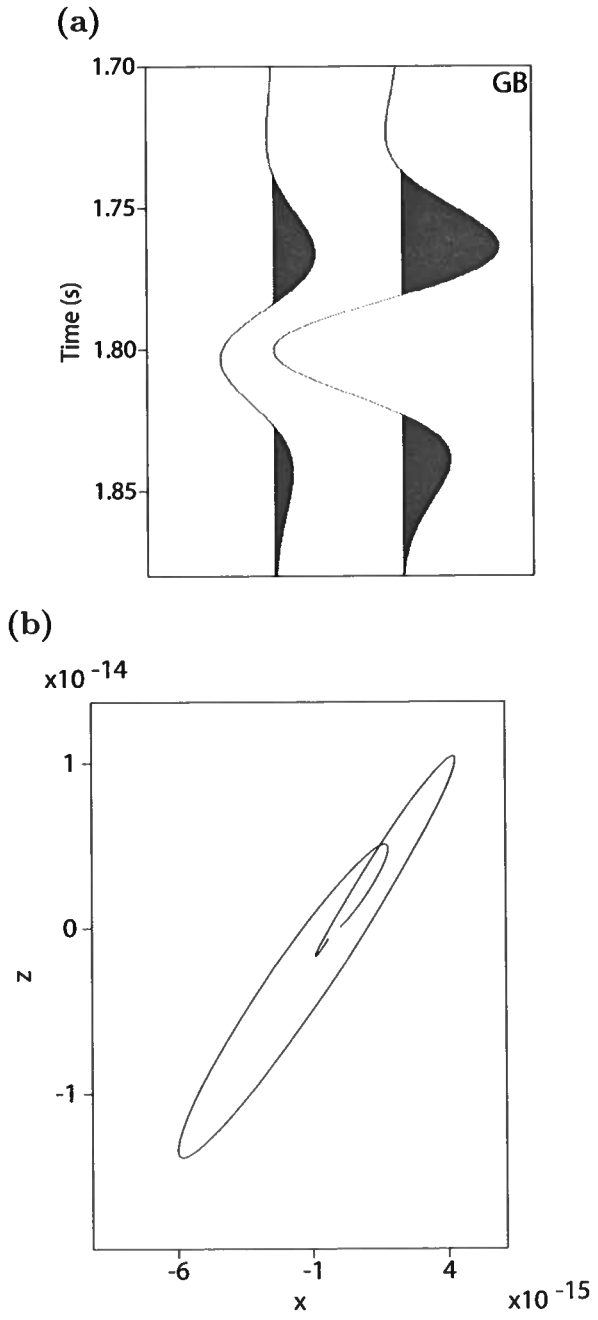

Figure 5.9: Seismic traces and hodograms at location 3 in Figure 5.6 obtained by the GB summation for $m = 4.0$. (a) is the X- and Z-component traces. (b) is the corresponding hodogram.

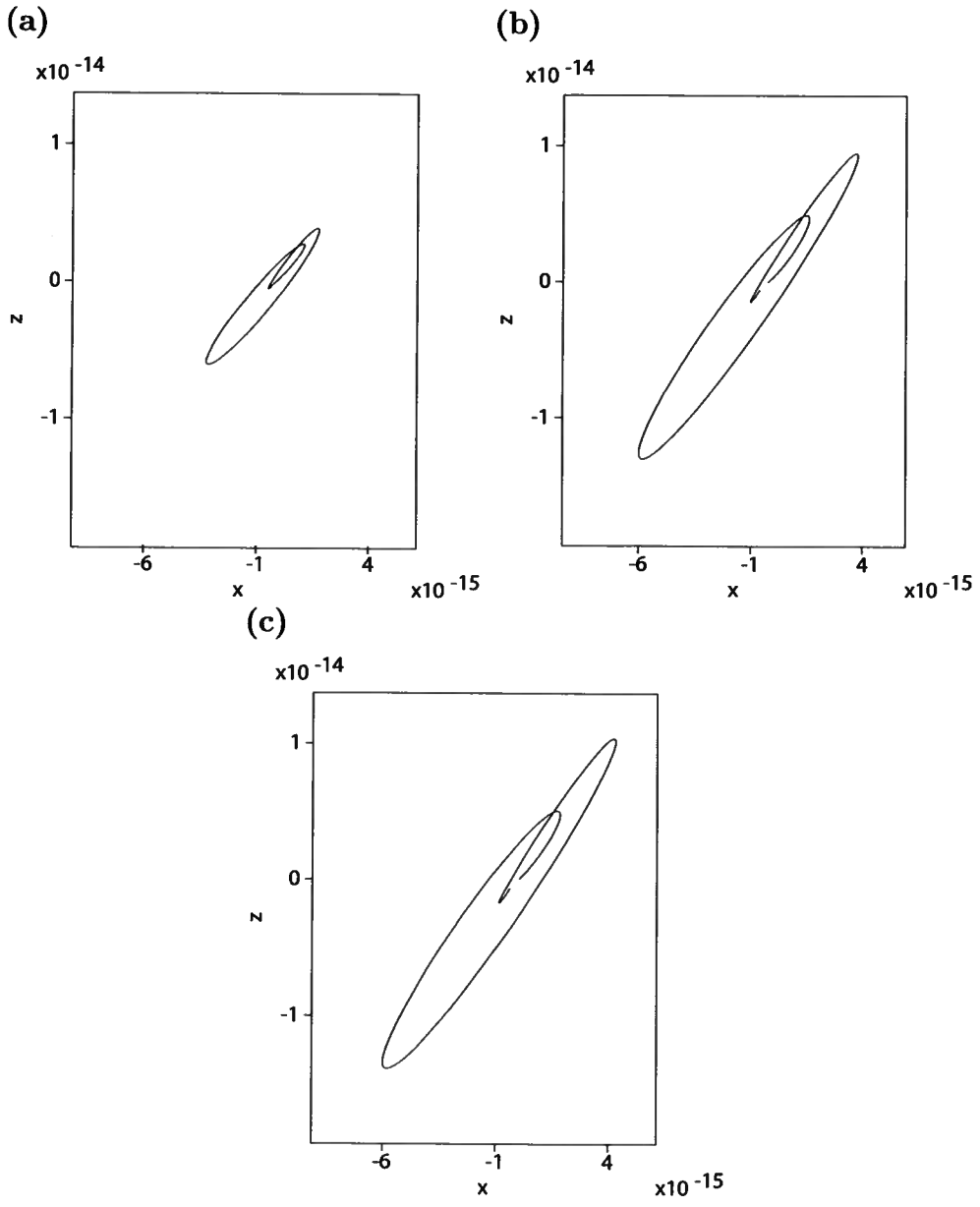

Figure 5.10: Hodograms at location 3 in Figure 5.6 for different values of m. (a) $m = 0.5$; (b) $m = 2.5$; (c) $m = 4.0$.

Chapter 6

Conclusions and future work

This thesis was devoted to application of the GB summation method to modeling SV-wave cusps in TI media. As an extension of ray theory, GB summation with the optimized beam parameters produces more accurate description of the amplitudes and polarization along cuspoidal wavefronts in homogeneous and layered TI models.

The beam weighting factor is derived using the asymptotic GB expression and the far-field Green's function in TI media. To obtain an accurate approximation for the wavefield, it is critically important to choose the optimal beam parameters, such as the angle range, beam interval, and the initial beam width. In particular, the optimal range of the initial beam width is found to be $2.0 < m < 8.0$. With the proper parameters, the GB summation method provides a close approximation to finite-difference (FD) results for both P- and SV-waves even in strongly anisotropic media. The diffraction expressions used to form Gaussian beams help model the nonlinear polarization along the cusp.

Testing was performed for a range of TI models with different types of SV-wave cusps. The maximum GB amplitudes are shifted slightly away from the edge of the cusp because the amplitudes are influenced by the combination of the geometrical spreading, source directivity, polarization and the reflection/transmission coefficients. On the whole, the amplitudes computed by the GB method deviate only by about 10% from the FD values.

The polarizations for cuspoidal wavefronts are nonlinear because the wavefield cannot be described by the geometrical-seismics approximation. Based on the tests for different spatial locations along the cusp, we found that GB summation produced nonlinear polarization, but the nonlinearity was not as pronounced as that computed by FD. Similar to the amplitudes, the polarization varies with the initial beam width. For $m > 2$, the polarization is weakly dependent on m and is relatively close to the

FD results.

Improper choice of the beam parameters leads to artifacts on seismograms. When the value of m is outside the optimal range, the beams at the receivers are too wide to generate clean seismograms.

In the future, the GB method discussed in this thesis can be applied to 3D anisotropic media of lower symmetry (e.g., orthorhombic). In particular, it would be instructive to compute GB wavefields in the vicinity of shear-wave point singularities.

References

Alkhalifah, T. 1995. Gaussian beam depth migration for anisotropic media. *Geophysics*, **60**(5), 1474–1484.

Babich, V. M., & Popov, M. M. 1990. Gaussian summation method (review). 1063–1081.

Bleistein, N. 2009. *Mathematics of Modeling, migration and inversion with Gaussian beams.* USA: http://www.cwp.mines.edu/ norm/ShrtCrse/.

Červený, V. 1972. Seismic rays and ray intensities in Inhomogeneous Anisotropic Media. *Geophys. J. R. astr. Soc.*, **29**, 1–13.

Červený, V. 1982. Expansion of a plane wave into Gaussian beams. *Studia geoph. et geod.*, **26**, 120–131.

Červený, V. 1983. Synthetic body wave seismograms for laterally varying layered structures by the Gaussian beam method. *Geophys. J. R. astr. Soc.*, **73**, 389–426.

Červený, V. 1985. Gaussian beam synthetic seismograms. *Journal of Geophysics*, **58**, 44–72.

Červený, V. 2001. *Seismic ray theory.* Cambridge University Press.

Červený, V., Klimes, L., & Pšenčík, I. 1984. Paraxial ray approximations in the computation of seismic wavefields in inhomogeneous media. *Geophys. J. R. astr. Soc.*, **79**, 89–104.

Červený, V., Klimes, L., & Pšenčík, I. 2007. Seismic ray method: recent developments. *Advances in Geophysics*, **48**, 1–126.

Červený, V., & Moser, T. 2007. Ray propagator matrices in 3D anisotropic inhomogeneous layered media. *Geophysical Journal International*, **168**, 593–604.

Červený, V., & Pšenčík, I. 1983. Gaussian beams and Paraxial Ray Approximation in Three-Dimensional Elastic Inhomogeneous Media. *Journal of Geophysics*, **53**, 1–15.

Červený, V., & Pšenčík, I. 2009. Gaussian beams in inhomogeneous anisotropic layered structures. *Geophysical Journal International*, 1–15.

Červený, V., Popov, M. M., & Pšenčík, I. 1982. Computation of wave fields in inhomogeneous media-Gaussian beam approach. *Geophys. J. R. astr. Soc.*, **70**, 109–128.

Dellinger, Joe A. 1991. *Anisotropic seismic wave propagation.* Ph.D. thesis, Stanford University.

Dewangan, P., Tsvankin, I., Batzle, M., van Wijk, K., & Haney, M. 2006. PS-wave moveout inversion for tilted TI media: A physical-modeling study. *Geophysics*, **71**(4), D135–D143.

George, Th., Virieux, J., & Madariaga, R. 1987. Seismic wave synthesis by Gaussian beam summation: A comparison with finite differences. *Geophysics*, **52**(8), 1065–1073.

Gray, S. H. 2005. Gaussian beam migration of common-shot records. *Geophysics*, **70**(4), S71–S77.

Gray, S. H., & Bleistein, N. 2009. True-amplitude Gaussian-beam migration. *Geophysics*, 1–4.

Hanyga, A. 1986. Gaussian beams in anisotropic elastic media. *Geophys. J. R. astr. Soc.*, **85**, 473–503.

Hill, N. R. 1990. Gaussian beam migration. *Geophysics*, **55**(11), 1416–1428.

Hill, N. R. 2001. Prestack Gaussian-beam depth migration. *Geophysics*, **66**(4), 1240–1250.

Isaac, J. H., & Lawton, D. C. 1999. Image simpositioning due to dipping TI media: A physical seismic modeling study. *Geophysics*, **64**, 1230–1238.

Kravstov, Y. A., & Berczynski, P. 2007. Gaussian beams in inhomogeneous media: a review. *Stud. Geophys. Geod.*, **51**, 1–36.

Martynov, V. N., & Mikhailenko, B. G. 1984. Numerical modeling of propagation of elastic waves in anisotropic inhomogeneous media for the half-space and the sphere. *Geophys. J. R. astr. Soc.*, **76**, 53–63.

Meschede, D. 2007. *Optics, Light and Lasers-The practical approach to modern aspects of Photonics and laser physics.* Wiley-VCH.

Musgrave, M. J. P. 1970. *Crystal acoustics.* Holden Day.

Nowack, S., & Orefice, A. 1993. Quasioptical treatment of electromagnetic Gaussian beams in inhomogeneous and anisotropic plasmas. *Phys. Fluid B*, **5**(7), 1945–1954.

Nowack, S., & Orefice, A. 1994. Three-dimensional propagation and absorption of high frequency Gaussian beams in magnetoactive plasmas. *Phys. Fluid B*, **1**(5), 1242–1250.

Popov, M. M. 1982. A new method of computation of wave fields using Gaussian beams. *Wave Motion*, **4**, 85–97.

Popov, M. M. 2002. *Ray theory and Gaussian beam method for geophysicists.* Salvador-Bahia.

Pšenčík, I., & Teles, T. N. 1996. Point source radiation in inhomogeneous anisotropic structures. *Pure and Applied Geophysics*, **148**, 591–623.

Siegman, A. E. 1986. *Lasers.* University science books.

Slater, C., Crampin, S., Brodov, L. Y., & Kuznetsov, V. M. 1993. Observations of anisotropic cusps in transversely isotropic clay. *Canadian Journal of Exploration Geophysics*, **29**(1), 216–226.

Sondergeld, C. H., & Rai, C. S. 1992. Laboratory observations of shear-wave propagation in anisotropic media. *Geophysics: The leading edge of exploration*, 38–43.

Thomsen, L. 1986. Weak elastic anisotropy. *Geophysics*, **51**(10), 1954–1966.

Thomsen, L., & Dellinger, J. 2003. On shear-wave triplication in transversely isotropic media. *Journal of applied geophysics*, **54**, 289–296.

Tsvankin, I. 2005. *Seismic signatures and analysis of reflection data in anisotropic media.* Elsevier.

Vavrycuk, V. 2003. Generation of triplications in transversely isotropic media. *Physical Reviews B*, **68**, 1–8.

Vavrycuk, V. 2004. Approximate conditions for the off-axis triplication in transversely isotropic media. *Stud. Geophys. Geod.*, **48**, 187–198.

Zhu, T., Gray, S. H., & Wang, D. 2007. Prestack Gaussian-beam depth migration in anisotropic media. *Geophysics*, **72**, S133–S138.

Appendix A

Dynamic ray tracing at interfaces for inhomogeneous TI media

When the ray hits the interface for reflection or transmission, we need to consider the boundary condition of dynamic ray tracing. The geometrical relations (Červený and Pšenčík, 1979) are shown in Figure (A.1). At the interface, there are three important coordinates: the local Cartesian coordinate u_i, the global Cartesian coordinates x_i, and the wavefront orthonormal coordinates y_i at the interfaces as shown in Figure (A.1). The x_2 axis, u_2 axis and y_2 axis are perpendicular to the incident plane. The symbol α indicates the angle between the positive direction of the local u_1 axis and the slowness vector of the incident wave. β is the angle between the positive direction of the local u_1 axis and the generated slowness vector. The symbol δ is the angle between the slowness vector and the positive direction of the general z axis at the point of incidence.

The 3D interface propagator matrix in the ray-centred coordinates in Červený and Moser (2007) is expressed by

$$\mathrm{II}^{(q)}(\tilde{\tau}_\Sigma, \tau_\Sigma) = \begin{pmatrix} \tilde{\mathbf{K}}^T\mathbf{K}^{-T} & \mathbf{0} \\ \tilde{\mathbf{K}}^T(\mathbf{E} - \tilde{\mathbf{E}} - (\sigma - \tilde{\sigma})\mathbf{D})\mathbf{K}^{-T} & \tilde{\mathbf{K}}^T\mathbf{K}^{-T} \end{pmatrix}. \tag{A.1}$$

Here, the expressions are valid both in plane and out of plane. All the symbols have the same meaning as in Červený and Moser (2007).

The in-plane quantities can be specified with the parameter in Figure (A.1). The new quantities for reflection or transmission are indicated as $\tilde{Q}_{ij}$ and $\tilde{P}_{ij}$ with the incident quantities Q_{ij} and P_{ij}. Specifying the formula in the above expression

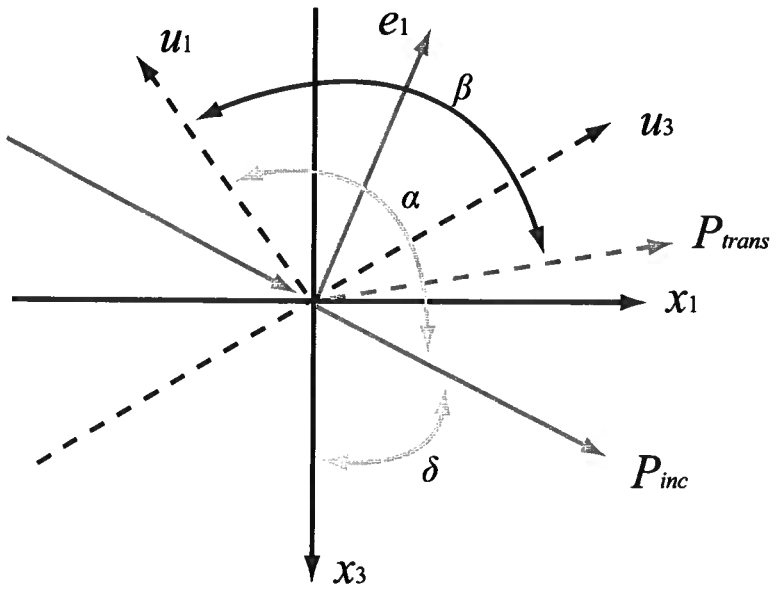

Figure A.1: Geometry for the interface coordinates. u_1 and u_3 indicate the local Cartesian coordinates. x_1 amd x_3 indicate the global Cartesian coordinates. e_2 and $\mathbf{P}$ indicate the wavefront orthonormal coordinates. u_2, x_2 and e_2 are coincident and orthogonal to the plane.

(A.1) and using the parameters in Figure (A.1), we get the explict expressions for the interface transformation in plane

$$\tilde{Q}_{\parallel}^{(y)} = Q_{\parallel}^{(y)} \sin\beta / \sin\alpha, \qquad \tilde{P}_{\parallel}^{(y)} = (P_{\parallel}^{(y)} \sin\alpha + Q_{\parallel} S_1 / \sin\alpha)/\sin\beta, \qquad \text{(A.2)}$$

with

$$\begin{aligned}
S_1 &= E_{\parallel} - \tilde{E}_{\parallel} - (\sigma - \tilde{\sigma}) D_{11}, \\
E_{\parallel} &= \frac{\cos\alpha}{V_p} \left[(\eta_x \cos\delta - \eta_z \sin\delta) \sin\alpha - \eta_x \sin(\alpha+\delta) + \eta_z \cos(\alpha+\delta) \right], \\
\tilde{E}_{\parallel} &= \frac{\cos\beta}{\tilde{V}_p} \left[(\tilde{\eta}_x \cos(\delta+\alpha-\beta) - \tilde{\eta}_z \sin(\delta+\alpha-\beta)) \sin\beta - \tilde{\eta}_x \sin(\alpha+\delta) + \tilde{\eta}_z \cos(\alpha+\delta) \right] \\
\sigma &= \frac{\cos\alpha}{V_p}, \\
\tilde{\sigma} &= \frac{\cos\beta}{\tilde{V}_p},
\end{aligned}$$

where D_{11} takes the same form as in Červený and Pšenčík (1979). All the symbols with the tilde indicate the generated wave parameters. The symbol η indicates the vector of derivative of slowness vector $\mathbf{p}$ with respect to τ:

$$\eta = \frac{\mathrm{d}\mathbf{p}}{\mathrm{d}\tau} = \{\eta_1, \eta_2, \eta_3\}\,. \tag{A.3}$$

Appendix B

Asymptotic results of 2D Gaussian beam summation

In this section, we derive the asymptotic results of the 2D GB wavefield in homogeneous media using the steepest-descent path method.

The Gaussian beam integral in homogeneous media with a unit initial amplitude can be expressed as

$$u_i = \int_D \phi(\theta) g_i \exp\{-\omega f(\theta)\} \mathrm{d}\theta, \tag{B.1}$$

where u is the displacement vector, $\phi(\theta)$ is the weighting factor, ω is the frequency, and $f(\theta)$ is the phase term which has the formula

$$f(\theta) = -it(R_r, S) + \frac{y_1^2}{2} M_{GB}. \tag{B.2}$$

As shown in Figure 3.2, R_r indicates the reference point in Figure 3.2, S is the source point, y_1 is the distance from the reference point to the receiver, and M_{GB} is the beam complex parameter.

Using the steepest-descent method, we should find the saddle point and the second-order derivative of the phase function with respect to θ.

First, let's review some basic relations of the paraxial ray theory (Červený, 2001):

$$\frac{\mathrm{d}y_1}{\mathrm{d}\theta} = Q. \tag{B.3}$$

Then, in the vicinity of the geometrical ray Ω_0, it's easy to obtain

$$y_1 = Q(\theta - \theta_0). \tag{B.4}$$

Here, Q is the dynamic ray tracing geometrical speading factor.

Also, the relations in the vicinity of the geometrical ray Ω_0 are given by

$$\begin{aligned} \frac{\mathrm{d}t(R_r,S)}{\mathrm{d}y_1} &= 0, \\ \frac{\mathrm{d}^2t(R_r,S)}{\mathrm{d}y_1^2} &= -M. \end{aligned} \tag{B.5}$$

With these basic relations, let's look into the first- or second-order derivatives of the phase term in equation (B.2). The first-order derivative of the first term is zero at the reference ray according to equation (B.5). The second term on the right has quadratic term of y_1. Therefore, the first derivative with respect to y_1 or θ is proportional to y_1. Thus, the saddle point is $y_1 = 0$ or $\theta = \theta_0$. Similarly, the second-order derivative of the phase term at the saddle point becomes two terms with the second derivative to the first term on the right side and the second-order derivative of the second term on the right. The second-order derivative of the phase term at the saddle point, only the terms without y_1 will survive. These two terms to θ read

$$\frac{\mathrm{d}^2 f}{\mathrm{d}\theta^2}|_{\theta=\theta_0} = i(M - M_{GB})(Q)^2. \tag{B.6}$$

The beam wavefield using the steepest-descent method (Bleistein, 2009) can be indicated as

$$\begin{aligned} u_i(r,\theta,\omega) &= \phi(\theta)\, g_i \sqrt{\frac{2\pi}{\omega \dfrac{\mathrm{d}^2 f}{\mathrm{d}\theta^2}|_{\theta=\theta_0}}} \exp\{i\omega t(r)\}, \\ &= \phi(\theta)\, g_i \sqrt{\frac{2\pi}{\omega\,[i(M - M_{GB})(Q)^2]}} \exp\{i\omega t(r))\}. \end{aligned} \tag{B.7}$$

The first line in this equation is based on equation (G.7) (Bleistein, 2009). Inserting equation (B.6) for the second-order derivative at the saddle point into the first line, we can obtain the final expression.

Based on Červený (2001) derivation for 3D Green's function in anisotropic media, we can obtain the Green's function and the displacement for a line source in 2D

anisotropic media:

$$u_i(R,\omega) = \sqrt{\frac{1}{2\pi\omega|Q|}}\frac{g_i}{2\rho V}\exp[i\frac{1}{2}\pi - i\frac{1}{4}\operatorname{sgn}(Q)\pi + i\omega t(S,R)]. \tag{B.8}$$

By comparing equations B.7 with B.8, we obtain the weighting factor

$$\phi(\theta) = \frac{i}{4\pi}\frac{\sqrt{(M-M_{GB})Q}}{\rho V}. \tag{B.9}$$

Appendix C

Green's function for 2D anisotropic media

Computing the Green's function is crucial for analyzing the behavior of wave propagation. The complexity of anisotropic media prevents the formulation of an analytical Green's function expression, however. To deal with this complexity, a high-frequency asymptotic method is applied. In this section, I specify the Green's function in 2D homogeneous anisotropic media following the 3D derivation in Červený (2001).

A general body force $\boldsymbol{f}$ is located at point $\boldsymbol{x}_0$. The elastodynamic wave equation reads

$$(c_{ijkl}u_{k,l})_{,j} + f_i = \rho\frac{\partial^2 u_i}{\partial t^2}, \tag{C.1}$$

where c_{ijkl} are the components of the stiffness tensor, and $u_{k,l}$ denotes the derivative of u_k with respect to x_l.

The solution can be expressed as

$$u_i(\boldsymbol{x}, t) = G_i(\boldsymbol{x}, t; \boldsymbol{x}_0, t_0). \tag{C.2}$$

Applying the 2D Fourier transform to equation C.1 yields the system of two linear equations:

$$D_{ik}\bar{u}_k = \rho^{-1}\bar{f}_i, \qquad D_{ik} = a_{ijkl}\,k_j k_l - \omega^2\delta_{ik}, \tag{C.3}$$

where a_{ijkl} are the components of the density ρ normalized stiffness tensor. The solution of this system is given by multiplying the inverse matrix $D_{ik}^{-1} = \dfrac{B_{ik}}{\det\hat{\mathbf{D}}}$ with

both sides of equation C.3

$$\bar{u}_k(k_j) = \frac{B_{ik}\bar{f}_i(k_j)}{\rho \det \hat{\mathbf{D}}}, \tag{C.4}$$

where B_{ik} are cofactors of D_{ik}. Using the inverse Fourier transform, the general solution of the elastodynamic equation is obtained

$$u_k(x_j) = \frac{1}{\rho}\int_{-\infty}^{\infty} I_k(k_1, x_3)\exp\left[ik_1x_1\right]\mathrm{d}k_1, \tag{C.5}$$

where the integral I_k is given by

$$I_k(k_1, x_3) = \int_{-\infty}^{\infty} \frac{B_{ik}\bar{f}_i(k_j)}{\det \hat{\mathbf{D}}}\exp\left[ik_3x_3\right]\mathrm{d}k_3. \tag{C.6}$$

The integral I_k can be calculated by a contour integration in a complex plane $k_3 = \mathrm{Re}(k_3) + i\mathrm{Im}(k_3)$. Contour C is composed of two parts: the first part is along the real axis and the second part is along a semicircle in the upper half-plane, $\mathrm{Im}(k_3) > 0$. The residues correspond to the roots of the equation $\det \mathbf{D} = 0$. Equation $\det \mathbf{D} = 0$ has four roots for k_3. If the imaginary of k_3 is negative, the energy of the wave increases with wave propagation. Here the out-going waves are only considered, which correspond to $k_3 > 0$ from the real k_3- axis into region C^+ (upper half-plane).

One of the roots of $\det \hat{\mathbf{D}}$ for k_3 in region C^+ can be denoted as $k_3 = \theta(k_1)$. Because inhomogeneous waves are not considered, function $\theta(k_1)$ is real-valued and positive. Calculating the residue of integral I_k for root $k_3 = \theta(k_1)$ yields

$$I_k = 2\pi i \left\{ \frac{B_{ik}\,\bar{f}(k_j)}{\partial \det \hat{\mathbf{D}}/\partial k_3}\exp\left[ik_3x_3\right] \right\}_{k_3=\theta(k_1)}. \tag{C.7}$$

Inserting equation C.7 to equation C.5 leads to

$$u_k(R) = \frac{2\pi i}{\rho}\int_{-\infty}^{\infty} \left\{ \frac{B_{ik}\,\bar{f}(k_j)}{\partial \det \hat{\mathbf{D}}/\partial k_3}\exp\left[ik_3x_3\right] \right\}_{k_3=\theta(k_1)} d\,k_1. \tag{C.8}$$

Substituting $k_i = \omega\, p_i$, I obtain $\det \hat{\mathbf{D}} = \omega^4 \det(\Gamma_{in} - \delta_{in})$, where Γ_{in} are components of the Christoffel matrix $\Gamma_{in} = a_{ijnl}p_jp_l$. Similarly, $B_{ik} = \omega^2 S_{ik}$, where S_{ik} are

cofactors of $\Gamma_{ik} - \delta_{ik}$. Hence,

$$u_k(R) = \frac{2\pi i}{\rho} \int_{-\infty}^{\infty} A_{ik}(p_1) \bar{f}(p_1) \exp\left[i\omega\theta(p_1)x_3\right] \mathrm{d}p_1, \tag{C.9}$$

$$A_{ik}(p_1) = \left\{ \frac{S_{ik}}{\partial \det(\Gamma_{in} - \delta_{in})/\partial p_3} \right\}_{p_3=\theta(p_1)}, \tag{C.10}$$

$$\bar{f}(p_1) = \left\{ \bar{f}(\omega p_1) \right\}_{p_3=\theta(p_1)}. \tag{C.11}$$

where, quantity $p_3 = \theta(p_1)$ is a positive real-valued root of the equation $\det(\Gamma_{in} - \delta_{in}) = 0$. The equation $\det(\Gamma_{in} - \delta_{in}) = 0$ represents the slowness surface, including the slowness surface branches corresponding to P- and SV-waves. Thus, the integral is calculated over the slowness surface $p_3 = \theta(p_1)$.

Expression for $A_{ik}(p_1)$ can be calculated in an alternative method. Substituting $k_i = \omega p_i$ into equation C.3, equation $\bar{u}_k$ is observed in the following form: $(\Gamma_{ik} - \delta_{ik})\, \bar{u}_k = \omega^{-2}\rho^{-1}\bar{f}$. I seek solution $\bar{u}_k$ using the relation $\bar{u}_k = \omega^{-2} A\, g_k$, where $\boldsymbol{g}$ is the eigenvector of Γ_{ik}, corresponding to eigenvalue G. Multiplying this equation by $g_i g_k$ yields

$$A\left(\Gamma_{ik} g_i\, g_k - 1\right) = A\left(G - 1\right) = \rho^{-1}\bar{f}. \tag{C.12}$$

Consequently, one of the solutions of equation $(\Gamma_{ik} - \delta_{ik})\, \bar{u}_k = \omega^{-2}\rho^{-1}\bar{f}_i$ is $\bar{u}_k = \omega^{-2}\rho^{-1} g_k\, \bar{f}_i / \left(G - 1\right)$. Using this new form of the solution in integrals leads to

$$A_k(p_1) = g_k / (\partial G / \partial p_3). \tag{C.13}$$

Based on the ray theory, the above equation is simplified by $\partial G/\partial p_3 = V_G$ which is the group velocity.

If I specify the line source function $f_i(x_j) = \delta(\boldsymbol{x} - \boldsymbol{x}(S))\ \delta(t - t_0)$ in the time domain, the source function in the frequency domain reads

$$\bar{f}_i(p_1) = (4\pi^2)^{-1} \exp\left[-i\omega r\theta(p_1)\right]. \tag{C.14}$$

Inserting C.14 into the expression for the Green's function, I obtain

$$G_k(R,S,\omega) = \frac{i}{2\pi\rho}\int_{-\infty}^{\infty} A_k(p_1)\exp\left[i\omega r\theta(p_1)\right]\mathrm{d}p_1. \tag{C.15}$$

Following the procedure of the stationary phase method in Červený (2001) book, I obtain the asymptotic expression

$$G_k(R,S,\omega) = \frac{i}{2\pi\rho}A_k\exp[i\omega p_3^{(y)}r]\int_{-\infty}^{\infty}\exp[\frac{1}{2}i\omega k_1^{(y)}(p_1^{(y)}-p_1^{(y)})^2 r]\mathrm{d}p_1^{(y)}. \tag{C.16}$$

where the upper script (y) indicates the wavefront orthogonal coordinate system.

Using the Poisson integral

$$\int_{-\infty}^{\infty}\exp[iku^2]\mathrm{d}u = \sqrt{\frac{\pi}{\mid k\mid}}\exp\left[\frac{1}{4}i\pi\ \mathrm{sgn}(k)\right] \tag{C.17}$$

yields

$$\int_{-\infty}^{\infty}\exp\left[i\left[\frac{1}{2}\omega k_1^{(y)}r\right](p_1^{(y)}-p_1^{(y)})^2\right]\mathrm{d}p_1^{(y)} \sim \sqrt{\frac{2\pi}{\left[\omega\mid k_1^{(y)}\mid r\right]}}\exp\left[\frac{1}{4}i\pi\ \mathrm{sgn}\left[k_1^{(y)}\right]\right] \tag{C.18}$$

Here, $k_1^{(y)}$ shows the Gaussian curvature in the wavefield which can be obtained by $k_1^{(y)} = -\dfrac{\partial^2\theta(p_1^{(y)})}{\partial(p_1^{(y)})^2}$. Using the relations in Červený's book (sec. 4.14, 2001) yields $k_1 = \dfrac{Q_2V_p^2}{rU^2}$. The final expression of the wavefield can be indicated as

$$u_k(r,\theta,\omega) \sim \sqrt{\frac{1}{2\pi\omega|Q_2|}}\frac{g_k}{2\rho V_p}\exp\left[i\frac{1}{2}\pi - i\frac{1}{4}\mathrm{sgn}\,(Q_2)\pi + i\omega\tau(R,S)\right]. \tag{C.19}$$